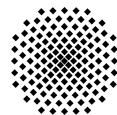# Microwave Investigation of Low-Dimensional Organic Conductors

Von der Fakultät Mathematik und Physik
der Universität Stuttgart
zur Erlangung der Würde eines Doktors der
Naturwissenschaften (Dr. rer. nat.) genehmigte Abhandlung

Vorgelegt von
Konstantin Petukhov
geboren in Kriwoj Rog

Hauptberichter: Prof. Dr. M. Dressel
Mitberichter: Prof. Dr. M. Mehring
Tag der mündlichen Prüfung: 23. Juni 2003

1. Physikalisches Institut

Universität Stuttgart
2003

Table of Contents

4

6

List of Abbreviations

1[2,3]D	one- [two-, three-] dimensional
AC	alternating current
AO	anion ordering
APRES	angle-resolved photoemission (experiment)
BCS	Bardeen, Cooper, and Schriffer (theory)
CDW	charge density wave
DAC	digital-to-analog (converter)
DC	direct current
EM	electro-magnetic (radiation)
ESR	electron spin resonance
FIR	far-infrared (spectral range)
FL	Fermi liquid
FLR	Fukuyama, Lee, and Rice (model)
IEEE	(interface by) Institute of Electrical and Electronics Engineers
HOMO	highest occupied molecular orbital
KK	Kramers-Kronig (transformations)
LHe	liquid helium
LL	Luttinger liquid
LN_2	liquid nitrogen
NMR	nuclear magnetic resonance
MW	microwave (radiation)
PID	proportional-integral-derivative (coefficient)

Q1[2,3]D	quasi-one- [two-, three-] dimensional
Q-factor	quality factor (of a resonator)
RF	radio frequency (spectral range)
SC	superconductivity/tor/ing
SDW	spin density wave
SP	spin-Peierls (ground state)
SS	singlet superconductivity/tor
TE$_{mnp}$	transversal electric (mode)
TM$_{mnp}$	transversal magnetic (mode)
(TM)$_2$X	Bechgaard salts
TMTSF	Tetramethyletetraselenafulvalene
TMTTF	Tetramethyletetrathiafulvalene
TS	triplet superconductivity/tor

Abstract

We present measurements of electrodynamical response of $(TMTSF)_2PF_6$, a representative member of the organic quasi-one dimensional Bechgaard salts, in both the normal ($T > 12$ K) and spin density wave state ($T < 12$ K). We report on the investigations performed along the chain axis a, and transverse crystallographic axes b' and c^*. For the measurements along the b' axis the single crystals samples were utilized for the first time. These measurements have been made at 24 and 33.5 GHz frequency and were anticipated by the DC transport measurements.

For the measurements at microwave frequencies the contactless cavity perturbation technique, employing the cylindrical copper cavity operated in the TE_{011} transmission mode, was developed. The design of the cavities allowed us to rotate the sample inside it, resulting in a precise sample alignment. The measurements were collected in the temperature range from 300 K down to 2 K.

The normal state transport properties of $(TMTSF)_2PF_6$ were analyzed in the framework of Luttinger liquid and Fermi liquid. The strong discrepancies forward the description within the Luttinger liquid picture were evidenced. The formation of the SDW ground state in all three directions was observed below 12 K. The thermal activation energy value at zero frequency ($\Delta_0 = 21$ K) is in a good agreement with literature single particle gap value, while at the microwave frequencies the valuable reduction of the activation behavior (with $\Delta = 6$ K) was observed along the a and b' crystallographic axes. Such behavior is indicative of a strongly frequency-dependent response and was attributed to the vicinity of the SDW pinned mode in the microwave frequency range. The low-temperature anomalies, below $T < 3.5$ K, were

evidenced deeply in the SDW state at 33.5 GHz, and we believe that these anomalies are due to the exceeding of the threshold electric field when performing the microwave measurements.

Kurzfassung

Stark anisotrope organische Kristalle dienen als Modellsysteme für quasi-eindimensionale Metalle. Die Frage, ob die Transporteigenschaften der Bechgaardsalze $(TMTSF)_2X$ im Rahmen der Fermiflüssigkeits-Theorie ("Fermi liquid", FL) oder der Luttingerflüssigkeits-Theorie ("Luttinger liquid", LL) verstanden werden können, ist Gegenstand einer lang andauernden Diskussion. Die Art der metallischen Phase eines wechselwirkenden Elektronensystems hängt stark von der Dimensionalität ab. Es ist aus theoretischen Überlegungen wohlbekannt, dass die konventionelle FL-Theorie dreidimensionaler (3D) Metalle nicht auf wechselwirkende Elektronen, deren Bewegung auf eine Dimension beschränkt ist, angewandt werden kann. Dies führt zur Formation des LL Zustandes.

Unter allen experimentellen Ansätzen, mit denen die Dimensionalität des Elektronengases in Bechgaardsalzen studiert werden kann, sind Messungen des transversalen Transports besonders wichtig, um direkt die Zwischenkettenkopplungen zu untersuchen. Aus diesem Grunde besteht ein hohes Interesse an zuverlässigen Messungen der Transporteigenschaften entlang der b'- und c^*-Richtungen. Dies war die Motivation für die vorgelegte Arbeit.

Die Untersuchung des Spindichtewellen (SDW) Grundzustandes bei tiefen Temperaturen in $(TMTSF)_2PF_6$ im Mikrowellenbereich ist ebenfalls von großem Interesse. Es wurde angenommen, dass die Modulation der Spindichte nicht vollständig kommensurabel mit dem unterliegenden Kristallgitter ist und dass die kollektive Mode gleitet und damit einen elektrischen Strom transportieren kann. Haftung ("Pinning") an Verunreinigungen lässt die kollektive Mode bei endlichen Frequenzen schwingen.

Die Resonanz durch die gepinnte Mode liegt in einener Reiche von Modellsystemen im Spektralbereich von Millimeterwellen [61]. Durch Anlegen eines äußeren elektrischen Feldes kann die kollektive Mode von den Haftzentren gelöst ("Depinning") werden und einen Strom transportieren. Die Elektrodynamik des SDW-Zustandes wurde bei unterschiedlichen Mikrowellenfrequenzen (3–100 GHz) entlang der Kettenrichtung (a-Achse) ausführlich untersucht [131, 132]. Bis jetzt gibt es keine Berichte über Mikrowellentransportmessungen an $(TMTSF)_2PF_6$ im SDW-Zustand entlang der beiden senkrechten Richtungen (b' und c^*).

$(TMTSF)_2PF_6$ -Einkristalle von hoher Qualität wurden mit Hilfe der elektrochemischen Oxidation hergestellt. Die Proben sind nadelförmig mit den typischen Dimensionen 2 mm × 0.5 mm × 0.1 mm entlang der a-, b'- und c^*-Achsen. Die Messungen der b'-Achsen Leitfähigkeit wurden an schmalen Kristallstücken, welche aus einem dicken Kristall parallel zur Kettenrichtung (lange Achse der Nadeln) herausgeschnitten wurden, durchgeführt; typische Dimensionen dieser Kristallstücke: 0.2 mm × 1.3 mm × 0.3 mm ($a \times b' \times c^*$). Die Mikrowellenmessungen in c^*-Richtung wurden an Mosaiken durchgeführt.

In dieser Arbeit werden Messungen der elektrodynamischen Antwort von $(TMTSF)_2PF_6$, einem repräsentativen Mitglied der Familie der organischen quasi eindimensionalen Bechgaardsalze, sowohl im normalen Zustand ($T > 12$ K) als auch im Spindichtewellen-Zustand ($T < 12$ K) präsentiert. Es wird über Untersuchungen entlang der Kettenachse a und der senkrechten Richtungen b' und c^* berichtet. Diese Messungen fanden bei Frequenzen von 24 und 33.5 GHz statt und wurden von ergänzenden Gleichstrommessungen begleitet.

Die Gleichstromwiderstandsmessungen wurden mit einer Standard-Vierpunktmesstechnik durchgeführt, um Einflüsse von Kontaktwiderständen zu eliminieren. Die Proben wurden langsam abgekühlt. Dadurch wurden Brüche in den Kristallen verhindert und ein gutes thermisches Gleichgewicht mit den Temperatursensoren gewährleistet. Die Widerstandsdaten wurden in einem weiten Temperaturbereich von 300 K bis 2 K aufgenommen.

Der niedrige Wert des Restwiderstandes ρ_a ist zusammen mit dem großen Widerstandverhältnis $\rho_a(300\ \text{K})/\rho_a(20\ \text{K})$ ein Anzeichen für eine sehr hohe Qualität der Einkristalle. Unterhalb von 70 K folgt der spezifische Widerstand einer quadratischen Temperaturabhängigkeit $\rho_a(T), \rho_{b'}(T) \propto T^2$ entlang der a- und b'-Richtung. Dieses Verhalten ist ein starkes Indiz für inelastische Elektron-Elektron Wechselwirkung und ist typisch für Fermiflüssigkeiten. Die quadratische Temperaturabhängigkeit in dem Temperaturbereich 12 K $< T <$ 70 K wurde nicht entlang der c^*-Richtung beobachtet. Hier gilt eher $\rho_{c^*}(T) \propto T$. Die Proportionalität $\rho_a(T) \propto \rho_{b'}(T)$ weist auf eine einfache anisotrope Bandstruktur mit isotroper Relaxationszeit $\tau(T)$ hin. Die Anisotropie $\rho_{b'}/\rho_a \simeq 180$ ist deshalb temperaturunabhängig. Zusammen mit der kleinen Bandbreite weist die temperaturunabhängige Anisotropie auch darauf hin, dass die "Tight-Binding"-Näherung angemessen ist. Daraus folgt eine einfache anisotrope Bänderstruktur: $(4t_a : 4t_b : 4t_c) \approx (1 : 4 \times 10^{-2} : 4 \times 10^{-3})$ eV = (11600 : 460 : 46) K. Dieses Resultat stimmt gut mit der Anisotropie, welche in Bandstrukturrechnungen bestimmt wurde, überein [24].

Im normalen Zustand oberhalb von $T = 100$ K, in dem das System mehr eindimensional sein sollte, wurden die Gleichstromeigenschaften im Rahmen der Luttingerflüssigkeits-Theorie analysiert. Diese liefert die folgenden Abhängigkeiten für den longitudinalen ($\rho_\parallel$) bzw. transversalen ($\rho_\perp$) spezifischen Widerstand:

$$\rho_\parallel(T) \sim T^{16K_\rho - 3},$$

$$\rho_\perp(T) \sim T^{1-2\alpha},$$

wobei K_ρ derjenige Exponent ist, der die Freiheitsgrade der Ladungen eines LL charakterisiert, und $\alpha = 1/4(K_\rho + 1/K_\rho) - 1/2$.

Die Bechgaardsalze sind bekannt dafür, dass ein großer Teil der Temperaturabhängigkeit der Leitfähigkeit durch thermische Ausdehnung verursacht wird. Um die Gleichstromleitfähigkeit von $(\text{TMTSF})_2\text{PF}_6$ innerhalb des LL Formalismus, welcher das Verhalten von Messgrößen in strikt eindimensionalen Systemen bei konstantem Volumen beschreibt, analysieren zu können, mussten die bei konstantem Druck

gemessenen Daten in die Leitfähigkeit bei konstantem Volumen konvertiert werden. Die Druckkoeffizienten für die Leitfähigkeit von $(TMTSF)_2PF_6$ sind aus der Literatur bekannt [30, 88].

Die Temperaturabhängigkeit der Gleichstromleitfähigkeit bei hohen Temperaturen 100 K $< T <$ 300 K ist durch $\rho_\parallel = \rho_a \propto T^{0.56}$ gegeben. Ein Vergleich mit den Vorhersagen der LL Theorie liefert den Exponenten $K_\rho = 0.22$. Optische Experimente entlang der Ketten [105, 58] lieferten $K_\rho = 0.23$. Wenn allerdings der Wert $K_\rho = 0.22$ verwendet wird, um die spezifischen Widerstandsdaten, die entlang der beiden senkrechten Achsen b' und c^* im selben Temperaturbereich gemessen wurden, zu beschreiben, gibt es eine Inkonsistenz: aus $K_\rho = 0.22$ folgt für den transversalen spezifischen Widerstand $\rho_\parallel \propto T^{-0.36}$, die experimentellen Ergebnisse dieser Arbeit zeigen aber eindeutig, dass $\rho_{b'} \propto T^{0.24}$ und $\rho_{c^*} \propto T^{-0.95}$. Die hier diskutierten Resultate zeigen somit deutliche Widersprüche zu den Vorhersagen der Luttingerflüssigkeitstheorie auf.

Bei tiefen Temperaturen wurde der SDW Grundzustand unterhalb von $T = 12$ K entlang aller drei Kristallrichtungen gefunden. Aktiviertes Verhalten wurde eindeutig durch die $\log \rho(1/T)$-Auftragung nachgewiesen. Die thermische Aktivierungsenergie wurde entlang aller drei Achsen zu $\Delta \simeq 21$ K bestimmt. Dieser Wert kann perfekt mit "Mean-Field" BCS-Theorie beschrieben werden, welche für die Übergangstemperatur $T_C = 12$ K die Energielücke $\Delta = 1.76 k_B T_C = 21$ K liefert.

Da die Bechgaardsalze eine ausgeprägte Nadelform haben ($a \gg b'$), ist es insbesondere schwer, Transportmessungen entlang der senkrechten Richtung b' mit Standard-Gleichstrommethoden durchzuführen. Bedingt durch eine nicht gleichförmige Ladungsverteilung zwischen den Kontakten können parasitäre Beiträge aus anderen Kristallrichtungen eine Rolle spielen. Man kann diese Probleme umgehen, indem man eine kontaktfreie Mikrowellenmesstechnik verwendet, die eine bessere Kontrolle der Orientierung der Stromlinien in den organischen Nadeln erlaubt.

Die Messungen der Mikrowellenleitfähigkeit wurden mit Hilfe der kontaktfreien

Hohlkörperstörmethode ("Cavity Pertubation Technique") durchgeführt unter Verwendung zylindrischer Kupferresonatoren, welche in der TE_{011} Transmissionsmode bei den Resonanzfrequenzen 24 oder 33.5 GHz arbeiten. Die Probe wurde mit einem Quarzstab im Maximum des elektrischen Feldes positioniert. Es wurden nadelförmige Proben für die Messungen entlang der a- und b'-Richtungen und Mosaike für die Untersuchungen entlang der kristallografischen c^*-Richtung verwendet. Während der Messungen kann die Probe innerhalb des Resonators rotiert werden, was Messungen der Anisotropie *insitu* erlaubt. Im Experiment wird die Änderung der Resonanzfrequenz $\left(\frac{\Delta\omega}{\omega_0}\right)$ und der Güte $\left(\Delta\frac{1}{2Q}\right)$ des Resonators nach Einführung der Probe gemessen. Ein kompletter Durchgang einer temperaturabhängigen Messung von 300 K bis 2 K ist mit verschiedenen Kühlraten möglich. Bei jeder gewünschten Temperatur wurden sowohl die Resonanzfrequenz $f_0 = \frac{\omega_0}{2\pi}$ als auch die Halbwertsbreite $\Gamma = \frac{f_0}{Q}$ gemessen. Mit der Apparatur können bei Zimmertemperatur Veränderungen der Frequenz oder Halbwertsbreite mit einer Auflösung, die besser als 5×10^{-7} ist, gemessen werden. Durch Abkühlen zu tiefen Temperaturen verbessert sich die Auflösung weiter um einen Faktor 2, die Temperaturgenauigkeit beträgt 10 mK.

Die komplexe Leitfähigkeit σ der Probe wird aus den Änderungen der Resonatorparameter Γ und Δf_0 bestimmt. Die Resultate wurden entweder im Rahmen der quasistatischen Näherung oder des Oberflächenimpedanz-Formalismus analysiert. Erstere ist anzuwenden, wenn die Skin-Eindringtiefe die Dimensionen der Probe überschreitet und die Mikrowellenstrahlung die Probe völlig durchdringt (Depolarisationsbereich), letzterer, im entgegengesetzten Fall (Skintiefen-Bereich).

Mit der selbstkonsistenten Analyse war es möglich die absoluten Werte des spezifischen Mikrowellenwiderstands von von $(\text{TMTSF})_2\text{PF}_6$ entlang aller drei Richtungen zu bestimmen. Die Temperaturabhängigkeit der spezifischen Mikrowellenwiderstände $\rho_a, \rho_{b'}$ und ρ_{c^*} ist ähnlich bei beiden Mikrowellenfrequenzen 24 und 33.5 GHz, ρ_a und $\rho_{b'}$ unterscheiden sich aber von den Gleichstromwerten. Nur der spezifische Mikrowellenwiderstand entlang der c^*-Achse skaliert mit den zugehörigen Gleichstromdaten,

während die spezifischen Mikrowellenwiderstände ρ_a und $\rho_{b'}$ eine schwächere Temperaturabhängigkeit zeigen, sowohl im normalen Zustand als auch im SDW Zustand. Darüberhinaus wurde gefunden, dass der spezifische Mikrowellenwiderstand $\rho_{b'}$ im Temperaturbereich 25 K $< T <$ 55 K im normalen Zustand nicht metallisch ist: mit abnehmender Temperatur nimmt $\rho_{b'}$ zunächst monoton ab bis zu einem lokalen Minimum bei 55 K, steigt dann leicht an bis zu einem lokalen Maximum nahe 25 K und nimmt dann wieder ab bis zum SDW Übergang bei 12 K. Die negative Steigung $\rho_{b'}/\mathrm{d}T < 0$ im Temperaturbereich 25 K $< T <$ 55 K widerlegt die mögliche Existenz von Quasiteilchenzuständen entsprechend dem Fermiflüssigkeitsmodell. Um die Mikrowellendaten im Rahmen der Luttingerflüssigkeits Theorie zu beschreiben, wurde eine Konvertierung der gemessenen Daten in den spezifischen Widerstand bei konstantem Volumen vorgenommen gemäß dem oben beschriebenen Verfahren.

Die Analyse der experimentellen Daten liefert $\rho_\perp(T) = \rho_{b'}(T) \propto T^{-0.4}$ im Temperaturbereich 20 K $< T <$ 45 K, daraus folgt $K_\rho = 0.22$ im LL Modell. Wird dieser Wert $K_\rho = 0.22$ verwendet, um den Verlauf der spezifischen Widerstandsdaten, welche entlang der Kettenrichtung a im selben Temperaturbereich 20 K $< T <$ 55 K aufgenommen wurden, zu beschreiben, taucht eine Inkonsistenz auf: mit $K_\rho = 0.22$ würde man eine Temperaturabhängigkeit des longitudinalen spezifischen Widerstandes gemäß $\rho_\parallel(T) = \rho_a(T) \propto T^{0.5}$ erwarten, während die experimentellen Resultate eindeutig einen temperaturunabhängigen Widerstand in diesem Temperaturbereich zeigen. Daraus folgt, dass man die Mikrowellendaten von $(\mathrm{TMTSF})_2\mathrm{PF}_6$ nicht vollständig innerhalb des LL Bildes verstehen kann.

Der Spindichtewellen-Übergang in $(\mathrm{TMTSF})_2\mathrm{PF}_6$ wurde in allen drei Kristallrichtungen bei 12 K nachgewiesen. Mit Hilfe des Arrhenius Auftrages $\log \rho(1/T)$ des spezifischen Mikrowellenzustandes im Bereich des thermisch aktivierten Verhaltens wurde ein mittlerer Wert der Aktivierungsenergie im SDW Zustand entlang der c^*-Achse von $\Delta_{c^*} \simeq 20.7$ K gefunden. Dieser bei Mikrowellenfrequenzen gemessene Wert für die Energielücke stimmt sehr gut mit der aus den Gleichstrommessungen abgeleiteten Einteilchenenergielücke $\Delta_0 = 21$ K überein. Entlang der a- und b'-Richtungen

wurden deutlich niedrigere Werte für die Aktivierungsenergien im Mikrowellenbereich gefunden: $\Delta_a \approx \Delta_{b'} \approx 6$ K. Dieses Verhalten ist ein Anzeichen für eine stark frequenzabhängige elektrodynamische Antwort und kann durch die Nähe der SDW Mode ("Pinned Mode") im Mikrowellenfrequenzbereich erklärt werden. Es wurde vorgeschlagen, dass das SDW Kondensat in $(TMTSF)_2PF_6$ bei Mikrowellenfrequenzen an den Verunreinigungen haftet. Aus den hier vorgestellten Ergebnissen kann man schlussfolgern, dass die Mikrowellenuntersuchungen in einem Bereich stattfanden, in dem die kollektive Mode immer noch die Messungen beeinflusst, d.h. an der Schulter der Resonanz der Haftmode. Werden Messungen bei 24 und 33.5 GHz durchgeführt, so gibt es nicht vernachlässigbare Beiträge der kollektiven Mode ("Pinned SDW Mode") zu den Transporteigenschaften des Systems, was wiederum zu einer Reduzierung des thermisch aktivierten Verhaltens des spezifischen Widerstandes im SDW Grundzustand führt. Zieht man einen zweidimensionalen Nesting-Vektor in der a-b' Ebene in Betracht, so führt dies zu einer vergleichbaren Antwort der SDW entlang der a- und entlang der b'-Achse. Das aktivierte Verhalten wird dann durch die Resonanzmode in beiden Richtungen gleichermaßen reduziert, während die Antwort entlang der c^*-Achse unverändert bleibt. Betrachtet man im SDW Zustand den Gleichstromfall ($\omega = 0$), so besitzt der Transport nur Einteilcheneigenschaften.

Anomalien wurden bei Temperaturen unterhalb von T = 3.5 K im SDW Zustand bei der Frequenz 33.5 GHz beobachtet. Vermutlich sind diese Anomalien darauf zurückzuführen, dass während der Durchführung der Mikrowellenmessungen das elektrische Grenzfeld überschritten wurde.

Chapter 1

Organic Conductors

"...organic conductors are a laboratory of solid state physics."

— P. M. Grant

In 1842 the German chemist W. Knop synthesized $K_2Pt(CN)_4$ which had an unusual aspect; unlike most metal salts that have a mineral-like colored or white appearance, it had a golden brown metallic sheen. In 1910 the British scientist Burt prepared another odd material which had the look of a metal, this time it was a polymer of linked sulfur and nitrogen atoms. These two were the first "metals from molecules". But it was not until the 1970's that the electrical properties of these materials were investigated [1]. In this time, a great variety of both organic (e.g., TTF-TCNQ) and inorganic (e.g., $NbSe_3$ or $K_{0.3}MoO_3$) linear chain compounds with an anisotropic overlap of the electronic orbitals have been synthesized. It turned out that the electronic properties of organic conductors are extraordinarily sensitive to even marginal changes in molecular structure. Due to this reason, organic conductors exhibit an especially rich variety of behaviors and their properties can easily be turned over a wide range. In this chapter a brief overview of fundamental organic conductors and their basic properties will be given.

In Section 1.1 we will give the basics of the classification and historical overview of the investigations of organic conductors and superconductors. We will also answer the

question why conductivity in organic solids is possible. The model material for our experiments, the quasi-1-dimensional Bechgaard salts $(TMTSF)_2X$, are introduced in Section 1.2, where we will consider their crystal structure and electronic band structure. A very rich phase diagram of the Bechgaard salts family will lead our narration to the next Chapter 2 "Low dimensional physics".

1.1   Organic Conductors: an Overview

Organic conductors are compounds containing along with carbon also elements such as hydrogen (H), nitrogen (N), sulfur (S), selenium (Se), oxygen (O), phosphorus (P), and having considerable values of conductivity $\sigma \geq 1\ \Omega^{-1}{\cdot}cm^{-1}$, which shows metallic temperature dependence $\sigma(T)$. Sometimes they are referred to as *synthetic metals*, emphasizing by this that the electronic properties typical for metals are obtained in them by synthesis of special organic chemical substances. What defines the electronic transport properties of organic compounds and forces them to be either conductors or dielectrics? A close look to their structure may answer this question.

In general, it is not so easy to get an organic material which is not insulating because they like to have closed shells with localized electrons. The main problem is how to create delocalized electrons. This is done by doping of polymers or by charge transfer between cations and anions. These additional electrons now can move on the chains of the polymer or of the molecules (anion or cation chains).

Structurally all existing organic conductors can be divided into two groups: *polymers* and *charge transfer salts*. Conductors of the first group are various polymers based on hydrocarbons. They have conjugated bonds all along their length, the length of such a conjugation chain reaches several thousands angstroms, and polymer molecules are assembled in fibers of diameter of 200 Å. The interactions between threads in a fiber are very weak, and electrons motion is completely of one-dimensional nature. Let us consider the simplest representative of the polymer family, namely the

polyacetylene ($-CH=CH-)_n$. Ideally, the delocalization of p-electrons along the polymer molecule due to an overlap of corresponding π-orbitals brings polyacetylene to a metallic state , and one would call such a hypothetical conducting polymer *polyene* (Fig. 1.1, a). However, the metallic state with equidistant spacing between carbon atoms in polyene is unstable against a so-called Peierls transition – dimerization [2]; this phenomenon will be discussed in details in Sec. 2.1. Due to the dimerization and Coulomb repulsion, a gap of 1.5 eV opens in the energy spectrum of the p-electrons in pure polyacetylene, forcing it to be a dielectric (Fig. 1.1, b). In 1977 it was first discovered that the conductivity of polyacetylene can be increased by "doping" by many orders of magnitude [3]. Doping of polyacetylene with atoms of potassium (K), sodium (Na), bromine (Br), iodine (I), or complexes like AsF_6, or other organic donors or acceptors leads to the emergence of spinless charge carriers – solitons, specific for Peierls dielectrics. Solitons determine the conductivity of the family $(CHX_m)_n$; at $m < 0.1$ the conductivity reaches the values of 10^{-4} – 10^{-3} $\Omega^{-1}\cdot cm^{-1}$ at temperature $T = 300\ K$ and decreases on cooling. At $m > 0.1$ a typical for metals paramagnetic susceptibility appears [4].

The representatives of the second group of organic conductors – *charge transfer salts* – contain organic molecules with conjugated bonds. These molecules play the role of donors and acceptors. In crystals of charge transfer salts plane molecules are packed in such a way, that the ions of one sign pile up like pancakes to form stacks, alternated with piles or chains of ions of the opposite sign (Fig. 1.2). The planarity of these molecules is an essential condition to build a charge transfer salt – the molecules can be packed closer to each other providing an overlap of the respective molecular orbitals. The p-electron orbitals of conjugated bonds of planar molecules have the slope of the figure-of-eight, elongated perpendicular to the plane of the molecule (Fig. 1.2, the right stack). They provide a rather good overlap of the electron wave-functions of neighboring molecules in a chain. Therefore electrons of the plane molecules are delocalized not only inside a molecule, but also along a pile. In the neutral state donor and acceptor molecules contain an even number of p-electrons,
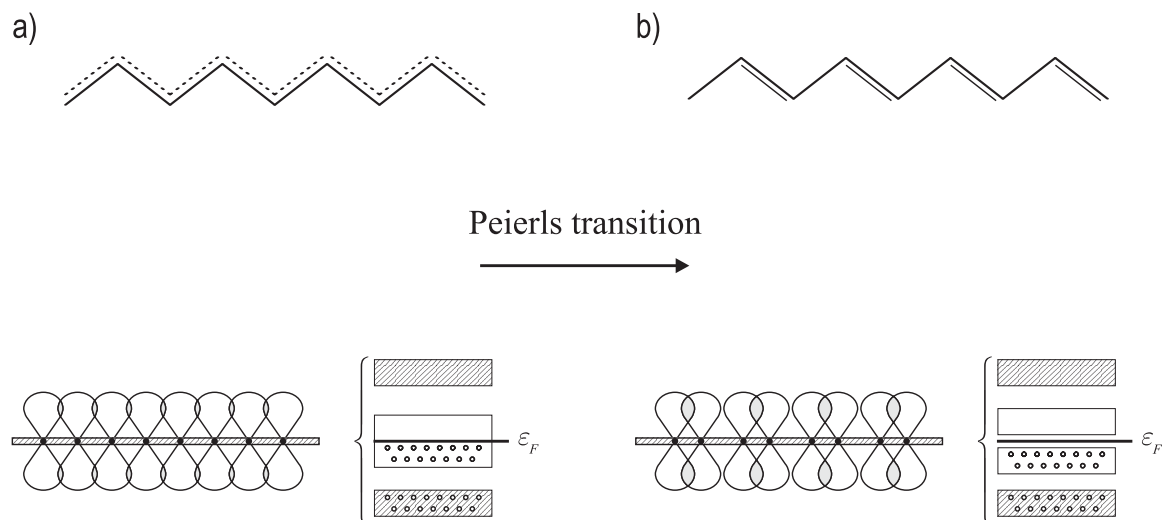
Figure 1.1: (a) *Polyene* – the simplest hypothetical conducting polymer, where electrons are delocalized all over the solid (dashed line). Due to the Peierls transition, polyene transforms to polyacetylene, a natural dielectric polymer with conjugated double bonds (b).

but when the crystal is formed, the number of electrons in the p-shell changes and p-electron band turns out to be partially filled in a pile. Thus, the two conditions necessary for metallic behavior of electrons are realized: partial filling of p-electron band, and their delocalization, at least along a chain.

Historically, the search of organic conductors was greatly stimulated by the idea of W. A. Little [5] that the coupling of the electrons to Cooper pairs might possibly be caused by an exitonic mechanism which could yield superconducting transition temperatures T_c easily above the room temperature. The field of practical investigations of organic conductors started in 1960 and 1970 with the discoveries of the molecules TCNQ (tetracyanoquinodimethane) and TTF (tetrathiofulvalene), respectively [6, 7]. Three years later Ferraris was the first to combine both anion (TCNQ) and cation (TTF) molecules in the ratio 1:1 and in this way to form the TTF-TCNQ molecule [8] of the first conducting charge transfer salt. The planar molecules of TTF-TCNQ form segregated stacks in a plane-to-plane manner and the molecular π-orbitals can interact preferably along the stacking direction (crystallographic b-direction of the
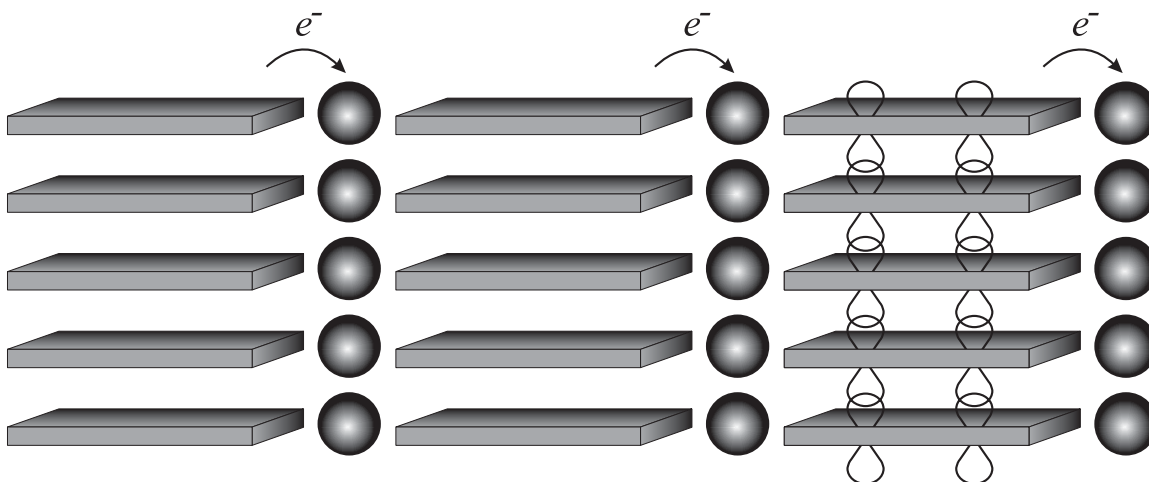
Figure 1.2: Schematic representation of a charge transfer salt. Planar molecules of donors (cations) are packed in stacks alternating with chains of acceptor molecules (anions, shown as balls). The intermolecular overlap of π-orbitals between the donor molecules is shown in the right stack, as an example.

monoclinic structure), leaving only weak interactions in the perpendicular a- and c-crystallographic directions. Hence TTF-TCNQ complexes exhibit very anisotropic conduction properties; they behave as quasi-1D conductors, although they are, of cause, three-dimensional crystals. Their one-dimensional nature also determines their shape: naturally they grow in needle-like form, which is by itself a clear indication of existing of a "preferential direction", whatever it means. The promising discovery of rather large room temperature conductivity of *ca.* $\sigma_b \sim 1000$ $\Omega^{-1}\cdot$cm^{-1} (less than three orders of magnitude smaller compared to copper), which increased by more than an order of magnitude upon cooling to 60 K, and its anisotropy (σ_b/σ_c) of *ca.* 500 led to intense search for other conducting organic molecules. Such a search was particularly promising, since TTF-TCNQ was subjected to metal-insulator transition at 54 K due to a Peierls instability of the 1D electron system [9, 10] and the task was to suppress this transition. (Sec. 2.1.1).

Under some physical conditions charge transfer salts may even become super-conductors. The practical possibility of reaching of superconductivity in compounds without a single metallic atom, but with two-dimensional (layered) nature of electron

motion was established by R. L. Greene and coworkers in 1975, as a result of experiments performed on synthesized polymeric polysulfurnitride $(SN)_x$ [11]. Molecules in crystals of this polymer are so close to each other that the electronic motion is practically isotropic in two directions; the conductivity reaches the values of $5 \cdot 10^5$ $\Omega^{-1} \cdot cm^{-1}$ at 4 K, below the critical temperature of $T_C = 0.26$ K superconductivity was observed.

As for the charge transfer complexes, about 15 years after Little's stimulating proposal, superconductivity in $(TMTSF)_2PF_6$ was observed [12]. These electronic quasi-1-dimensional organic metals based on the donor molecule TMTSF, the Bechgaard salts, show at low temperatures, in general, a phase transition to an insulating state. Only after applying pressure of a few kbar the insulating ground state is suppressed and superconductivity emerges at a temperatures of 2–3 K.

Since 1980, over 400 organic conductors have been synthesized, over 50 of which are superconducting. During this time the superconducting transition temperature in these materials increased from 1.2 K to 12.6 K [31].

This dissertation is devoted to investigations of a particular group of charge transfer salts – the Bechgaard salts, which we will introduce in the next section.

1.2   Bechgaard Salts

Typically organic chain compounds are formed by stacks of large cations separated by anions. The incomplete electron transfer leads to the formation of a partially filled band along the chain direction, and they show anisotropic behavior at room temperature. Most of these compounds share various ground states in temperature and pressure space. Our studies were done on the tetramethyletetraselenafulvalene-hexafluorophosphate [1] $(TMTSF)_2PF_6$.

---

[1]Tetramethyletetraselenafulvalene, shortly (TMTSF) or (TM), has a chemical composition $(CH_3)_4C_6Se_4$ and the official IUPAC name 4,4′,5,5′-tetramethyl$\Delta^{2,2'}$-bi-1,3-diselenolylidene.

1.2.1 Crystal Structure of Bechgaard Salts

The first $(TMTSF)_2X$ molecular crystals were synthesized in the late 1970s and are known as Bechgaard salts, after the name of the synthesizer Klaus Bechgaard [13]. While with various anions, X, they show highly conducting behavior at room temperature, the spin-density wave insulating state was found with anions of centrosymmetric PF_6^-, AsF_6^- and SbF_6^- or non-centrosymmetric NO_3^- and ClO_4^-.

The crystals are grown by the electrochemical reaction (Sec. 3.4). The structure [14] of these isomorphous crystals is shown in Fig. 1.3.

The unit cell structure is triclinic, with the anions at the inversion center of the $P\bar{1}$ space group [14]. The conduction chain is formed by a zig-zag stack of the nearly planar TMTSF molecules (the angle between the two halves of the molecule is $1.2\degree$) and each stack is separated by anions. The unit cell dimensions for several different salts are listed in Table 1.1. The shortest distance between the Se atoms in neighboring adjacent TMTSF molecules is 3.87 Å while the Van der Waals distance is 4 Å, suggesting a large overlapping of the electronic wave functions of the direction of the π-orbitals. The interplanar distance along the stacks alternates with 3.63 and 3.66 Å leading to a slight dimerization at room temperature; thus the mean value of the intermolecular distance is $a_s = 3.645$ Å . This interaction with anions folds the Brillouin zone into half of its size with 2 TMTSF molecules per unit cell. The top band has a concave up curvature. One anion takes away one electron from two TMTSF molecules resulting in a 1/4 filled hole band along the $(TMTSF)_2$ stacks. This partially filled band produces metallic conduction along the chain provided the intermolecular electron repulsion (the Hubbard U) is not strong compared to the bandwidth, i.e., $U < D$.

1.2.2 Role of Anions

To be more detailed, the position of anions, which can be categorized by their symmetry as shown in Fig. 1.3, is an inversion center of the three-dimensional structure [19]. Thus the non-centrosymmetric anions, such as NO_3^- and ClO_4^-, can be in either two

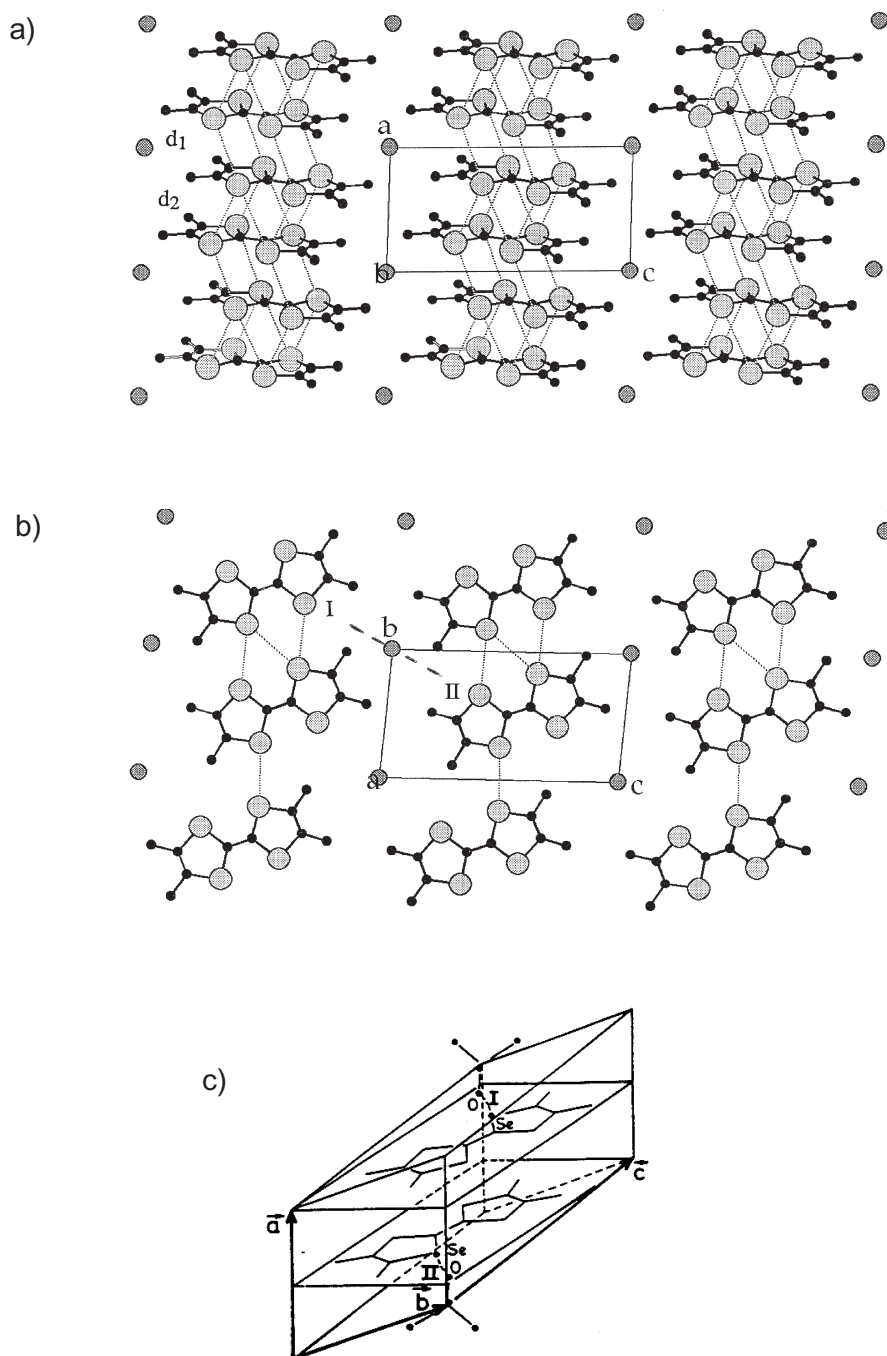Figure 1.3: Projection of the crystal structure of $(TMTSF)_2X$ on the $a-c$ plane (a), where the zig-zag structure can be clearly seen, and $b-c$ plane (b). The Se atoms are the large light gray circles, the carbon atoms are small black circles, and dark gray circles between the molecules denote anions. From Ref. [32]. (c) The triclinic unit cell of a salt with tetrahedral anions. From Ref. [33].

Anion $\mathbf{X}$	T_{AO} (K)	T (K)	a (Å)	b (Å)	c (Å)	α	β	γ	V_{cell} (Å^3)
AsF$_6$[a]	-	300	7.277	7.711	13.651	83.16	86.00	71.27	719.9
ClO$_4$[b]	24[e]	300	7.226	7.678	13.275	84.58	86.73	70.43	694.4
NO$_3$[c]	41	300	7.217	7.567	12.822	89.14	86.61	70.56	659.1
PF$_6$[b]	-	300	7.297	7.711	13.522	83.39	86.27	71.01	714.3
PF$_6$[d]	-	4	7.076	7.632	13.322	84.14	88.05	70.13	673.0
ReO$_4$[b]	180	300	7.284	7.751	13.483	83.23	86.56	70.08	710.5
SbF$_6$[b]	-	300	7.299	7.728	13.901	82.77	85.23	71.52	737.0
TaF$_6$[b]	-	300	7.280	7.716	13.918	82.88	85.37	71.67	735.6

Table 1.1: Anion ordering temperature T_{AO} and unit cell dimensions for several different Bechgaard salts (TMTSF)$_2\mathbf{X}$ at temperature T. Labels a, b, and c are the unit cell dimensions along the respective crystallographic axes. Labels $\alpha = \widehat{(b, c)}$, $\beta = \widehat{(a, c)}$, and $\gamma = \widehat{(a, b)}$ are the angles of a unit cell of volume V_{cell}. Note the substantial thermal contraction of the unit cell in (TMTSF)$_2$PF$_6$.
[a] Ref. [15]
[b] Ref. [16]
[c] Ref. [17]
[d] Ref. [18]
[e] Slowly cooled, typically $\Delta T / \Delta t < 100$ mK/min

equivalent positions introducing disorder. At low temperatures, interactions between the anions and the organic stacks [20, 21] lead to an anion ordering (AO) transition. When the anions are ordered at low temperature, the periodicity of the lattice is either doubled by alternating its orientation (BF_4^- and ReO_4^-), or not affected by uniform orientation (NO_3^-, ClO_4^-). The resulting superstructure is characterized by the wave vector which is identified by new reflection spots appearing in the X-ray pattern [20]. A list of the different AO transition temperatures T_{AO} is given in Table 1.1. Interestingly, having hexahedral centrosymmetric anions PF_6^-, the $(TMTSF)_2PF_6$ compound around 58 K the proton relaxation experiments indicate structural phase transition involving rearrangement of the PF_6 ions [22].

1.2.3   Band Structure and Electronic Properties

From the Fig. 1.3, it can be seen that the cation stacks are arranged in sheets which are separated by planes of anions. As we mentioned above, the intrastack molecular spacing is smaller than the sum of the Van der Waals radii of Se atoms, whereas the interstack spacing is nearly equal to (b direction) or much larger (c direction) than the sum of the Van der Waals radii. Describing the electron band within the tight-binding approximation, the linearized energy dispersion relation is given by [30]:

$$\varepsilon(\mathbf{k}) = -2t_a \cos(k_a \cdot a_s) - 2t_b \cos(k_b \cdot b) - 2t_c \cos(k_c \cdot c), \qquad (1.1)$$

where t_a, t_b, and t_c are the transfer integrals along the a, b, and c axes respectively, a_s is the intermolecular distance along the a-axis and k_i are the electron wave vectors in the ith direction. The lobes of the molecular π-orbitals point along the stacks and this, together with anisotropic Se-Se distance leads one to expect relations $t_a \gg t_b \gg t_c$.

For a purely one-dimensional (1D) system, i.e., completely neglecting the transverse overlap, the bandwidth is $4t_a$ and the density of states diverges at the band edges, with a minimum at zero energy (Fig. 1.4a). The Fermi surface of such a system consists of two planes separated by $2k_F$ when viewed in a 3D space , as shown in Fig. 1.4b, and this surface is perfectly nested ($\varepsilon_{\mathbf{k}} = \varepsilon_{\mathbf{k+Q}}$ for all $\mathbf{k}$ on the Fermi

surface) by the wave vector $\mathbf{Q} = (2k_F, 0, 0)$.

The three-dimensional band structure can be considerably simplified, if one does not consider any interaction in c-direction. Thus with $t_a \gg t_b$ and $t_c = 0$ the dispersion relation reduces to [30]:

$$\varepsilon(\mathbf{k}) = 2(t_b \cos(k_b \cdot b) \pm t_a \cos(\frac{1}{2}k_a \cdot a)) \tag{1.2}$$

Equation (1.2) provides a complete analytical description of the 2D or quasi-1D band structure of $(\text{TM})_2\text{X}$ which can be used as a basis for derivation of the electronic and transport properties [23].

The Fermi surface is determined by the condition

$$k_a = k_F + \frac{2t_b}{v_F} \cos k_b b + \bar{O}(t_b^2 \cos k_b b) \tag{1.3}$$

with $v_F = 2at_a \sin(ak_F/h)$. This leads, neglecting the third term in equation (1.3), to a sinusoidal Fermi surface in the k_a-k_b plane, as shown in Fig. 1.4c,d. While the Fermi surface of a strictly 1D conductor consists of two planar sheets intersecting the k_a axis at $\pm k_F$ (see Fig. 1.4c, dashed lines), the effect of the small transverse overlap t_b is to introduce some warping of the original planar Fermi surface. The wave vector $\mathbf{Q} = (2k_F, 0, 0)$ no longer nests the warped Fermi surface, but the new nesting vector $(2k_F, \pi/b, \pi/c)$ deviates from the perfectly nesting vector only with terms of the order $(t_b/t_a)^2$ [19, 25]. It is clear that the general trend of increasing t_b and/or t_c leads to a destruction of the nesting. Perfect nesting, as shown in Fig. 1.4c, is obtained only in the limit when $t_b/t_a \to 0$. With increasing t_b/t_a the last term in equation (1.3) becomes progressively more important and the nesting condition applies for a smaller number of electron-hole pairs [26].

The dimensionality of the system is defined by the ratio of the thermal energy $k_B T$ to the band parameters: t_a, t_b, and t_c. Whenever $k_B T/t_i \gg 1$ the motion is diffusive in the ith direction. In an anisotropic system one typically finds a temperature-dependent dimensionality with a cross-over to 3D behavior occurring only below temperatures $k_B T/t_i \ll 1$, for all i. With this in mind (and keeping our 1D tight-binding

a)

b)

c)

d)
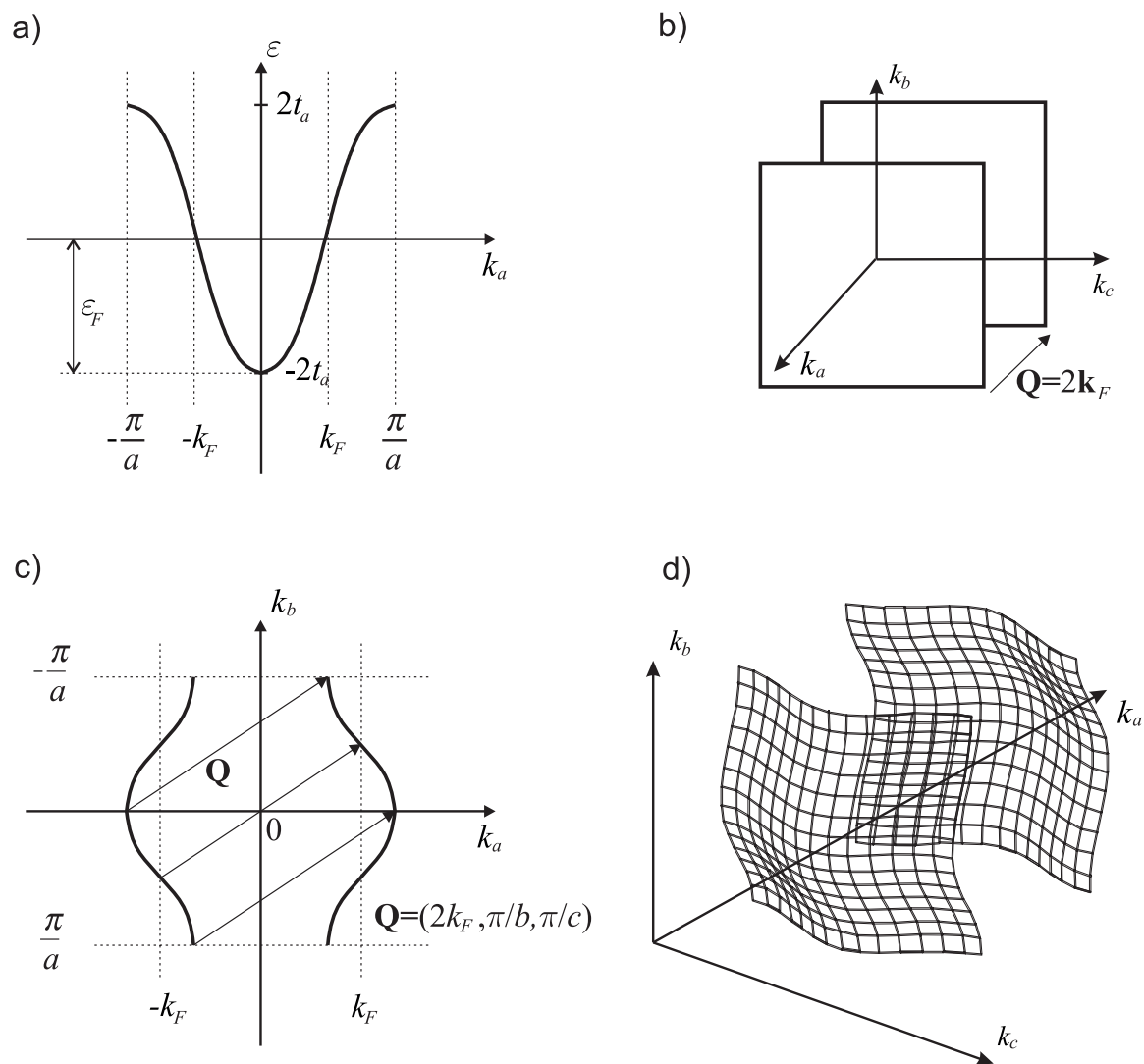
Figure 1.4: (a) The bandwidth of a purely 1D system, conducting along a-axes. (b) The Fermi surface of a purely 1D system, conducting along a-axes. (c) The solid curves represent the Fermi surface obtained by neglecting the 2$^{\mathrm{nd}}$ harmonic term in Eq. (1.3); the dashed lines show the flat Fermi surface in the absence of transverse coupling, after Ref. [31]. (d) The 3D view of the Fermi surface of a Q1D/2D system, corresponding to the solid curves in figure (c).

approach), the charge transfer of 1/2 electron per TMTSF molecule formally gives a 3/4 filled hole band (TMTSF is the donor). However, the slight dimerization found in these systems causes a zone folding, opening a small gap $\Delta(4k_F)$ at the zone boundary, thus leaving a 1/2 filled upper band. Typically, the dimerization $(\delta a/a)$ found in the TMTSF salts is *ca.* 0.8%, while the TMTTF (tetramethyltetrathiafulvalene, or "Fabre salts", the four selenium atoms of TMTSF are replaced by sulfur) salts have a more pronounced dimerization, *ca.* 2.8%, as found from the optical measurements [25].

In the tight binding approximation the mean free path, ℓ, is given approximately by [28]:

$$\ell = \frac{\sigma \pi \hbar}{2ne^2 a}, \tag{1.4}$$

where a and σ is the lattice constant and conductivity in the direction in question, respectively; n is the concentration of the charge carriers, and e is elementary charge.

The conductivity anisotropy is approximately given by the square of the band structure anisotropy. The conductivity across the chain is diffusive and can be related to the longitudinal conductivity by using the one dimensional Golden rule [27]. The resulting expression is

$$\frac{\sigma_a}{\sigma_\perp} = \left(\frac{t_a}{t_\perp}\right)^2 \left(\frac{a_s}{l}\right)^2, \tag{1.5}$$

where σ_a and $\sigma_\perp$ are the conductivities along and perpendicular to the chain axis; $a_s = a/2$ is the mean value of the intermolecular distance (see page 25 for more details), and $l =(b$ or $c)$ is the distance to the neighboring stack (see the lattice parameters in Table 1.1). Equation (1.5) shows, that the conductivity anisotropy should thus be temperature independent.

A more realistic approach incorporates the finite transverse coupling. P. M. Grant, to whom the quotation in the beginning of this chapter belongs, has performed a 3D band structure calculation and, considering only the highest occupied molecular orbitals (HOMO), he finds $(4t_a : 4t_b : 4t_c) = (1.5 : 10^{-1} : 3 \times 10^{-3})$ eV for the TMTSF

salts [24]. Such parameters lead to a strongly anisotropic system with open orbits
(at all temperatures) and a cross-over to 3D behavior below about 10 K. The energy
dispersion along XV and ΓV is shown in Fig. 1.5. In Table 1.2 we report the transfer
integrals t_a and t_b as taken from this band strucure calculation Ref. [24].
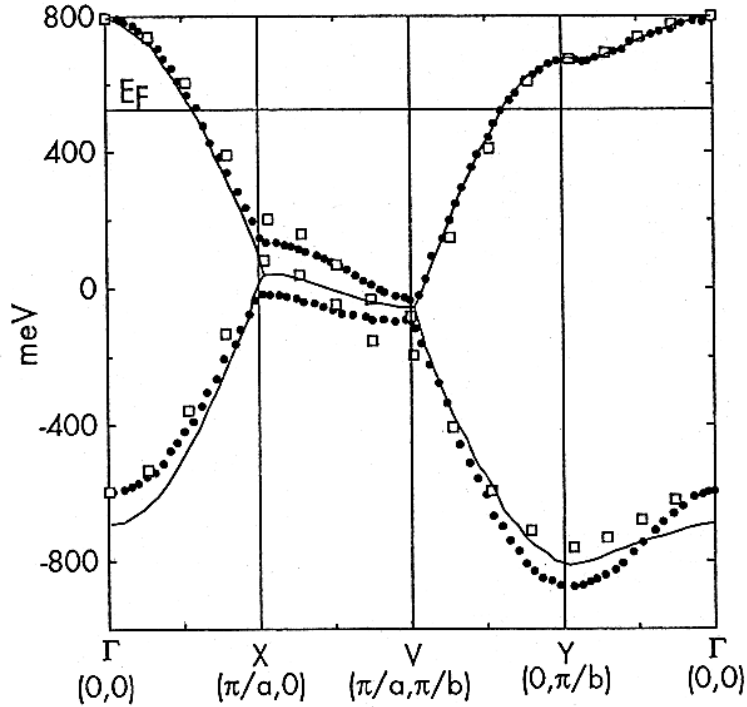
Figure 1.5: Band structure of $(TMTSF)_2AsF_6$, which is representative for all Bechgaard
            salts, as calculated by P. M. Grant [24]. The different symbols and the solid
            curve on the plot correspond to the different numerical procedures, which con-
            form with each other.

1.2.4 The Phase Diagram of Bechgaard Salts

A direct consequence of the pronounced 1D character of the $(TM)_2X$ series is the
existence of a wide variety of ground states that can be observed for various members
of the family. The nature of the ground state depends on such parameters as chemical
composition of the organic molecule or the inorganic anion, the hydrostatic pressure

	t_a (meV)	$t_{b'}$ (meV)
$(TMTSF)_2ClO_4$	366	21.6
$(TMTSF)_2NO_3$	391	23.9
$(TMTSF)_2PF_6$	365	26.2
$(TMTSF)_2ReO_4$	364	19.7

Table 1.2: Room temperature transfer intrastacks (t_a) and interstacks ($t_{b'}$) integrals of se-
lected Bechgaard salts. The transfer integrals differ due to the slightly different
unit cell parameters. From Ref. [24].

and an eventually applied external magnetic field. The generic phase diagram in
Fig. 1.6 displays the variety of ground states found in Bechgaard salts.

Thereby, the crucial parameter is pressure and not the charge-carrier concentra-
tion, as it known for high-temperature superconductors. Increased pressure is equiv-
alent with an increased overlap of the molecular wave functions, in particular perpen-
dicular to the direction of high conductivity (a-axis). This results in a reduction of
the anisotropy and, consequently, in an increase of the dimensionality. The arrows in
Fig. 1.6 indicate ambient-pressure starting points for different charge-transfer salts.
At the far left side of the phase diagram the $(TMTTF)_2PF_6$ is located, the sulfur
analog of $(TMTSF)_2PF_6$. At high temperatures of about 230 K this system shows
a smooth transition into an insulating state (loc), which is caused by localization of
the interacting electrons presumably due to a Mott-Hubbard transition. The anti-
ferromagnetically ordered spin chains lead to a spin-Peierls (SP) transition at about
15 K, where the lattice dimerizes with two neighboring spins forming a spin singlet.
Consequently, the magnetic energy of the crystal is reduced. By applying external
pressure of about 13 kbar, the transition into a localized state gets suppressed and
the system remains metallic until at lower temperatures a Peierls transition connected
with a spin density wave (SDW) occurs as a new ground state. The organic mate-
rials $(TMTTF)_2Br$ and $(TMTSF)_2PF_6$ have an increasingly larger dimensionality
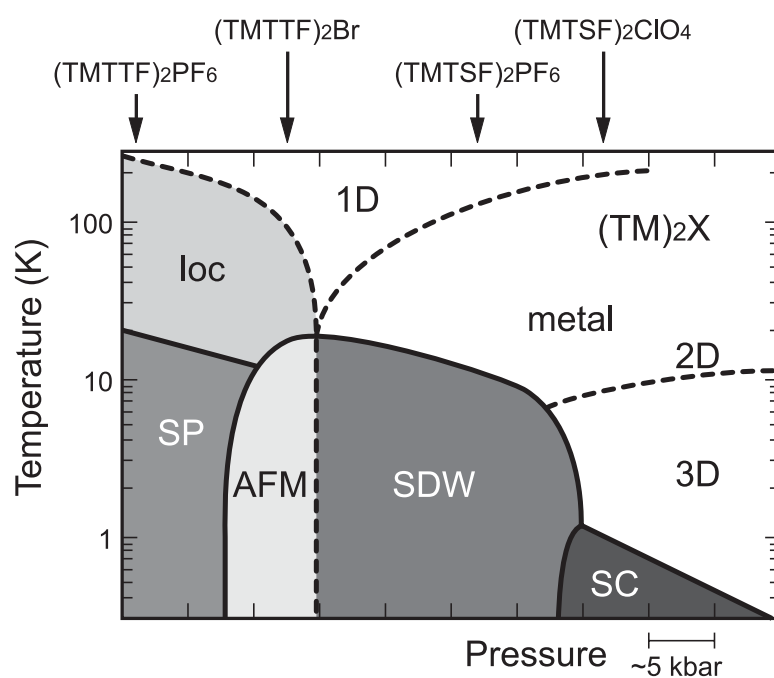
Figure 1.6: Generalized phase diagram for the $(TM)_2X$ series. The notations loc, SP, AFM, SDW and SC refer to Mott localized, spin-Peierls, antiferromagnetic (commensurate SDW), spin density wave (incommensurate), and superconducting ground sates, respectively. The dashed curves within the metallic phase mark the dimensional crossover regions. The arrows indicate the location at atmospheric pressure of the different compounds in the generalized diagram. Adopted from [29].

already at ambient pressure and show the SDW transition at correspondingly lower temperatures. Under a pressure of 26 kbar for $(TMTTF)_2Br$ [34] and about 6 kbar for $(TMTSF)_2PF_6$ [35], the metal-insulator transition is completely suppressed and superconductivity (SC) develops with transition temperatures of about 1–3 K. The only Bechgaard salt with low-enough anisotropy is $(TMTSF)_2ClO_4$, which becomes superconducting already under ambient pressure at about 1.4 K.

We will discuss these ground states in the next Chapter 2 "Low dimensional physics" in more details.

Chapter 2

Low-Dimensional Physics

"Nature is an infinite sphere whose center is everywhere."

— Emerson

Metals may undergo a phase transition to a state with a new type of electronic order. Iron and nickel, for instance, become ferromagnetic. In these materials, magnetic interactions cause an alignment of the spins of the conduction electrons, and an ordered state with nonzero magnetic moment is formed. Other metals, such as aluminum and lead, become superconducting. In superconductors, electrons of opposite momentum are grouped into pairs as a result of their interactions with lattice vibrations. Such Copper pairs can move through the superconductor without dissipation.

A different type of phase transition occurs in a class of metals with chain-like crystal structure, namely quasi-one dimensional materials.

In the charge-density-wave (CDW) state, the electron density is periodically modulated in space, and the ions are slightly displaced. The wavelength of this modulation can be both commensurate and incommensurate with the underlying lattice. The transition to the CDW state is named after Rudolph Peierls who in 1930 was the first to describe the mechanism for CDW formation [36].

CDWs bear a strong formal analogy to superconductivity. The CDW transition can be viewed as a Bose condensation of electron-hole pairs, similar to Cooper-pairs

forming a superconductor. Like superconductors, CDWs give rise to remarkable electron transport properties. In 1954, Fröhlich predicted that incommensurate CDWs can slide along the chains without dissipation as a result of translational invariance with respect to the lattice [37]. Such Fröhlich superconductivity has never been found experimentally. In real crystals, CDWs are pinned by impurities, and a finite electric threshold field must be applied to set the CDW into motion. CDW sliding was observed for the first time in 1979 as a sharp increase of conductance in NbSe$_3$ [38].

Another typical 1D low-temperature ground state is the spin-density-wave (SDW) state, which is due to electron-electron repulsive interactions. When electron-electron interactions are attractive, the superconducting ground state is formed. In Section 2.1 we will discuss in more detail the various broken-symmetry ground states found in Bechgaard salts.

In Section 2.2 we will finally concentrate on the normal state properties of systems of reduced dimensionality. We will introduce the most important properties of a Luttinger liquid (LL), which could serve as a model to describe the normal state of a strictly 1D interacting electron system in which interactions play a crucial role.

2.1   Quasi-1-D Ground States

2.1.1   Charge-Density Waves

Charge-density waves occur in conductors with a chain-like crystal structure. For such materials, the Fermi surface can be approximated by two parallel planes separated by a wavevector $2k_F$ (see Sec. 1.2.3). This particular topology leads to a response to external perturbations that is strongly different from that in three dimensions. Due to the large number of electron states at the Fermi-surface that differ by $2k_F$, the electron gas is unstable with respect to external perturbations of this wavevector. At low temperatures, both the charge density and the lattice sites (only in the commensurate case of 1/2 filling) are modulated by the corresponding wavelength $\lambda = \pi/k_F$.

A schematic representation of the CDW modulation is shown in Fig. 2.1 for a wavelength equal to twice the lattice parameter a (for the half-filling). The electron density ρ is given by

$$\rho(\mathbf{r}) = \rho_0 + \rho_1 \cos(2\mathbf{Q} \cdot \mathbf{r} + \phi) \tag{2.1}$$

in which $\mathbf{Q}$ denotes the net momentum of an electro-hole pair (total spin $S{=}0$), and ρ_1 denotes the CDW amplitude and ϕ is the CDW phase, which determines the position of the CDW with respect to the lattice. The distortion of the lattice sites has been exaggerated in the sketch; real distortions are typically less than 1% of the lattice constant. The new periodic potential lowers the electronic energy by opening a Peierls gap 2Δ at the Fermi energy. This energy gain overcomes the energy cost for distorting the lattice.

The opening of the Peierls gap has far-reaching consequences for the electrical transport properties. The material becomes a semiconductor, and transport can only occur through quasi-particles that are thermally excited across the gap. Typical gap values for Peierls semiconductors lie in the range of 20–200 meV, which is an order of magnitude smaller than for well-known band semiconductors such as silicon and germanium (1.12 and 0.66 eV at room temperature, respectively).

Since the wavelength of the CDW is determined only by the Fermi wavevector, there is no direct relation between λ and a. If the ratio λ/a is a rational number, the CDW is commensurate with the underlying lattice and the CDW energy depends on its phase. In the ground state, the phase is such that the energy is minimized, and a force is required to push the CDW out of this potential minimum. For incommensurate CDWs, on the other hand, λ/a is irrational, and the CDW is translationally invariant with respect to the underlying lattice.

Due to this translational invariance, incommensurate CDW can slide through the lattice . But in real materials the CDW is pinned to the impurities and to the crystal imperfections (such as micro cracks, for example), and the CDW can slide when a moderate electric field is applied. Then the CDW is depinned from impurities, and a
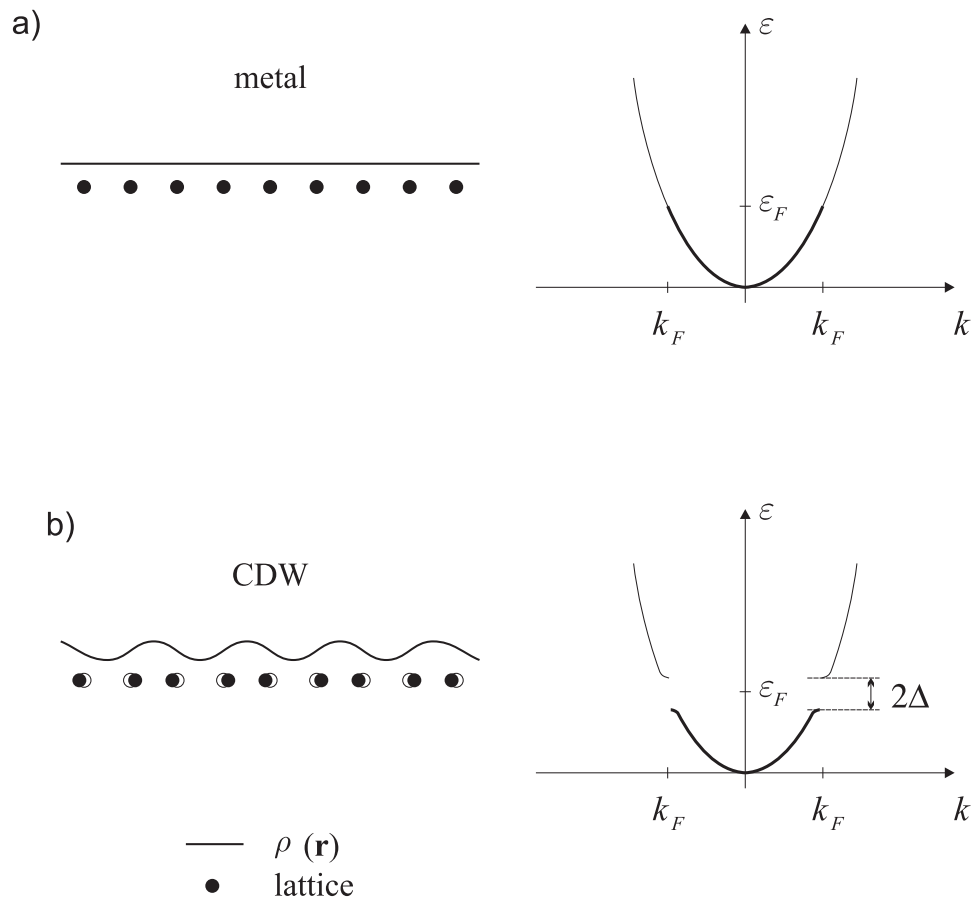
a)

metal

b)

CDW

$\rho\,(\mathbf{r})$

lattice

Figure 2.1: Charge-density-wave formation. A sketch of the spatial variation of the net charge density in both the metallic (a, left figure) and CDW (b, left figure) states. In the band structure, a gap 2Δ opens at the Fermi energy (b, right figure). The thick line denotes filled states at $T = 0$.

current is carried by the collective motion of the CDW electrons. CDW sliding causes nonlinear voltage-current characteristics.

One of the most appealing phenomena originating from CDW sliding is the appearance of coherent current oscillations, also known as narrow-band noise. If a DC current is applied between the contacts of a sliding-CDW conductor, an AC voltage component is measured in addition to the normal DC response. The frequency of this AC response is proportional to the CDW current, with a proportionality constant that only depends on the number of current-carrying chains. Typical internal frequencies in CDW crystals are in the range of 1–100 MHz.

Several models have been proposed to describe the sliding CDW motion in the presence of impurities. A simple model is the single-particle model [39]. This model treats the CDW as a rigid object moving in a periodic pinning landscape ("washboard potential"). Applying an electric field corresponds to tilting the washboard. For low fields, the particle remains trapped in a trench of the washboard, and the CDW is pinned. Sliding occurs if the applied electrical field E exceeds the threshold field E_T ($E > E_T \sim 0.5$ V/cm), when the washboard tilt is strong enough for the particle to come out of the trench and roll down. The single-particle model can qualitatively predict several phenomena associated with CDW sliding. For instance, the presence of coherent current oscillations in the response to a DC signal can easily be visualized with a rigid object bumping down a washboard. For a quantitative comparison with experimental data, however, the single-particle model is in most cases an oversimplification.

A more elaborate and widely-used model of CDW motion has been worked out by Fukuyama, Lee, and Rice in the late seventies [40, 41]. In FLR model, the CDW is an elastic medium which can adjust itself at impurity sites. Two regimes can be identified. In the strong-pinning regime, the pinning strength of impurities dominates over the elastic energy of the CDW, and the CDW phase is fully adjusted at each impurity. In the weak-pinning regime, on the other hand, the CDW elastic force is stronger than the impurity-pinning force, and the CDW phase is only partially

adjusted at each impurity. In this case, the phase coherence length can extend over many impurities. The classification of CDW conductors into weak-pinning and strong-pinning materials has been the subject of intensive research and debate [42, 43, 44, 45].

2.1.2   Spin-Density Waves

While the Peierls transition and the phenomena related to it are a consequence of electron-phonon interactions, electron-electron interactions can also play a significant role in the dynamics of low-dimensional systems. In particular, such interactions, either attractive or repulsive, can lead to broken-symmetry ground states such as superconductivity (SC) and spin density waves (SDW). It was Overhauser who first realized that the paramagnetic state of an interacting electron gas is unstable with respect to the formation of a static spin density wave [46, 47]. In analogy to the case of the CDW, the ground state consists of electron-hole pairs with total spin $S = 1$ and net momentum $\mathbf{Q}$, and is characterized by a spatial modulation of the electronic spin density:

$$\mathbf{S}(\mathbf{r}) = \mathbf{S}_1 \cos(\mathbf{Q} \cdot \mathbf{r} + \phi), \tag{2.2}$$

where S_1 and ϕ are the amplitude and phase of the electronic spin density, respectively. The existence of such a state has been well established and extensively studied, and several comprehensive reviews have been written [26, 61].

The simplest way to visualize the SDW is to imagine that a SDW actually is a split CDW: it consists of a wave for spin-up ($\uparrow$) electrons and another one for spin-down ($\downarrow$) electrons with a phase shift $180\,°$ between spin-up and spin-down wave. The splitting is intruduced by electron-electron interactions. Because of the phase shift the corresponding lattice distortions interfere destructively and there is no net distortion, i.e. the SDW is accompanied by no lattice distortion. Therefore, a SDW cannot be detected by structural investigations (X-ray or neutron scattering), however, local susceptibility measurements turn out to be very powerful such as ESR (electron spin resonance) and NMR (nuclear magnetic resonance), the latter because of the hyperfine interaction through which electronic spins relax the nuclear spins [61].
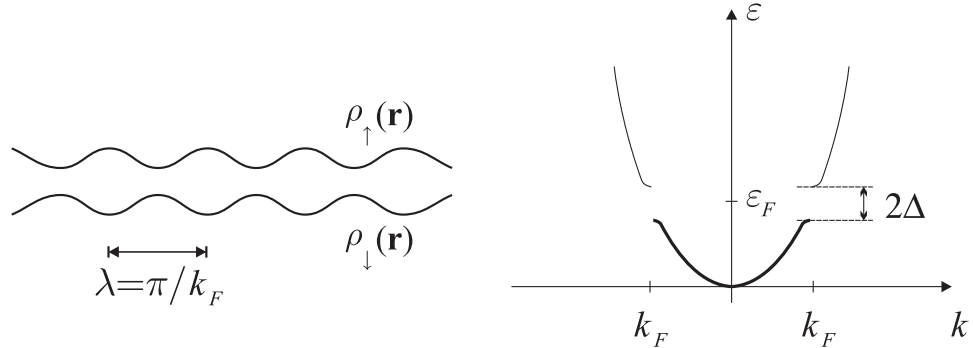
Figure 2.2: A plot of the spacial variation of the spin up ($\uparrow$) and spin down ($\downarrow$) waves forming an SDW state. The depicted phase difference is $180\,^{\circ}$.

Because the SDW is pinned for a small applied field and the gap opens for all sates on the Fermi surface, electrical conduction is caused by single particle excitations above the gap. Since the number of carriers is proportional to the Boltzmann factor $\exp(-\Delta/T)$, the low temperature resistivity in the SDW state roughly obeys

$$\rho \propto \exp(\Delta/T). \tag{2.3}$$

with SDW gap values of ~ 1 meV.

Similar to CDWs, for electric fields larger than a threshold E_T, the SDW can brake free from the pinning potential landscape and additional current from the SDW results. This feature is seen in the nonlinear DC current *versus* voltage and broadband noise generated by the sliding SDW. Typical static threshold fields for $(\text{TMTSF})_2\text{PF}_6$ are 3.5 mV/cm [48].

In general, SDW transition temperatures are significantly smaller (around 10 K), often by an order of magnitude or more, than those in CDW compounds. In addition, the calculated mean field transition temperatures for materials with SDW ground states are typically very close to the actual transition temperatures, and the fluctuation regime is rather narrow. However, despite this fact, the normal state properties of these materials are not necessarily characteristic of simple metals. This

fact will be discussed in more detail below in Sec. 2.2 and examined experimentally in Chapter 5.

2.1.3   Superconductivity

As mentioned above, these two ground states (CDW and SDW) are the result of Fermi-surface instabilities whose effects are enhanced due to the reduced dimensionality.

Superconductivity is another ground state common to systems with interacting Fermi surface electrons. A quick glance at Table 2.1 shows that, with the notable exceptions of $(TMTSF)_2BF_4$ and $(TMTSF)_2NO_3$, all of the Bechgaard salts listed display a transition to a superconducting ground state (usually external pressure and low temperatures are required). However, as a SC consists of electron-electron pairs with zero net momentum, the Coulomb repulsion between electrons must be overcome in order to form a pair. Typically (within the BCS theory, see the next section), the bare repulsion is overcome by the retarded electron-phonon interaction. Within this picture, the lattice polarization induced by one electron slowly decays, and can therefore attract a second electron for some time after the first electron has moved away. However, in 1D the retardation is not so effective, as the reduction in the phase space available makes it difficult for two electrons moving in opposite directions to avoid one another [59]. The upshot is that superconductivity is always a 2D or 3D phenomenon and therefore should usually not compete with either a CDW or a SDW ground state. This was reconciled with the observed SC state in these Q1D salts, by the large, experimentally measured [60] decrease in the anisotropy (increased dimensionality) under pressure.

The picture which emerges is that of a family of salts where the charge transfer is complete and the conduction takes place solely along the TMTSF chains. The phase transitions observed at low temperature are tied to the Fermi surface instabilities. Yet, the dominant response function is determined in part by the dimensionality of the system, which depends on the molecular overlap in the transverse direction and

Material	Metal-Insulator	Ground State	SC*	SC*
	T_{MI} (K)	Ambient Pressure	P_C (kbar)	T_C (K)
$(TMTSF)_2BF_4$	38	AO	-	-
$(TMTSF)_2ClO_4^\dagger$	24	SC	0	1.2
$(TMTSF)_2ClO_4^\ddagger$	6	SDW	-	-
$(TMTSF)_2ReO_4$	180	AO	9.5	1.3
$(TMTSF)_2NO_3$	41	SDW	-	-
$(TMTSF)_2AsF_6$	12	SDW	12	0.9
$(TMTSF)_2PF_6$	12	SDW	6.5	1.2
$(TMTSF)_2SbF_6$	12	SDW	11	0.4
$(TMTSF)_2TaF_6$	11	SDW	12	1.4

Table 2.1: Characteristics of the phase transitions seen in the $(TMTSF)_2X$ salts.
[†] Slowly cooled, typically $\Delta T/\Delta t < 100$ mK/min
[‡] Quenched
[*] Under pressure, most of the salts show a low-temperature transition to a superconducting state. P_C is the minimum pressure required to observe such a transition and T_C is the maximum temperature at which superconductivity can be observed.

therefore is sensitive to the effects of pressure and/or anion size and shape. One manifestation of this sensitivity to dimensionality is, as displayed in Fig. 2.3, the strong dependence of the critical pressure on the b-axis lattice constant. One can see that the two effects (i.e. pressure and increasing anion size) compete and one is left with a system where the dimensionality can effectively be "tuned".

Thus, it turns out to be very important to perform reliable measurements of the anisotropy of Bechgaard salts, this dissertation is devoted to, since the anisotropy (or dimensionality) is the key feature for the formation of this or that type of low-temperature ground state.
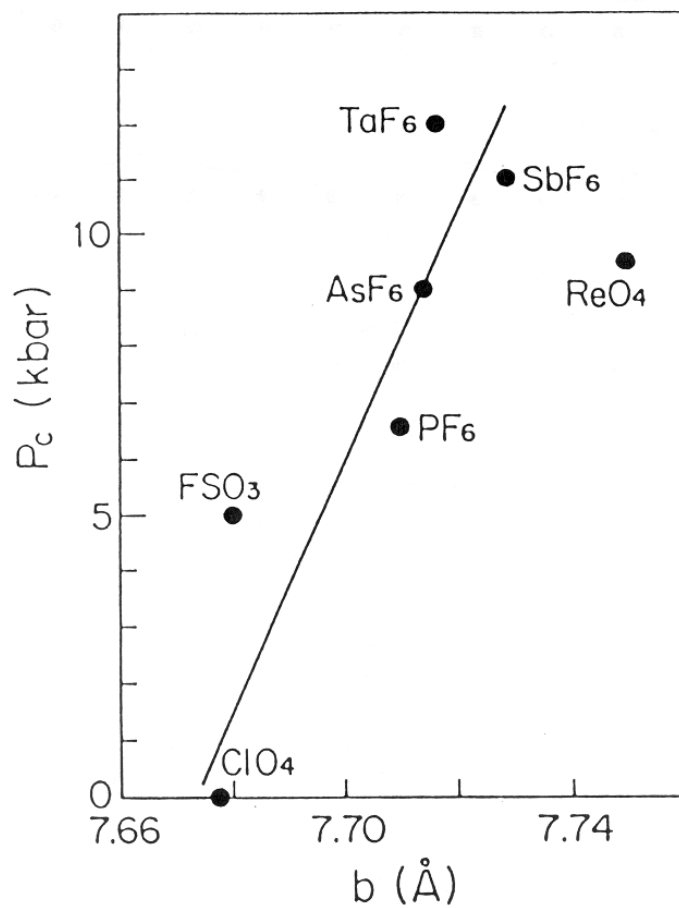
Figure 2.3: The relationship between P_C, the critical pressure above which the ground state is superconducting, and the b-axis parameter in several different Bechgaard salts. After Ref. [31].

2.1.4 BCS Theory

The general microscopic theory of superconductivity was developed by Bardeen, Cooper and Schriffer (BCS) in 1957 [50, 51]. The fundamental aspect of the model was that, in the presence of an attractive interaction, electrons in the neighborhood of the Fermi surface condense into a new ground state formed of electron-pairs with equal and opposite momentum and opposite spin components called Cooper pair: $(\mathbf{k}, \uparrow)$ and $(-\mathbf{k}, \downarrow)$ Bloch states. The attraction between the electrons in a pair can in principle be due to any suitable kind of interaction that overcomes the Coulomb repulsion (*e.g.* magnetic interaction, coupling by polarons or excitons). The energy required to break a pair is $2\Delta(T = 0)$. In 1950 Fröhlich suggested that the attractive interaction of the electrons in the solid is mediated by lattice distortions (phonons) [52]. The discovery that for many superconductors the transition temperature T_C depends on the isotope mass [53], supported this proposal. In this case, the transition temperature scales as the Debye temperature (T_D). Early, it was anticipated that other mechanism could also lead to the same pairing, but so far conclusive examples have not been found. Although the BCS theory was developed for superconductivity, its principle, the mean-field theory, is general enough to apply for every type of pairing (for example CDW and SDW order).

One of the main characteristics of the condensed phase is that the quasiparticle excitation spectrum has an energy gap $2\Delta(0)$ at zero temperature. In the BCS model, this gap is isotropic and independent of the $\mathbf{k}$ direction. A cut-off energy ($\hbar\omega_C = k_B T_D$) fixes the neighborhood of the Fermi level affected by the attractive interaction. $N(0)$ is defined as the single-spin electron density at the Fermi energy and V represents the interaction energy between the electrons. In the weak coupling limit ($T_C \ll T_D$) or $VN(0) \to 0$, the amplitude of the gap takes the limiting form:

$$\Delta(0) \sim 2\hbar\omega_C e^{-1/N(0)V}. \tag{2.4}$$

The transition temperature can be then estimated from the gap value:

$$2\Delta(0) = 3.528\, k_B T_C. \tag{2.5}$$

The temperature dependence $\Delta(T)$ is inferred from the famous "gap equation"

$$1 = VN(0) \int_0^{\hbar\omega_C} du \, \frac{\tanh(\sqrt{u^2 + \Delta^2(T)}/2k_BT)}{\sqrt{u^2 + \Delta^2(T)}}. \tag{2.6}$$

2.1.5   Other Pairing Symmetry

The basics of the BCS theory shown in the previous section can be extended to any other type of pairing mechanism [49]. For example, one can use the same tools to grind through the CDW ground state. The CDW ground state couples an electron and a hole of opposite spin at the antipode of the Fermi surface: $(\mathbf{k},\uparrow)_e$ and $(\text{-}\mathbf{k},\downarrow)_h$. Other possible pairing symmetries include:

- SS (singlet superconductivity), coupling two electrons of the opposite spin and opposite momentum $(\mathbf{k},\uparrow)_e$ and $(\text{-}\mathbf{k},\downarrow)_e$ ("classical" BCS superconductivity);

- TS (triplet superconductivity), coupling two electrons of the same spin, but opposite momentum $(\mathbf{k},\uparrow)_e$ and $(\text{-}\mathbf{k},\uparrow)_e$ (never observed without controversy);

- SDW, coupling an electron $(\mathbf{k},\uparrow)_e$ to a hole $(\text{-}\mathbf{k},\uparrow)_h$ of the same spin.

2.1.6   Spin-Peierls State

It is important to mention that another ground state occurs in these materials which is not due to a Fermi surface instability. This state is found at low temperatures in the TMTTF salts (a sulfur analog of TMTSF) and is characterized by a lattice distortion at $2k_F$ [62, 63] together with a rapid freeze out of the susceptibility below the critical temperature T_{SP} [64].

The nature of the SP transition can be explained by the following simple picture. Let us consider a magnetically ordered spin chain, known as Heisenberg spin chain. The spins can order ferromagnetically (all parallel) or antiferromagnetically (up and down alternating). The Heisenberg chain has collective excitations, the magnons. If
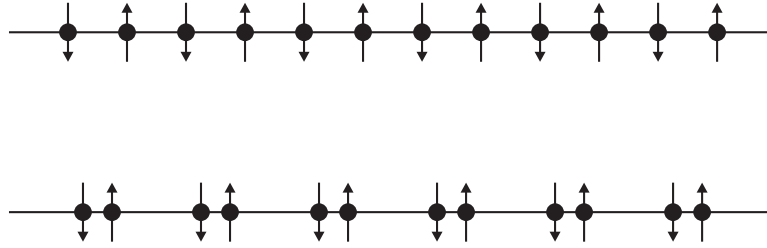
Figure 2.4: Spin-Peierls transition. The chain of equidistant electrons (Heisenberg chain) orders magnetically. The magnetic energy can then be lowered by approach of the electrons in pairs.

the equidistant electron arrangement is changed into a pair arrangement as indicated in Figure 2.4, the magnon energy can be lowered in a way similar to the lowering of the electron energy in the Peierls transition. The lattice adjusts to the paired electrons, the elementary cell is doubled and the lattice distortion is again found at $\pi/2a$. Because of the analogy to the Peierls instability, this transition is called a spin-Peierls (SP) transition.

2.2 The Luttinger Liquid

In order to understand the phase transitions discussed above, in particular the SDW formation, it is crucial to understand the dynamics of interacting electrons in their normal state. Landau's well known Fermi liquid (FL) theory [65], which describes the excitations of the interacting system, the so-called quasi-particles, as a gas of non-interacting particles, gives a good description of interacting fermions in 3D, for excitation energies small compared to the Fermi energy. A quasi-particle emerges from a free electron gas upon adiabatically switching on the electron-electron interactions. Those electrons form a cloud of finite diameter due to screening around the dressed electron. The quasi-particle keeps all the characteristic quantum numbers of a bare particle. However, the kinetic parameters as the effective mass or the dispersion velocity are renormalized. The quasi-particles with typical energies $\varepsilon \sim 25$ meV are robust against small displacements away from the Fermi surface ($\varepsilon_F \sim 0.8$ eV) with

a lifetime $\tau \propto (\varepsilon - \varepsilon_F)^{-2}$, leading to the well-known T^2 temperature dependence of resistivity [49].

The FL picture breaks down in 1D because of less stringent phase space restrictions on particle-particle interactions. An approach to this problem which has attracted much attention in recent years is known as "bosonization". It is based on the fact that in 1D long wavelength CDW and SDW oscillations, constructed by the combination of electron-hole pair excitations at low energy, form extremely stable excitations. These actually have no space available to decay, in contrast to the situation found in a FL where a damping exists. Quasi-particles are absent at low energy for a 1D system of interacting electrons and are replaced by collective acoustic excitations for both spin and charge degrees of freedom which turn out to be true eigenstates of the system. This description in terms of non-interacting boson fields is the basis of what has come to be known as the Luttinger liquid (LL) picture [66], which has received considerable attention in recent years [67, 68]. This renewed interest for the properties of the LL was stirred up by Anderson's proposal [69, 70] that the normal state properties of high-T_C superconductors, which can not satisfactory be described by a FL picture [71, 72], could be described by a hypothetical LL in 2D. While there is no consensus on this issue and indeed others have argued for FL [73, 74] or "marginal FL" [75, 76, 77] physics, attention has certainly been refocused on understanding the physics of interacting electrons in low dimensions. An alternative field of research for typically 1D correlations and eventual evidence in favor of a LL picture could be provided by organic and inorganic quasi-1D metals whose normal state properties show significant deviations from FL behavior. Due to their strongly anisotropic physical properties, these materials are excellent systems in which to study 1D physics. A family of quasi-1D metals is the Bechgaard salts, introduced in Chapter 1. Both, nuclear magnetic resonance (NMR) [78, 79] and (partially) angle-resolved photoemission measurements (APRES) [80, 81] on these compounds provided evidence in favor of a LL behavior, as we will see in Chapter 4. This was a part of the motivation to examine the microwave properties of the normal state of a

representative of the Bechgaard salts, namely $(TMTSF)_2PF_6$, with focus on possible evidence for LL behavior.

The theoretical predictions of the LL model have been extensively covered in several review articles [67, 68, 82]. Therefore we will limit the discussion to a survey of some of the most important results. The key features of a LL are:

- spin-charge separation, leading to a fractionization of the electrons into charged, spinless, and neutral, spin-carrying collective excitations: holons ρ $(S = \pm 1/2, q = 0)$ and spinons σ $(S = 0, q = \pm e)$, with different dynamics determined by velocities $v_\rho \neq v_\sigma$;

- correlation functions with non-universal power laws, parametrized by one renormalized coupling constant K_ν per degree of freedom $\nu = \rho$ charge, σ spin which can be viewed as the 1D equivalents of the Landau parameters of a FL;

- each of the above features leads to the absence of fermionic quasi-particles [83, 84].

2.2.1 Bosonization Formalism

As there are no fermionic quasi-particles in a LL, the problem can be treated by a procedure known as bosonization, a representation when all excitations of an 1D system can be described in terms of density oscillations [59, 66, 89].

The Hamiltonian describing the excitations of the fermionic system is expressed as a sum of the bosonic terms, one involving charge field and the other only spin fields [67]:

$$H = \mathcal{H}_\rho + \mathcal{H}_\sigma. \tag{2.7}$$

The bosonic Hamiltonians $\mathcal{H}_\rho$ and $\mathcal{H}_\sigma$ can be expressed as [67, 90]:

$$\mathcal{H}_\nu = \frac{1}{2\pi} \int dx \left[(u_\nu K_\nu)(\pi \Pi_\nu)^2 + \left(\frac{u_\nu}{K_\nu} \right) (\delta_x \phi_\nu)^2 \right], \tag{2.8}$$

where all of the interaction effects are hidden in u_ν, the propagation velocities of the charge and spin excitations, and in K_ν, the LL coefficient controlling the decay

of correlation functions. These LL parameters can be viewed as the 1D equivalents of the Landau parameters of a FL. Π_ν and ϕ_ν are canonically conjugate variables satisfying the Bose commutation relation

$$[\phi_\nu(x), \Pi_\mu(y)] = i\delta_{\nu\mu}\delta(x-y).\tag{2.9}$$

The quantities $\delta_x\phi_\nu$ give the deviations of the charge and spin densities from their average values, and Π_ρ is proportional to the current density.

The model described by the Hamiltonian (2.7) can be solved exactly. It describes the electrons in a gapless one-band 1D system in the vicinity of the Fermi surface. The spectrum shows only collective excitations with bosonic character and all the properties of the model then become entirely governed by the velocities u_ν and the parameter K_ν of acoustic excitations, which are functions of the microscopic coupling constants and differ for the charge and spin. The eigenstates of this Hamiltonian (Eq. (2.7)) are independent long wavelength oscillations of the charge and spin densities with linear dispersion relations $\omega_\nu(k) = u_\nu|k|$, therefore the system is conducting. For a noninteracting system, the velocities of the charge and the spin excitations would be the same $u_{\rho,\sigma} = v_F$ and $K_{\rho,\sigma} = 1$ This latter situation describes then free 1D fermions with $U = 0$ (if one considers the 1D Hubbard model).

When electron-electron interactions are turned on ($U \neq 0$), the values of K_ν are modified. The renormalized value of K_σ can be calculated or, if applicable, fixed to unity by the requirement of spin-rotation invariance [82]. One consequence of the modification of K_ρ is that there is no universal power-law decay of correlation functions in the LL. In addition, the interactions will cause the separation of the Hamiltonian into spin and charge parts, a peculiar feature of LL, which will be discussed below.

2.2.2   Spin-Charge Separation

One of the most spectacular key features of the LL model is the complete separation of the dynamics of the spin and charge degrees of freedom. In general, one has $v_\rho \neq v_\sigma$,

i.e. the charge and spin oscillations propagate with different velocities. The concept of spin-charge separation can be visualized very easily by a simple picture [67]. We consider a piece of a half-filled Hubbard chain. Then, for strong U there will be no double-occupied sites, and because the strong short-range antiferromagnetic order the typical local configuration will be

$$\uparrow\downarrow\uparrow\downarrow\uparrow\uparrow\downarrow\uparrow\downarrow\uparrow\downarrow\uparrow\downarrow \,.$$

Introducing a hole will lead to

$$\uparrow\downarrow\uparrow\downarrow\uparrow\uparrow\downarrow\uparrow \circ \uparrow\downarrow\uparrow\downarrow\uparrow\downarrow,$$

and after moving the hole by a few lattice sites the configuration is as follows:

$$\uparrow\downarrow\uparrow\downarrow \circ \uparrow\uparrow\downarrow\uparrow\uparrow\downarrow\uparrow\downarrow\uparrow\downarrow \,.$$

Note the hole, which was originally surrounded by two up spins, has split into a hole bracketed by antiferromagnetically aligned spins (called a "holon") and an object with two adjacent up spins, containing an excess spin 1/2 with respect to the initial configuration (called a "spinon"). This spinon can, of course, propagate via spin exchange process leading, for example, to

$$\uparrow\downarrow\uparrow\downarrow \circ \uparrow\uparrow\downarrow\uparrow\downarrow\uparrow\downarrow\uparrow\uparrow\downarrow \,.$$

Thus, we see that a single excitation can split into two excitations, one with charge and one with spin, with different velocities.

This charge-spin separation is one of the most interesting features of the Luttinger liquid, though it is difficult to study experimentally. For the first time it was experimentally investigated [54] by photoemission-based techniques on an artificial system of chains of Au atoms on Si(111) insulating substrate. The successful experiments on real materials were performed only recently, a wide class of Q1D Bechgaard salts were clearly indicate the separation of spin and charge degree of freedom in transport, sensitive to charge dynamics, and electron spin resonance (ESR), sensitive to spin dynamics, measurements [55]. The latter work was confirmed by thermal conductivity experiments [56].

2.2.3   Physical Properties of a Luttinger Liquid

The simple form of the LL Hamiltonian (Eq. (2.7)) makes the calculation of physical properties of a LL rather straightforward. The low-temperature specific heat can be shown to be linear in temperature, with a coefficient given by [67]:

$$\gamma/\gamma_0 = \frac{1}{2}(v_F/u_\rho + v_F/u_\sigma), \tag{2.10}$$

where γ_0 is the specific heat coefficient of non-interacting electrons of Fermi velocity v_F. Similarly the spin susceptibility can be written as

$$\chi/\chi_0 = v_F/u_\sigma, \tag{2.11}$$

where again χ_0 indicates the non-interacting value.

We see that apart from renormalization u_ρ, u_σ and K_ρ, these properties are the same as those of a FL. However, this system is not a FL, and this can be seen by considering the single-particle Green's function by using bosonization [91] in order to obtain momentum distribution function in the vicinity of k_F at $T = 0$ (Fig. 2.5) [67]:

$$n_k \approx n_{k_F} - \beta\text{sign}(k - k_F)|k - k_F|^\alpha, \tag{2.12}$$

where β is a model-dependent constant. The parameter α is called anomalous dimension and is given in terms of K_ρ (assuming spin-rotation invariance, i.e. $K_\sigma = 1$) as

$$\alpha = (K_\rho + 1/K_\rho - 2)/4 \geq 0. \tag{2.13}$$

and therefore is interaction dependent. It does not depend on the sign of the interaction but only on its strength and range. For the noninteracting case ($K_\rho = 1$) α is zero.

The single particle density of states near k_F is found to be

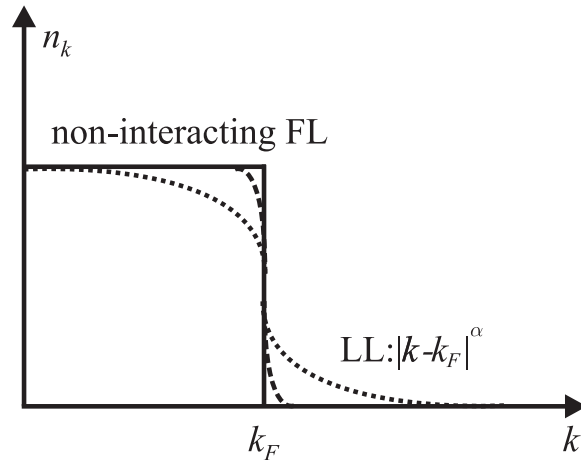$$D(\omega) \approx |\omega|^\alpha. \tag{2.14}$$

Figure 2.5: Fermi distribution at $T = 0$ for a non-interacting electron gas (solid curve), an interacting Fermi liquid (dashed curve), and a Luttinger Liquid (dotted curve) showing no discontinuity of n_k at $k = k_F$. From Ref. [85].

Thus, it is clear that for any interaction ($K_\rho \neq 0$) the distribution function and density of states have power-law singularities at the Fermi level, with a vanishing single-particle density of states at E_F, contrary to a standard FL which would have a finite density of states and a step-like singularity in n_k (Fig. 2.5).

The transport properties of the LL depend on the scattering mechanisms. If we consider electron-electron scattering in a band with filling factor $1/n$, we obtain from the current-current correlations [57]

$$\rho(T) \sim T^{n^2 K_\rho - 3}, \tag{2.15}$$

$$\sigma(\omega) \sim T^{n^2 K_\rho - 5}. \tag{2.16}$$

The second law has apparently been observed in Bechgaard salts [58].

2.2.4 A System of Weakly Coupled Luttinger Chains

While there were several successful issues to describe the longitudinal transport and optical properties of quasi-1D Bechgaard salts within a framework of LL theory, the nature of finite transverse conductivity is still under debate. Recently, a theoretical

work was devoted and focused on interchain transport and optical response of Q1D
Bechgaard salts [86] describing it by a model of weakly coupled Luttinger chains. It
was shown, that the interchain conductivity for the simplest case of weakly coupled
metallic Luttinger liquids obeys

$$\sigma_\perp(T,\omega) \propto (T,\omega)^{2\alpha-1}, \tag{2.17}$$

where α is the Fermi surface exponent (see Eq. (2.13)).

Several experimental results on transverse transport properties of $(TM)_2X$ were
tried to be interpreted in the framework of this theory [87, 88], although unsuccess-
fully.

Chapter 3

Experimental

"There is no higher or lower knowledge, but one only, flowing out of experimentation."

— Leonardo da Vinci

Frequency-dependent measurements were always essential for studying the electrodynamic properties of materials and solids. At low frequencies (kHz and MHz), contacts can be attached to the sample and the complex response of the material can be determined by lock-in techniques, network analyzers, impedance analyzers. These methods, however, fail in the GHz frequency range because the wavelength becomes comparable to the cable length, and capacitance and inductance between the wires can obscure the sample properties.

For this reason since the early 1950s the cavity perturbation technique (CPT) has been extensively employed for studying the dielectric and magnetic properties of materials at microwave frequency, when the GHz-frequency-range sources of the electro-magnetic (EM) radiation became available. This technique was pioneered by Slater [92] and co-workers. Nowadays this contact-free technique is still one of the most widely used because of its high sensitivity and relative simplicity.

A microwave resonant cavity is a box fabricated from high-conductivity metal (usually from oxygen-free copper) with dimensions comparable to the wavelength.

Often it has rectangular or cylindrical form, because in a resonator of complicated shape, it may be nearly impossible to calculate the distribution of electric and magnetic fields. While in the case of right or simple geometrical form these distributions are well-known and calculated for a long time.

At resonance, the cavity is capable of sustaining microwave oscillations, which form an interference pattern (standing wave configuration) from superposed microwaves multiply reflected from the cavity walls. Each particular cavity size and shape can sustain oscillations in a number of different standing wave configurations called *modes.*

There are many ways of using cavity perturbation to characterize the microwave properties of materials, but the principle of operation is similar in all cases. Samples are placed in the vicinity of a microwave resonator, with some provision made for varying the sample temperature. The change in the resonant frequency and the quality factor upon introducing a sample inside the cavity is the basis of the cavity perturbation technique.

Historically, the microwave range of frequency was approached both "from below" and "from above", by means of more traditional low-frequency (up to MHz) and optical (starting with FIR) measurements, respectively[1]. Only since the 1950's the mm-wave gap between conventional electrical low-frequency measurements and optics was covered by the rapid developing of the microwave technique, which became available for physicists, which were already familiar at that time with the neighboring ranges of the EM spectrum. This is the reason why there is almost no "microwave language", and people rather use a typical terminology of both electrical (resistance, reactance, impedance, and so on) and optical (reflectivity, refractive index, etc.) terms for the microwaves. Hereinafter in this chapter we will just call all the physical parameters as "optical".

---

[1]Some people can raise an objection against the optical spectroscopy as an old tool. To my opinion, it is ancient and maybe the first scientific method of investigation of nature. We should not forget about the "everyday optical spectroscopy": gems are colored and transparent and metals are opaque and shiny, this was observed since thousands of years, although it got its physical interpretation only in the last century.

In this chapter we first will describe the experimental technique we developed for our investigations and the physical language of optical and electrodynamical parameters, needed for this description. In Section 3.1 we will briefly introduce the basics of microwave electrodynamics and consider the Hagen-Rubens limiting regime, which is of great importance for the analysis employed in our experimental methods, which we describe in details in Section 3.2. Section 3.3 is devoted to the analysis of the experimental data. Finally, the electrochemical crystal grow procedure is described in Section 3.4.

3.1   Theoretical Background

The electrodynamic response of any system is characterized by two quantities, often combined to a complex parameter, basically describing the amplitude and the phase of the response. This might be the complex conductivity, the refractive index or the surface impedance. At low frequencies, up through the radio frequencies (RF), these quantities are usually experimentally accessible, and hence both the real and imaginary parts of the complex conductivity $\hat{\sigma} = \sigma_1 + i\sigma_2$ can be directly determined. On the other hand, at higher frequencies only one experimental parameter is usually directly accessible (surface resistance R_S in the micro and millimeter spectral range and the reflectivity R in the optical spectral range). In order to combine the micro and the millimeter wave data with the optical results, we have to consider the relationships between different optical parameters.

3.1.1   Basic Electrodynamics

When we study highly conducting materials at microwave frequencies, the physical quantity we usually measure is the complex surface impedance $\hat{Z}_S = R_S + iX_S$, where R_S is the surface resistance and X_S is the surface reactance. The surface impedance is defined [93] as the ratio of the electric and magnetic field at the surface of the metal $\hat{Z}_S = \mathbf{E}_\parallel / \mathbf{H}_\parallel$, where the subscripts indicate the field component parallel to the

plane of the surface. The surface impedance, put by this definition, is a dimensionless quantity, which is independent of the surface geometry. Usually it is normalized by the impedance of the vacuum $Z_0 = 4\pi/c_0 = 377\ \Omega$ [49], and the definition becomes

$$\hat{Z}_S = \frac{4\pi}{c_0} \cdot \frac{\mathbf{E}_\parallel}{\mathbf{H}_\parallel} \tag{3.1}$$

The impedance is a response function which determines the relationship between the electric and the magnetic fields in a medium, it can be shown [2.16], that for a non-magnetic conductor ($\mu_1 = 1$)

$$\hat{Z}_S = \frac{4\pi}{c_0} \cdot \frac{1}{\sqrt{\hat{\varepsilon}}} = \frac{4\pi}{c_0} \cdot \frac{1}{\hat{N}} = \frac{Z_0}{\hat{N}} \tag{3.2}$$

where

$$\hat{N} = n + ik = \sqrt{\hat{\varepsilon}} \tag{3.3}$$

is the complex refractive index, $\hat{\varepsilon} = \varepsilon_1 + i\varepsilon_2 = \varepsilon_1 + \frac{4\pi i}{\omega}\sigma_1$ is the complex dielectric constant.

Although the surface impedance is mainly used in characterization of high-frequency properties of conductors, its idea is also useful if the thickness of the medium is much larger than the skin depth.

At high frequency $f = \omega/2\pi$, the electrical field penetrates into the matter on a length scale, $1/\text{Im}(\hat{k})$, where $\hat{k}$ is the wavevector inside the material [49]; this length in general is either the skin depth in the normal state or the penetration depth in the superconducting state. It is assumed that the sample surface is flat at the scale of the penetration length.

Typically for the most of good conducting materials, the low-frequency approximation, known as the Hagen-Rubens limit ($\omega\tau \ll 1$), is valid [49]. For a good metal in the Hagen-Rubens limit $\sigma_1 \approx \sigma_{DC} \gg \sigma_2$, and $1/\text{Im}(\hat{k})$ becomes the classical skin-depth, which depends on the DC-conductivity σ_{DC}:

$$\delta = \frac{c_0}{\sqrt{2\pi\omega\sigma_1}} = \frac{c_0}{\sqrt{2\pi\omega\sigma_{DC}}} \tag{3.4}$$

If we assume that $|\varepsilon_1| \gg 1$, which is certainly true for the case of good metals at microwave frequencies but may also be fulfilled for dielectrics, we obtain from Eq. (3.2) the well known relation for the surface impedance [49]:

$$\hat{Z}_S \approx \left(\frac{4\pi\omega}{i \cdot c_0^2 \left(\sigma_1 + i\sigma_2 \right)} \right)^{1/2} ; \tag{3.5}$$

the expression for the real and imaginary parts, R_S and X_S, are then

$$R_S = \left(\frac{2\pi\omega}{c_0^2} \right)^{1/2} \left[\frac{\left(\sigma_1^2 + \sigma_2^2 \right)^{1/2} - \sigma_2}{\sigma_1^2 + \sigma_2^2} \right]^{1/2} , \tag{3.6}$$

$$X_S = - \left(\frac{2\pi\omega}{c_0^2} \right)^{1/2} \left[\frac{\left(\sigma_1^2 + \sigma_2^2 \right)^{1/2} + \sigma_2}{\sigma_1^2 + \sigma_2^2} \right]^{1/2} . \tag{3.7}$$

In the Hagen-Rubens limit, for highly conducting materials at microwave frequencies $\varepsilon_2 \gg |\varepsilon_1|$ or $\sigma_1 \approx \sigma_{DC} \gg |\sigma_2|$, we find that the components of the surface impedance are equal:

$$R_S\left(\omega\right) = -X_S\left(\omega\right) = \left(\frac{2\pi\omega}{c_0^2 \sigma_1} \right)^{1/2} = \frac{1}{\delta\left(\omega\right)\sigma_1} \tag{3.8}$$

and display a characteristic $\omega^{1/2}$ dependence on the frequency.

Eq. (3.8) means that the surface resistance and (the absolute value of) the surface reactance are equal in the case of a metal. In cases where both the surface resistance and the surface reactance are measured, we can calculate the complex conductivity $\hat{\sigma} = \sigma_1 + i\sigma_2$ by inverting these expressions:

$$\sigma_1 = -\frac{8\pi\omega}{c_0^2} \frac{R_S X_S}{\left(R_s^2 + X_s^2 \right)^2}, \tag{3.9}$$

$$\sigma_2 = \frac{4\pi\omega}{c_0^2} \frac{X_s^2 - R_s^2}{\left(R_s^2 + X_s^2 \right)^2}. \tag{3.10}$$

The complex refractive index $\hat{N}$ is related to the reflectivity R at the normal incidence by [49]:

$$R\left(\omega\right) = \left|\frac{1 - \hat{N}}{1 + \hat{N}}\right|^2 = \frac{[1 - n]^2 + k^2}{[1 + n]^2 + k^2} \tag{3.11}$$

at the interface air-material. The relationship between R_S, X_S and $R(\omega)$ can be calculated from Eqs. (3.2) and (3.11), giving

$$R\left(\omega\right) = 1 - \frac{4R_S}{Z_0}\left(1 + \frac{2R_S}{Z_0} + \frac{R_S^2 + X_S^2}{Z_0^2}\right)^{-1}. \tag{3.12}$$

In the limit $R_S, X_S \ll Z_0$, the higher order terms in Eq. (3.12) can be neglected, yielding

$$A\left(\omega\right) = 1 - R(\omega) = \frac{4R_S}{Z_0}. \tag{3.13}$$

Thus, at this limit, the absorptivity $A(\omega)$ is directly proportional only to R_S. As Z_0 is very large compared with the values of the surface impedance measured in our experiments (a typical order of magnitude for the samples we have investigated is 1 Ω; for a good metal as copper it is equal to 30 mΩ at the temperature of 4.2 K and frequencies of 10^{11} GHz), this limit is appropriate for the most of the situations we intended to examine.

3.2 Experimental Techniques

3.2.1 Cavities

In order to perform microwave absorption measurements at K (18–26.5 GHz), Ka (26.5–40 GHz), and V (50–75 GHz) frequency bands, we have designed three enclosed resonators (cavities) with center frequencies of 24 GHz, 33.5 GHz, and 60 GHz, respectively. Being manufactured from a copper block, the cylindrical TE_{011} cavities are operated in a transmission configuration; the microwave power is led into the cavity through the inlet waveguide, and the detector is mounted at the end of the outlet waveguide. All cavities are constructed in three pieces: two flat endplates mechanically attached by screws to the middle cylindrical barrel, which provide the pressure

for reproducibly clamping the cavity assembly tightly together (see Fig. 3.4). The cavity may be taken apart or disconnected from the waveguides in a matter of minutes providing an easy sample insertion/removal. Nevertheless, since the resonance frequency of a cavity is extremely sensitive to the volume of the cavity, after any disassembling and further assembling of the resonator we suffer an inevitable shift of the central frequency of about ± 1 MHz. However, this irreproducible frequency offset can be taken into account and can be eliminated from the consequent analysis, and we will come back to this problem in Section 3.3.

The resonance frequency of a cavity is determined by the length h and the inner diameter d of the cylindrical barrel. In fact, for one particular mode there is only one parameter, either the diameter d or the height h, which can be arbitrarily chosen to obtain the best performance of the resonator, namely, high quality factor Q. In the beginning, we have selected the diameter d to height h ratio equal to $3/2$. This value of d/h gives small density of modes near the desired resonance frequency together with a good value of the quality factor Q, which is maximal for $d/h = 1$ for any TE$_{mnp}$ =TE$_{0np}$ mode [94]. Here the subscripts m, n, and p refer to the number of half-cycle variations in the angular (ϕ), the radial (r), and the longitudinal (z) direction, respectively.

The dependence of the frequency f on the diameter d and the height h of a cylindrical cavity in the vacuum (or air) is presented by [95]:

$$(df)^2 = \left(\frac{c \, (k_c a)'_{mn}}{\pi} \right)^2 + \left(\frac{c_0 p}{2} \right)^2 \left(\frac{d}{h} \right)^2 \tag{3.14}$$

where $c_0 = 1/(\mu_0 \varepsilon_0)^{1/2}$ is the velocity of light in the vacuum, and $(k_c a)'_{mn}$ is a nth root of the mth-order Bessel function $J'_m(k_c a)$. By substituting numerical values TE$_{mnp}$ = TE$_{011}$, $(k_c a)'_{mn} = 3.832$, $d/h = 3/2$, and $c = 2.998 \times 10^{10}$ cm/s, we get:

$$d \, [\text{cm}] = \frac{4.29 \times 10^{10} \, [\text{cm/s}]}{f \, [\text{Hz}]}, \quad h \, [\text{cm}] = \frac{2.86 \times 10^{10} \, [\text{cm/s}]}{f \, [\text{Hz}]}.$$

The Table 3.1 summaries the so-calculated sizes of resonators for appropriate frequencies.

f	Q [†]	d	h	V_c
(GHz)	at 300 K	(mm)	(mm)	(mm^3)
24	12500	17.9	11.9	2994
33.5	11000	12.8	8.6	1100
60	7000	7.1	4.8	190

Table 3.1: Resonant frequency f, the measured quality factor Q, diameter d, height h, and volume V_c for each of our cavities. Notice the ratio $d/h \approx 3/2$ for each cavity. [†] dependent on the quality of cavity interior surface

In order to minimize Ohmic losses in the cavity walls and, therefore, to maximize the resonator's quality factor Q, all interior walls of the cavities were polished after fabrication up to perfect mirror surface condition.

3.2.2   Modes Excited

We have chosen the working mode of the resonators to be TE$_{011}$ for the following reasons. First, the quality factor Q is roughly proportional to the volume divided by the surface area because the stored energy depends on the volume while the losses occur only at the walls. An exceptional case is the TE$_{01p}$ mode. For this mode the side-wall losses decrease continuously with increasing frequency, and it may be used to obtain a very high Q, so that the resonances are sharp. Second, in the TE$_{011}$ mode only the circumferential currents flow, thus the field distribution and the quality factor Q are independent of the contact between the middle cylindrical part and removable endplates of the cavity. In fact, there is no electric current flow in either the radial (r) or the longitudinal (z) direction, but only in angular (ϕ) direction (Figs. 3.1, 3.2). This allows us to open the cavity for introducing the sample without a posterior degradation of the Q value.

In general, for a perfectly cylindrical cavity, the TE$_{01p}$ modes are degenerate with the TM$_{11p}$ modes. This problem can be easily avoided by small modification of shape of the cavity, since the TM$_{11p}$ modes have electrical currents flow on the walls of
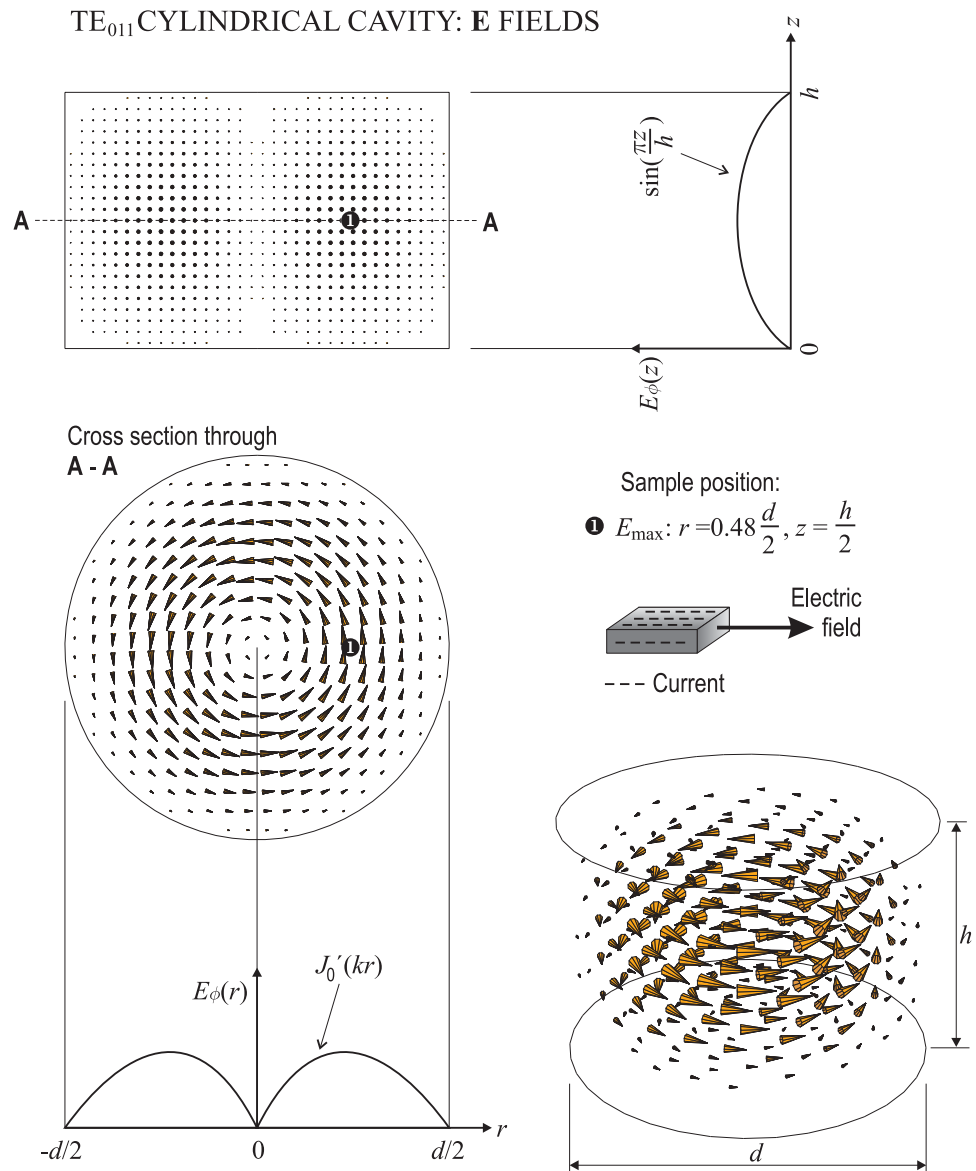
Figure 3.1: Electric field lines inside a cylindrical cavity resonating in the TE_{011} mode. The position of the maximal electric field E_{max}, position 1, is indicated on the figure. The field distribution was calculated numerically using the commercially available program MAFIA [103].
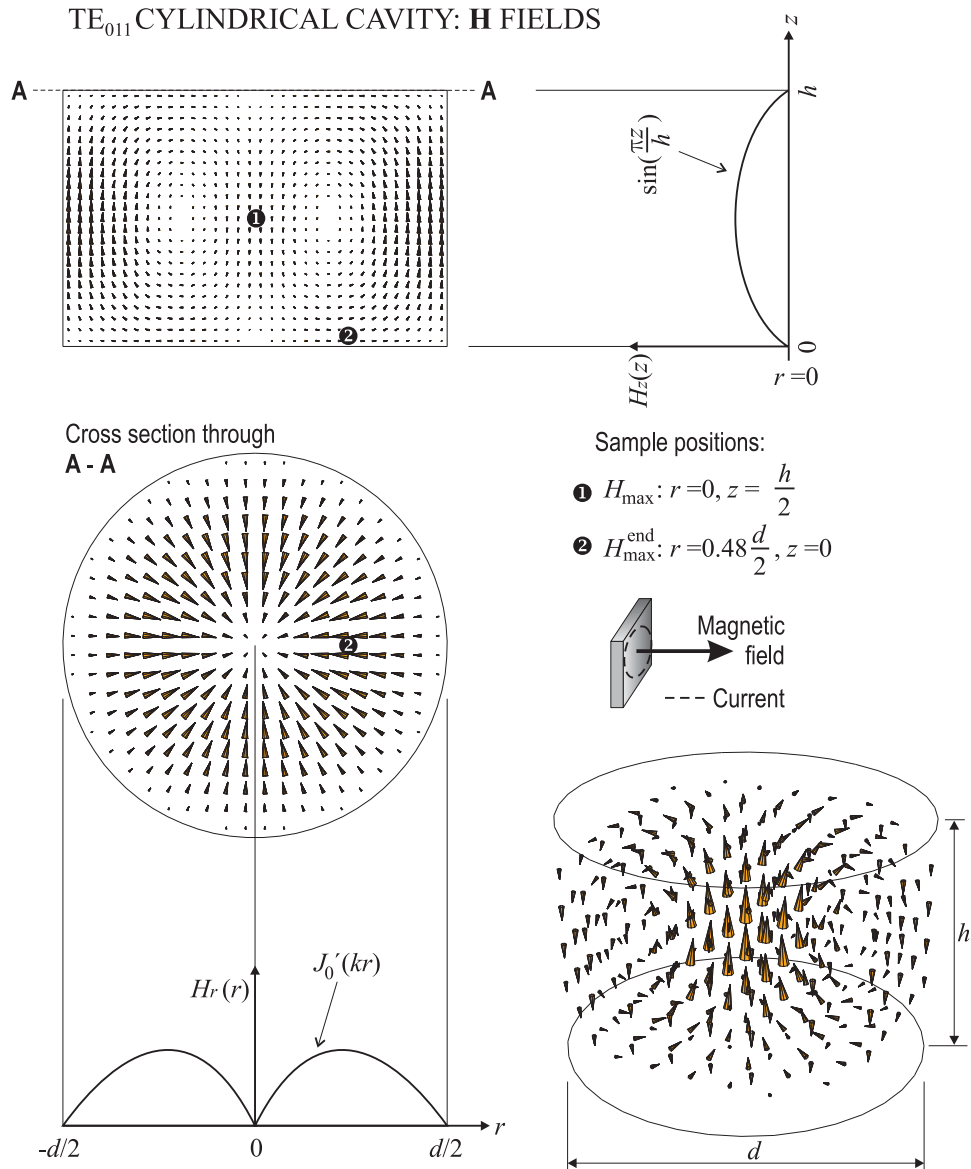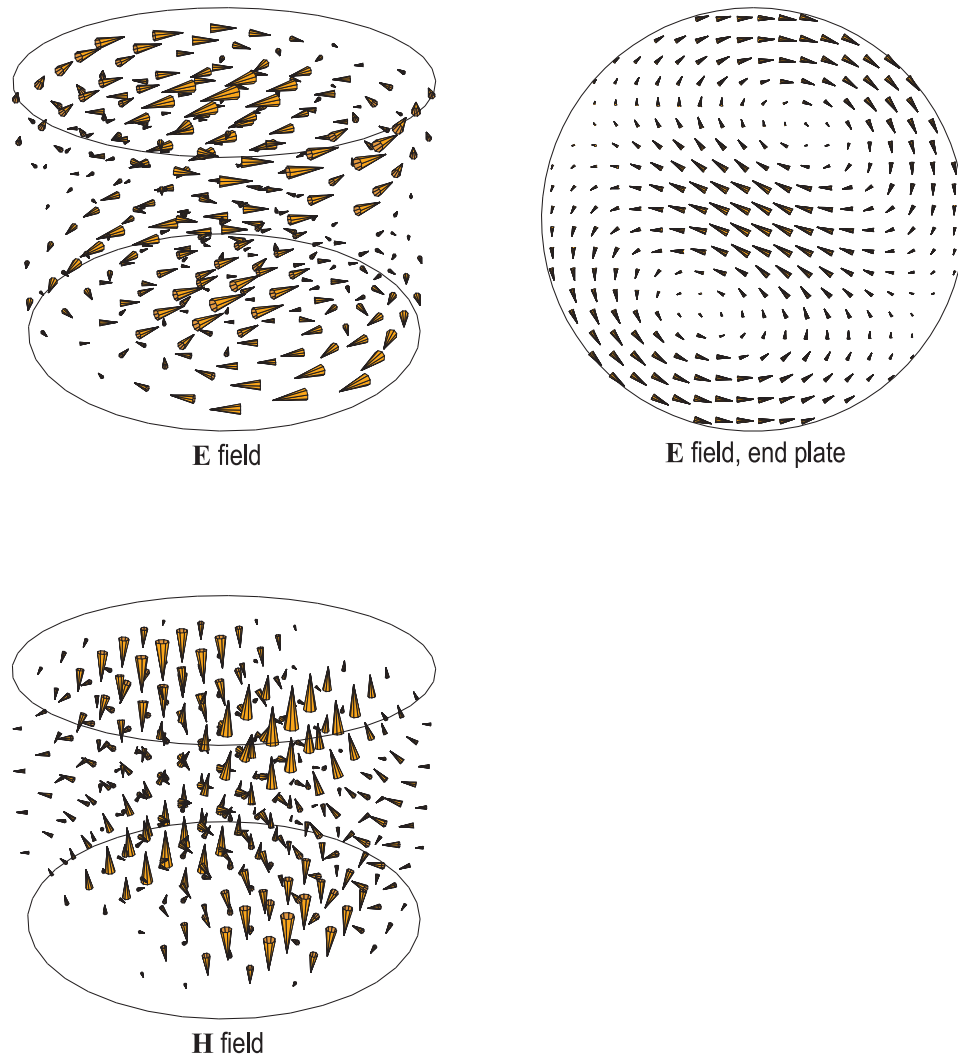
Figure 3.2: Magnetic field lines inside a cylindrical cavity resonating in the TE_{011} mode. Both H_{max}, the maximal magnetic field in the cavity, position 1, and H_{max}^{end}, the maximal magnetic field on the endplate, position 2, are indicated on the figure. The field distribution was calculated numerically using the commercially available program MAFIA [103].

TM$_{111}$ MODE: **E** and **H** FIELDS

E field

E field, end plate

H field

Figure 3.3: Electric and magnetic field lines inside a cylindrical cavity resonating in the TM$_{111}$ mode. Note that the electric field has its antinode on the endplate. The field distribution was calculated numerically using the commercially available program MAFIA [103].

the cavity. To discriminate against the TM_{111} mode, we made small grooves at both the top and the bottom ages of the barrel part (see Fig. 3.4). These grooves are at the position of an antinode in the TM_{111} mode and of a node of the TE_{011} mode(see Fig. 3.3). Consequently, the TM_{111} mode shifts to lower frequencies by some hundreds MHz. It gets also weaker and has lower Q-values than that for the TE_{011} mode. This was experimentally checked for 24 GHz and 33.5 GHz cavities by using a broad-band microwave spectrum analyzer.

The hole for the sample positioning as well as the coupling apertures also affect only the center frequency and the Q factor of the TM_{111} mode rather a that of the TE_{011} mode.

3.2.3   Coupling

Coupling between the waveguides and the cavity is achieved by means of small circular holes in the cavity wall. For the cylindrical TE_{011} mode the electric field is zero at all surfaces, so the coupling must be magnetic. Actually, possible are only two good ways of magnetic coupling of the TE_{011} cylindrical cavity resonator to the rectangular waveguide operating in TE_{10} mode. They correspond to the two magnetic field maximum belts in the cavity: the first, "equatorial" belt lies at $h/2$ position of the barrel part, the second is located on the surface of each end plate at distances $0.24d$ from the center of the plate (see Fig. 3.2). Obviously, the hybrid use of these two magnetic field maximum belts provides a third possible configuration of the coupling. Since we wanted to use an upper end plate for the sample positioning, we have chosen the lateral coupling configuration. The two antipodal coupling holes were made on opposite sides in the side wall of the cylindrical part of the cavity at half of its height, where the magnetic field of the TE_{011} mode has its antinodes (Fig. 3.2). These holes coincide with the holes in the narrow faces of the rectangular waveguides operating in TE_{10} mode. The only field existing at the narrow edge of a waveguide carrying the dominant mode is a longitudinal magnetic field. Through the two coupling holes this field is transmitted into the cavity with opposite phases for the two holes, and

so it matches the TE_{011} mode, but not the other possible TE-modes. The attached waveguides were terminated at distances of $3/4\lambda_g$ from the holes by pieces of metal soldered to butt-ends. Here λ_g is a wavelength of the electromagnetic (EM) radiation in a waveguide defined by formula [96]:

$$\lambda_g = \frac{\lambda_0}{\sqrt{1 - \left(\frac{\lambda_0}{\lambda_c}\right)^2}}, \tag{3.15}$$

where $\lambda_0 = c/f$ is the wavelength of EM-radiation in the free space without walls, λ_c is a cutoff wavelength, which equals $\lambda_c = 2a$ in the case of a rectangular waveguide with cross section dimensions $a < b$ [96]. From the geometrical consideration (see Fig. 3.4) it is obvious that the length between the coupling hole and the shorted end of the waveguide should be any odd multiple of $1/4\lambda_g$.

We can control the degree of coupling between the waveguides and the cavity by means of the diameter and the thickness of the coupling apertures: the bigger the ratio of the diameter to the thickness, the stronger the coupling. Nevertheless, the diameter of the coupling hole cannot be too large: Bethe [97] has shown that the linear dimensions of the aperture must be less than $\lambda_g/2\pi$, so that the electrical and the magnetic fields in its neighborhood are closely approximated by unperturbed fields. There is a crucial trade off between the strong coupling, which assures a good signal-to-noise ratio, and weak the coupling, which decreases radiation losses from the cavity, resulting in a higher Q-factor and an increased sensitivity. We have found experimentally that the optimal coupling apertures should be small, with a diameter of $\lambda_0/5 - \lambda_0/4$, where λ_0 is the wavelength corresponding to the working frequency. For the cavities working at frequencies 24, 33.5, and 60 GHz we used the coupling holes with diameters 3, 2, and 1 mm, respectively. The diameter to thickness ratio for a coupling aperture was always kept larger than $3/2$. Therefore we used undercoupled cavities with a coupling of about 10%, which provides a good compromise between a good dynamic range and a high sensitivity.
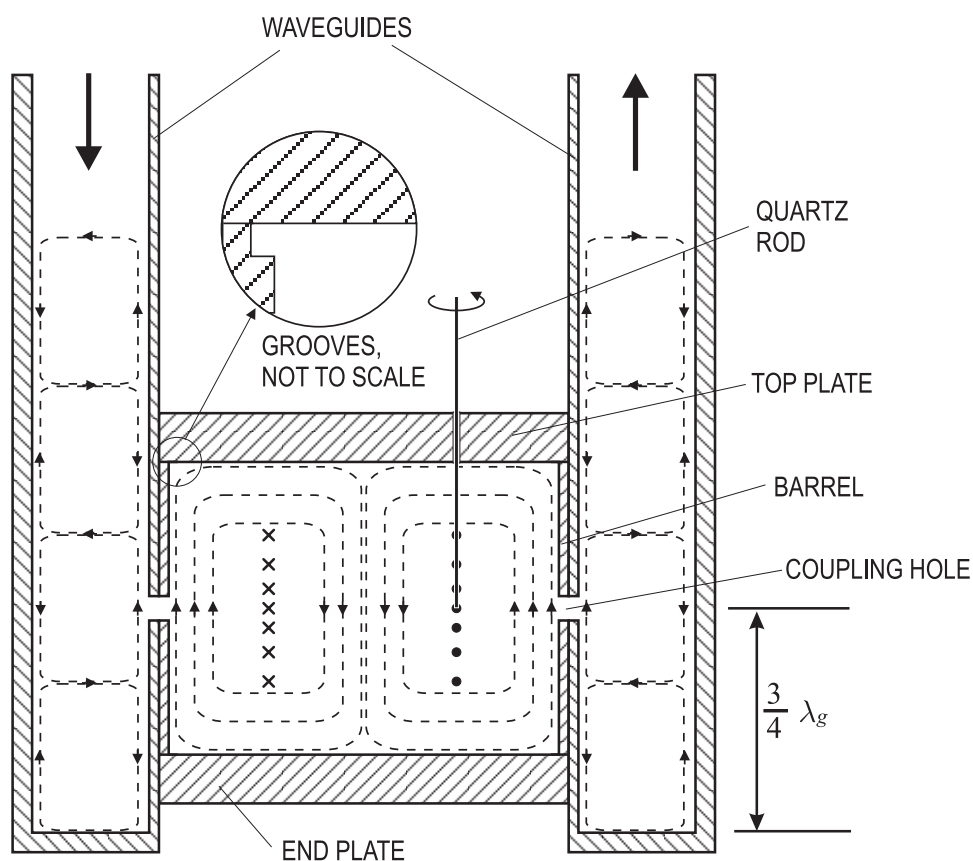
Figure 3.4: Schematic view of the TE_{011} cavity coupled via magnetic field (dashed lines). The grooves in the barrel wall edges serve to shift the TM_{111} mode to lower frequency. For the distance of the coupling holes to the shorted ends we have chosen $3/4\lambda_g$, where λ_g the wavelength of the guided wave.

3.2.4 Sample Positioning, and Sample Rotation

Typically, the perturbation is realized by either placing a small piece of the material of interest into the cavity (enclosed configuration) or by replacing one of the walls of the cavity with the material (endplate configuration). For studies of quasi-one-dimensional conductors, which usually grow as tiny needle-like crystals, the endplate configuration cannot be applied because of geometrical/size reasons. Moreover, as it was discussed above, the current in the endplate of a cylinder cavity operating in the TE_{011} mode flows circularly. This implies that the endplate configuration is useful only for materials which are plane-isotropic, i.e., for a two-dimensional sample. We have developed the enclosed configuration technique which does not preclude the study of anisotropic conductors [98, 100].

From the field patterns of the TE_{011} mode described above it turns out that there are two possibilities of performing the microwave absorption measurements either in the electric or in the magnetic field antinodes. If the sample is placed in the magnetic field antinode, then the circular eddy currents are excited in the plane perpendicular to the magnetic field, thus one cannot use this configuration for probing the one-dimensional samples along a desired direction. The placing of the sample in the electric field antinode is preferred for measurements of low-dimensional systems. In this case the excited currents are co-directed with an electric field vector giving the possibility to measure along one particular direction, as shown in the Figure 3.1.

In order to make measurements of samples placed in the electric field antinode (cylindrical coordinates $[0.24d; \phi; h/2]$), we drilled a small hole of a 0.2 mm diameter in the top plate at a distance $0.24d$ from its center. The samples were mounted atop of a quartz rod of diameter 0.15 mm, which was run through this hole. Typically, we used the central purely quartz part of an optical fiber cut exactly perpendicular to the axis. The length of the quartz rod was chosen in a way that the sample position was exactly $h/2$ inside the cavity resonator. The quartz fiber was connected to a specially constructed rotation mechanism, which allowed rotating the sample inside the cavity without taking it out (*insitu* rotation). For setting on the rotation of the
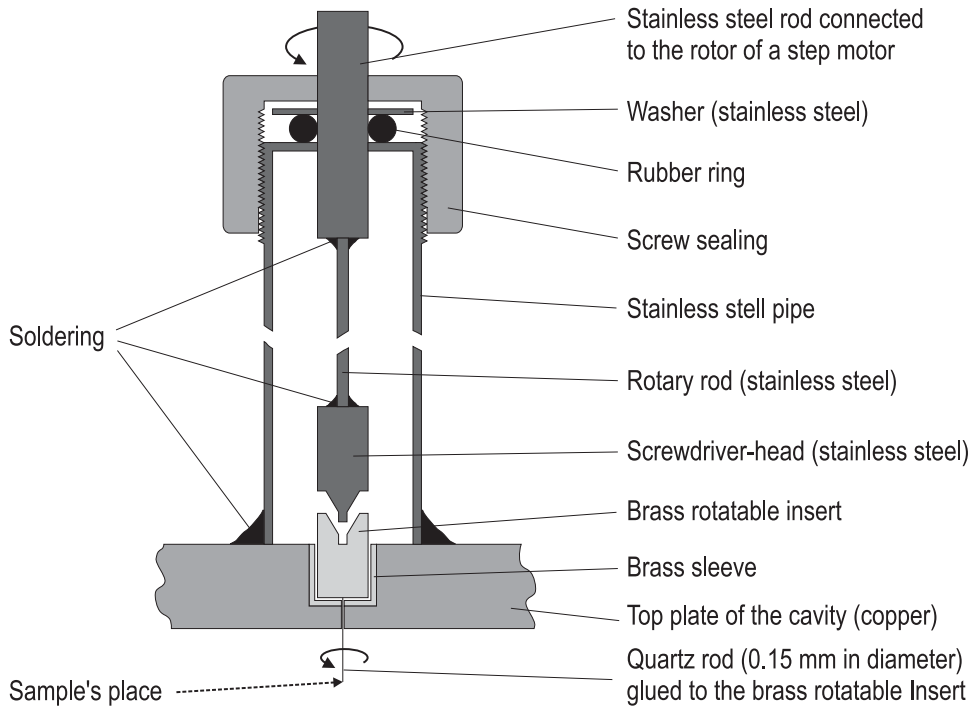
Figure 3.5: Schematic view of the rotation mechanism we utilized in our experiments.

sample we used a PC-controlled stepper motor. The whole construction is depicted in Fig. 3.5 This technique provided us with an angular positioning accuracy of better than 1 degree. The typical angular scans of center frequency and halfwidth of a sample rotating inside the cavity are shown in Fig. 3.6.

We found that the quartz fiber does not change the cavity Q-factor, but introduces a slight temperature-independent shift of the center frequency of a resonance. This shift can, however, be excluded from the analysis by making both an unperturbed (reference) and a perturbed (with a sample) measurements in the presence of the same quartz rod.

3.2.5   Experimental Scheme and Devices

A schematic diagram of the setup is shown in Figure 3.7. We utilized in our measurements a common width technique [100, 102] by making a broad sweep of the source
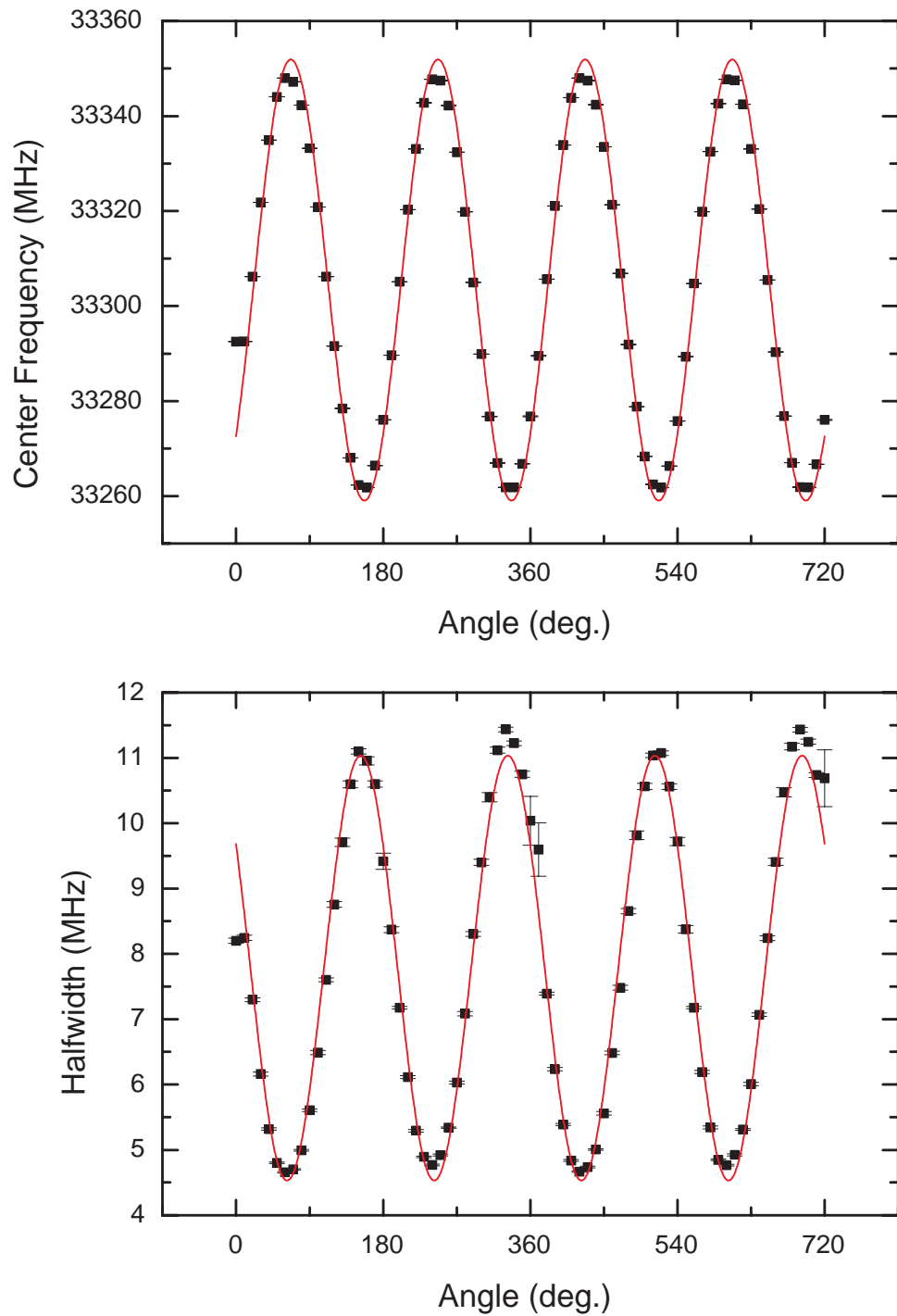
Figure 3.6: Typical angular scans of center frequency (top) and halfwidth (bottom) of a sample rotating in the cavity. Solid symbols are measured points, the curve is a fit with $\cos^2$ function. The minima of the center frequency and maxima of the halfwidth correspond to situation when the sample is aligned parallel to the local electric field.
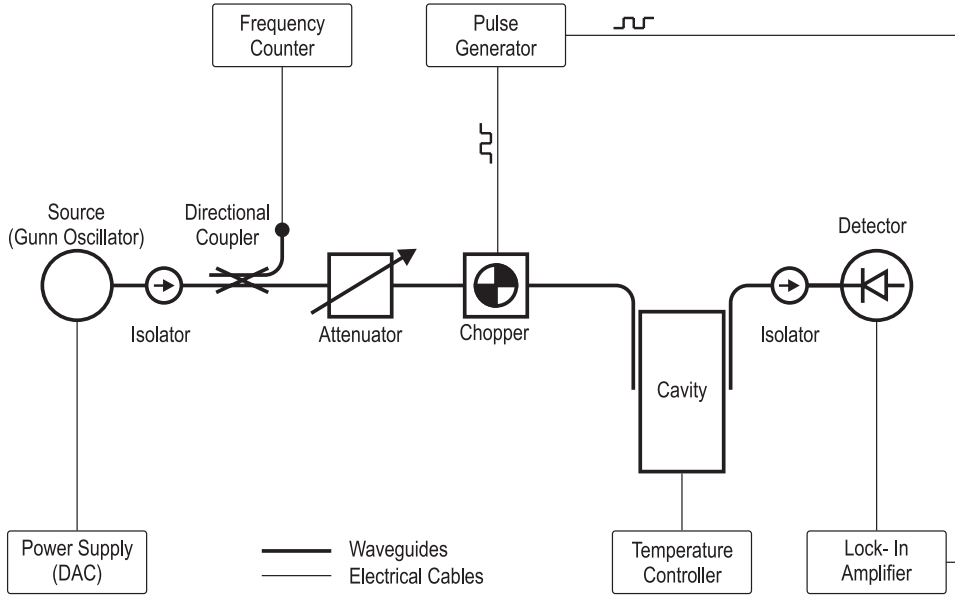
Figure 3.7: Schematic view of the experimental setup for the width measurement configuration.

frequency over a range of several times the resonance width Γ. The amplified detected signal is averaged (typically 50 times) before fitting with a Lorentzian, which directly gives the center frequency f_0, halfwidth Γ, and quality factor $Q = f_0/\Gamma$. A perfect Lorentzian fit, which has three parameters, requires at least three points, though we found that the best results can be obtained with a scan of approximately 5–7 times the halfwidth of the resonance curve containing 150–200 experimental points.

The experiments are performed by using a varactor-tuned Gunn sweep oscillators with an essentially flat power output of about 100 mW (14 dBm) and a frequency bandwidth of 1 GHz around the center frequencies of 24 GHz, 33.5 GHz, and 60 GHz for K, Ka, and V bands, respectively. These voltage-controlled sources are tuned by high – stability 16-bit digital-to-analog controller (DAC) made in the electronic shop of Physics Department. The DAC has either a grounded or a float output in the range of ± 15 V (max. current 5 mA) with a resolution of 458 μV/step. In order to prevent the microwave source from reflected waves, we used a ferrite isolator attached to the oscillator. Then the microwave power goes though a 20 dB directional coupler, the

reference arm of which is connected to the "EIP 598A" microwave frequency counter capable of reading frequencies up to 170 GHz. A calibrated attenuator is utilized to tune the microwave power and finally is fixed to some value preventing the sample from heating with the microwave radiation. The radiation is chopped by a modulator controlled by a commercial function generator, at the frequency around 3 kHz . After passing through the cavity, the transmitted microwaves pass through another ferrite isolator and finally reach a diode detector. Since the typical detected signal is some millivolts, we used a 40 dB low noise preamplifier connected directly to the detector, before transmitting the signal through the lengthy coaxial cable to the "EG&G 5210" lock-in amplifier. The lock-in amplifier is synchronized with the chopper by using the signal of the same reference frequency from the function generator.

All used devices are connected to a PC via IEEE-488 bus interface, and the experiment is completely controlled by a homemade computer program.

3.2.6 ^{4}He Cryogenic System

In order to perform measurements at low temperatures, the following cryogenic system was constructed. The heart of the system is a glass ^{4}He bath cryostat (Fig. 3.8a) with an internal metallic cryostat inserted. The glass cryostat consists – from outside to inside – of following volumes: the outer vacuum shield volume with an unrestorable vacuum quality, the liquid nitrogen (LN_2) bath, the intermediate vacuum volume, and the liquid helium (LHe) bath. The double-wall metallic cryostat is made of two light-wall stainless steel tubes inserted one into another. This construction provides two additional volumes: the intermediate vacuum jacket between the tubes, and the sample volume, usually filled with a small quantity of He exchange gas. A Mylar window atop each copper waveguide is used to ensure a vacuum-tight environment of the sample volume.

The LHe bath volume, the intermediate vacuum volume of the metallic insert and the sample volume are separately connected to the helium main and pumping stand, formed by a concatenated booster and rotary pumps. The system of valves permits
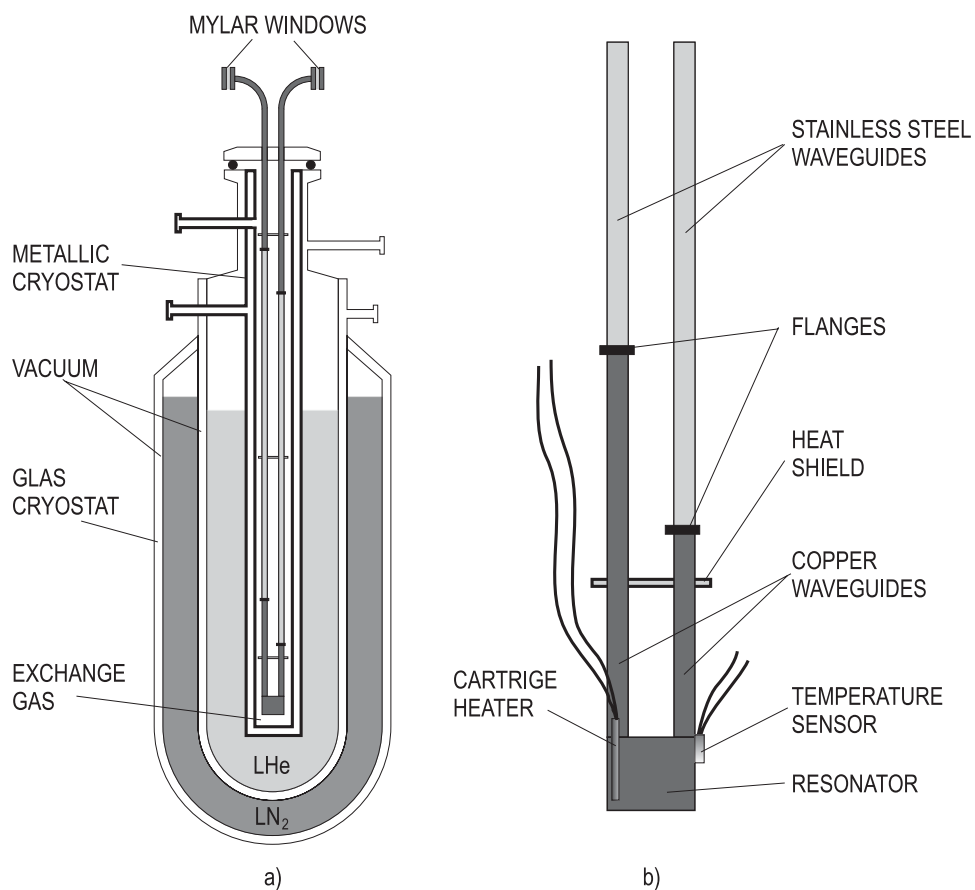
Figure 3.8: Schematic view of the ^{4}He cryostat with a cavity inserted (a). Schematic view of the resonator with attached waveguides and temperature regulation elements (b).

to inflate with gaseous helium or to evacuate any of these volumes independently. This allows, varying the intermediate vacuum and exchange gas density, to control the heat exchange and therefore tune the cooling rate inside the sample volume from 0.1 K per minute to several Kelvin degrees per minute.

In order to cool from the room temperature down to 80 K, we fill the cryostat only with liquid nitrogen, make rough intermediate vacuum of 0.1 mbar and put some exchange gas into the LHe bath and the sample volume, usually about 5 mbar, which provides a weak thermal link to the He bath. To cool further down we put some cold helium gas from a helium transportation dewar, reaching the temperature of about 20 K. Subsequent temperature lowering down to 4.2 K is achieved by filling the LHe volume with liquid helium.

The measurements below 4.2 K are performed by pumping on liquid helium in the LHe bath. By doing this, the lowest temperature of 1.8 K can be achieved. The measurements on warming were done using either a natural warming of the cryostat or combining that with an additional heating of the cavity. The natural warming of the cryostat from 4.2 K to the room temperature usually takes about 50 hours with minimal cooling rate of 0.1 K per minute. In order to increase or vary the warming rate, the built-in heater can be used, power load of which is regulated by a "Lake Shore DRC-91C" temperature controller.

3.2.7 Temperature Regulation and Stability

The three-term (PID) "Lake Shore DRC-91C" temperature controller provides real-time adjustment and control of the temperature setpoint, gain (proportional), reset (integral), and rate (derivative). Having determined the proper PID coefficients, we can achieve the temperature stability of better than 10 mK. An analog heater output with four decade steps of a maximum output power from 25 mW to 25 W is connected to a "Watlow" 20 W cartridge heater, embedded in the side wall of the cavity (see Fig. 3.8b). The temperature controller is supplied with IEEE-488 standard remote interface.

Temperature sensing over the range from 1.4 K to 325 K is realized by a "Lake Shore DT-470" silicon diodes, which follow a standard voltage-temperature response Curve # 10 from Lake Shore. The temperature sensor is mounted atop the cavity housing opposite to the heater.

In order to prevent the sample from heating by the microwave radiation, we used a series of test measurements of a reference sample and changed the attenuation of the microwaves, to ensure that the power applied did not affect the results of the measurements. The small amount of the He exchange gas inside the cavity is also promotes that the cavity and the sample are at the same temperature.

3.3   Data Analysis

The theory of an analysis required to determine the sample properties when inserted inside a cavity is highly developed [99, 100, 101]. In this case one simply takes the difference of the measured quality factor Q (or a halfwidth of the resonant curve $\Gamma = f_0/Q$) and center frequency $f_0 = \omega_0/2\pi$ with the sample in and out. However, the relative changes of quality factor $\left(\Delta\frac{1}{2Q}\right)$ and center frequency $\left(\frac{\Delta\omega}{\omega_0}\right)$ upon introducing the sample are connected to the complex conductivity in a nontrivial way, depending on the sample "electrodynamical" geometry. Namely, the sample can either be a good conductor and microwaves penetrate only in the length scale of skin depth into it, or it can be a bad conductor (or even a dielectric) and microwave radiation penetrates completely through it, since the skin depth exceeds the principal dimensions of a sample. The former situation is called "skin depth regime", the latter is called "depolarization regime". Since it is the conductivity, which defines the skin depth value (see Eq. (3.4)) at a certain frequency, it turns out that to be useful to know the conducting properties of a sample *a priori*, at least roughly. Nevertheless, a self-consistent analysis can be performed even for a sample of unknown conductivity; and we will discuss it below.

3.3.1 Skin Depth Regime

If the sample is in the skin depth regime, then both, the surface resistance R_S and the surface reactance X_S can be calculated directly from the change of the halfwidth of the resonance ($\Delta\Gamma$) and the center frequency (Δf), divided by the center frequency (f_0) of the unperturbed cavity [99, 100, 101]:

$$\xi R_S = \frac{\Delta\Gamma}{2f_0}, \tag{3.16}$$

$$\xi X_S = \frac{\Delta f}{f_0} - C, \tag{3.17}$$

where C is a constant frequency shift which is introduced when the cavity is disassembled in order to mount the sample (Sec. 3.2.1), and ξ is a calculable resonator constant depending on cavity sizes, operating mode at given frequency $\omega = 2\pi f_0$, as well as on the sample's shape and size [99]:

$$\xi = \frac{-i\gamma}{n^2} \frac{\omega a}{2c_0} \cdot \Theta, \tag{3.18}$$

where γ is a constant that depends only on the filling factor and the resonant mode of a cavity of a given shape; n is a depolarization factor, depending on the shape of the sample; a is a principal sample's size; c_0 is the speed of light. The parameter Θ describes the deviation of the sample's shape from the spherical one and its values for the two typical configurations, a prolate and an oblate spheroid, are summarized in Table 3.2.

In our experiments we have employed cylindrical cavities operating in the TE_{011} mode, having the ratio of the diameter to the height equal to 3/2 and we were putting the samples in the electric field antinode, at the half height of the cavity (see. Sec. 3.2.4). In this experimental configuration the sample's constant γ is defined by the following equation [99]:

$$\gamma = 2.03 \frac{V_S}{V_C}, \tag{3.19}$$

where V_S and V_C is the volume of the sample and of the cavity, respectively. Both of them are measurable quantities.

	Prolate Spheroid, Θ	Oblate Spheroid, Θ
Field $\parallel \hat{z}$	$(3^2\pi/2^5)b/a$	$(3/2^3)a/b$
Field $\perp \hat{z}$	$(3\pi^3/2^6)b/a$	$(3^2/2^3)b/a\ln a/b$

Table 3.2: Parameter Θ for different orientations of either a prolate or an oblate spheroid, in the electric field antinode, where $2a \gg 2b$ are the sample dimensions; $\hat{z}$ is the direction of the spheroid symmetry axis and the electric field is either parallel or perpendicular to this symmetry axis.

The value of the depolarization factor, n, is fully determined just by the shape of the sample and can be exactly calculated for any rotationally symmetric body, like a spheroid or a disk. This means that we have to model our sample with one of the following bodies [99]:

- A sphere $(a = b = c)$: $n_x = n_y = n_z = 1/3$.

- A cylinder in the x-direction $(a \to \infty, b = c)$: $n_x = 0, n_y = n_z = 1/2$.

- A flat plate $(a, b \to \infty)$: $n_x = n_y = 0, n_z = 1$.

- A prolate spheroid $(a > b = c)$ of eccentricity $\varepsilon = \sqrt{1 - (b/a)^2}$

$$n_x = \frac{1 - \varepsilon^2}{2\varepsilon^3}\left(\ln\frac{1+\varepsilon}{1-\varepsilon} - 2\right), n_y = n_x = \frac{1}{2}(1 - n_x). \tag{3.20}$$

- An oblate spheroid $(a = b > c)$ with $\varepsilon = \sqrt{(a/c)^2 - 1}$

$$n_z = \frac{1 + \varepsilon^2}{\varepsilon^3}\left(\varepsilon - \arctan\varepsilon\right), n_x = n_y = \frac{1}{2}(1 - n_z). \tag{3.21}$$

- A prolate ellipsoid $(a \gg b \geq c)$

$$n_x = \frac{bc}{a^2}\left(\ln\frac{4a}{b+c} - 1\right). \tag{3.22}$$

Here a, b, and c are the sample dimensions and n_x, n_y, n_z are the depolarization factors $(n_x + n_y + n_z = 1)$ along the x, y, and z directions, respectively. All of our samples had a needle-like geometry and therefore were modelled either by a prolate spheroid or prolate ellipsoid, using Eqs. (3.20) and (3.22).

Hence, as a consequence of the analysis described above, for the most common configuration of our investigations, a sample of a needle-like shape with dimensions $a \gg b \geq c$ placed in the electric field antinode of a cylindrical cavity operating at TE_{011}, the constant ξ would result in:

$$|\xi| = 2.03 \frac{V_S}{V_C} \cdot \frac{3^2 \pi \omega}{2^6 c_0} \cdot \frac{a^4}{bc^2 \left(\ln \frac{4a}{b+c} - 1 \right)^2} \tag{3.23}$$

in terms of notations introduced above.

Finally, the complex conductivity can be evaluated from R_S and X_S

$$\sigma_1 = \frac{f_0 R_S X_S}{(R_S^2 + X_S^2)^2}, \tag{3.24}$$

$$\sigma_2 = \frac{f_0 \left(X_S^2 - R_S^2 \right)}{2 \left(X_S^2 + R_S^2 \right)^2}. \tag{3.25}$$

If the sample is a good conductor, when we have a so-called Hagen-Rubens limit (see Sec. 3.1), it can be shown that:

$$R_S = -X_S, \tag{3.26}$$

and from Eqs. (3.16) and (3.17) the unknown frequency shift C can be determined. This was the case when we were measuring our samples along a- and b'- crystallographic directions.

In the Hagen-Rubens limit [101]:

$$\sigma_2 \ll \sigma_1 \simeq \sigma_{DC}, \tag{3.27}$$

and

$$\sigma_1 = \frac{f_0}{4R_S^2}. \tag{3.28}$$

The measurements along the c^* crystallographic axis were done in a depolarization regime, since we made mosaics, a single unit of which was shorter than the corresponding skin depth.

3.3.2   Depolarization Regime

In depolarization regime the real part of the conductivity is given by

$$\sigma_1 = \frac{f_0\gamma \cdot \frac{\Delta\Gamma}{2f_0}}{2\left(\gamma + n \cdot \frac{\Delta f}{f_0}\right)^2 + 2n^2\left(\frac{\Delta\Gamma}{2f_0}\right)^2}, \tag{3.29}$$

where n is the depolarization factor of a sample depending only on its shape, γ is a constant that depends only on the filling factor of the cavity for a given resonant mode (see above).

All of the values used for both skin depth and depolarization regimes are given in CGS (Gaussian) units. The surface impedance can be converted to Ohms by multiplying by $Z_0 = 377\,\Omega$ and the conductivity can be converted from s^{-1} to $(\Omega cm)^{-1}$ by using the conversion factor $9 \times 10^{11}\ s^{-1} = 1\ (\Omega cm)^{-1}$.

3.4   Crystal Grow

The crystals of $(TMTSF)_2PF_6$ were electrochemically grown in the technological laboratory of the 1. Physikalisches Institut, Universität Stuttgart. The growth was performed in glass cells (see Fig. 3.9) at room temperatures (22–23 $^\circ$ C) and at 0 $^\circ$ C. The following mixture of chemical components was added into the glass cells and stirred up until the complete dilution of radical ions salts:

- 150 mg TMTSF (in powder form), from "Sigma-Aldrich", catalog Nr. 27,440-2

- 1.06 g Tetrabutylammonium-hexafluorophosphate, from "Sigma-Aldrich", catalog Nr. 28,102-6

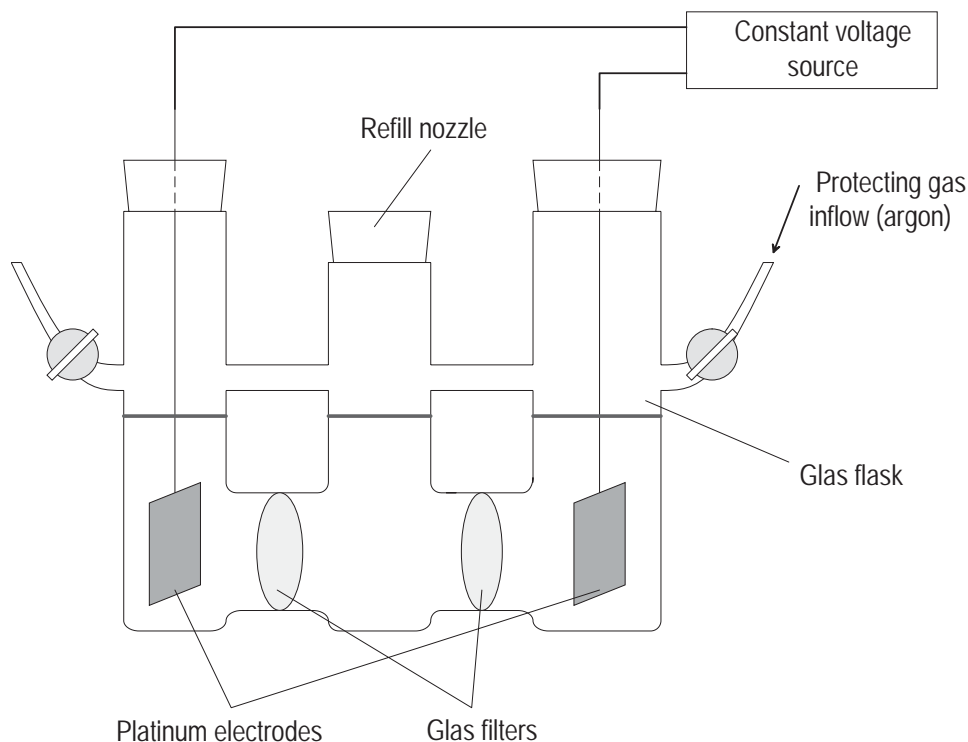- 70 ml Methylenchloride (solvent), from "Sigma-Aldrich", catalog Nr. 15,479-2

Figure 3.9: The crystal grow scheme. Constant voltage is applied to the platinum electrodes, where the needle-shaped crystals of $TMTSF_2PF_6$ are grown on the anode. The porous glass filters (with pores of 10–16 μm in diameter) are used to prevent the electrode from pollution by solid waste of the electrochemical process.

The mixture was filled into glass cells, which were then flushed with argon to avoid oxygen contamination. The platimun electrodes (of approx. 3 cm^2 area) were placed in the cells and tightly closed. During the electrochemical crystallization process we applied a constant voltage (1.5 V) to the electrodes, and the current through the solution was between 9.2 and 13.4 μA. The crystal growth, carried in a dark room, took a time from several weeks to several months, depending on the temperature of the cells environment. During this time, the solvent was permanently filled up into the glass flask under argon atmosphere so that the electrodes were always covered with a liquid. After the crystals of $TMTSF_2PF_6$ reached the needed sizes, they were cleaned with a pure solvent (Methylenchloride), dried and kept in a dark place.

Chapter 4

DC resistivity measurements of (TMTSF)$_2$PF$_6$

There is a long standing controversy whether the transport properties of the Bechgaard salts can be understood in terms of the usual Fermi-liquid (FL) theory, or the Luttinger liquid (LL) theory [67, 83, 30]. The nature of the metallic phase of interacting electron system depends strongly on the dimensionality. It is theoretically well established that the conventional FL theory of 3D metals cannot be applied to the interacting electrons whose motion is confined to one dimension, thus leading to a formation of the LL state (Sec. 2.2).

It is expected that the strongly anisotropic Bechgaard salts may exhibit non-FL like properties at high temperatures (where the thermal energy exceeds the transverse coupling energy) that lead to the loss of coherence for the interchain transport. The crossover from the LL behavior to the coherent one is expected as the temperature (or the frequency) is decreased [78, 104].

While many of the low temperature properties (in the normal state, below 50 K) of the Bechgaard salts are well described by the FL theory [31], their high temperature phase is still poorly understood. The optical conductivity data were interpreted as a strong evidence for a non-FL behavior and the power law asymptotic dependence of the high frequency optical mode has been associated with the LL exponents [105, 58].

On the other hand, the interpretation of the transport and magnetic susceptibility results has not been unambiguous, as some data were interpreted in the framework of the LL model [29, 106], whereas for the other, the FL theory was used [107, 108].

Recently, the long missing basic experiment, the temperature dependence of the Hall coefficient in the metallic phase of the Q1D organic conductor (TMTSF)$_2$PF$_6$ was performed by two groups [114, 109]. Their results were obtained for different geometries and were interpreted differently, i.e., using the conventional FL theory [114] and LL concept [109]. More recently, the theoretical calculations of the in-chain and inter-chain conductivity as well as of the Hall effect in a system of weakly coupled LL chains have been performed [87, 86], giving the explicit expressions as a function of temperature and frequency, but the measurements of the DC transport in (TMTSF)$_2$PF$_6$ along the c^*-axis are not fully understood theoretically within a LL formalism [29, 87].

The aim of the measurements described in this Chapter is to contribute to the solution of these, still open, questions by studying the anisotropic transport properties of the Bechgaard salt (TMTSF)$_2$PF$_6$. The DC measurements are also a good tool to check the quality of the samples we used for microwave frequency measurements. We will describe the experimental details and the geometry of our samples in Sec. 4.1. The experimental results, obtained for both the high-temperature metallic and the low-temperature SDW state are discussed in Sec. 4.2. Finally, the analysis of our data in the normal state and in the SDW state will be presented in Secs. 4.3.1 and 4.3.2, respectively.

4.1   Experimental

High quality single crystals of (TMTSF)$_2$PF$_6$ have been synthesized by the standard electrochemical growth method (see Sec. 3.4). The samples have a needle-shaped form with typical dimensions 2 mm $\times$ 0.5 mm $\times$ 0.1 mm along a, b' and c^*- axis, respectively. The results on the b' axis conductivity were obtained on a narrow slice cut from

a thick crystal perpendicular to the chain axis (the needle's longest dimension); and the typical dimensions of so-made samples were $a \times b' \times c^* = 0.2 \times 1.3 \times 0.3$ mm^3.

Direct current (DC) resistivity measurements were performed using a conventional four-probe technique to eliminate influence of the contact resistances. The contacts were made by evaporating gold pads on the crystal, then 25 μm gold wires were pasted on each pad with a small amount of silver paint. The samples were slowly cooled down to avoid cracks and ensure a good thermal equilibrium with temperature sensors, and the resistivity data were taken in the wide temperature range from 300 K down to 2 K (Helium on pump). The experimental setup is described in details elsewhere [110].

Electrical resistance of several samples was measured along the most conducting longitudinal direction [110, 55], the transversal direction b', and the least conducting transversal direction c^*. The c^* direction is perpendicular to the sheets of TMTSF stacks ($a - b$ plane) and b' denotes the direction normal to a and c^*, and therefore does not completely coincide with the principal crystallographic axis (tilt angle 1.7 degree) [13].

Typical set of resistivity ρ_{DC} *versus* temperature T for all three directions is displayed in Figure 4.1. In general terms, the temperature behavior of the resistivities of (TM)$_2$X along the a, b' and c^* axes has a similar feature: a metal-to-insulator transition occurs at $T = 12$ K due to the developing spin density wave (SDW); this value, obtained from the derivatives of our data, is in good agreement with the literature. Below we will discuss our findings separately for high-temperature normal phase and low-temperature SDW ground state.

4.2 Experimental Results

Due to the long, needle-shaped crystals of (TM)$_2$X compounds, the DC conductivity along the longest chain axis a of (TMTSF)$_2$PF$_6$ is most intensively studied. Despite of some differences in the absolute value of the room-temperature a-axis conductivity, its temperature behavior was scrutinized by various groups [13, 111, 19, 112, 29, 113].
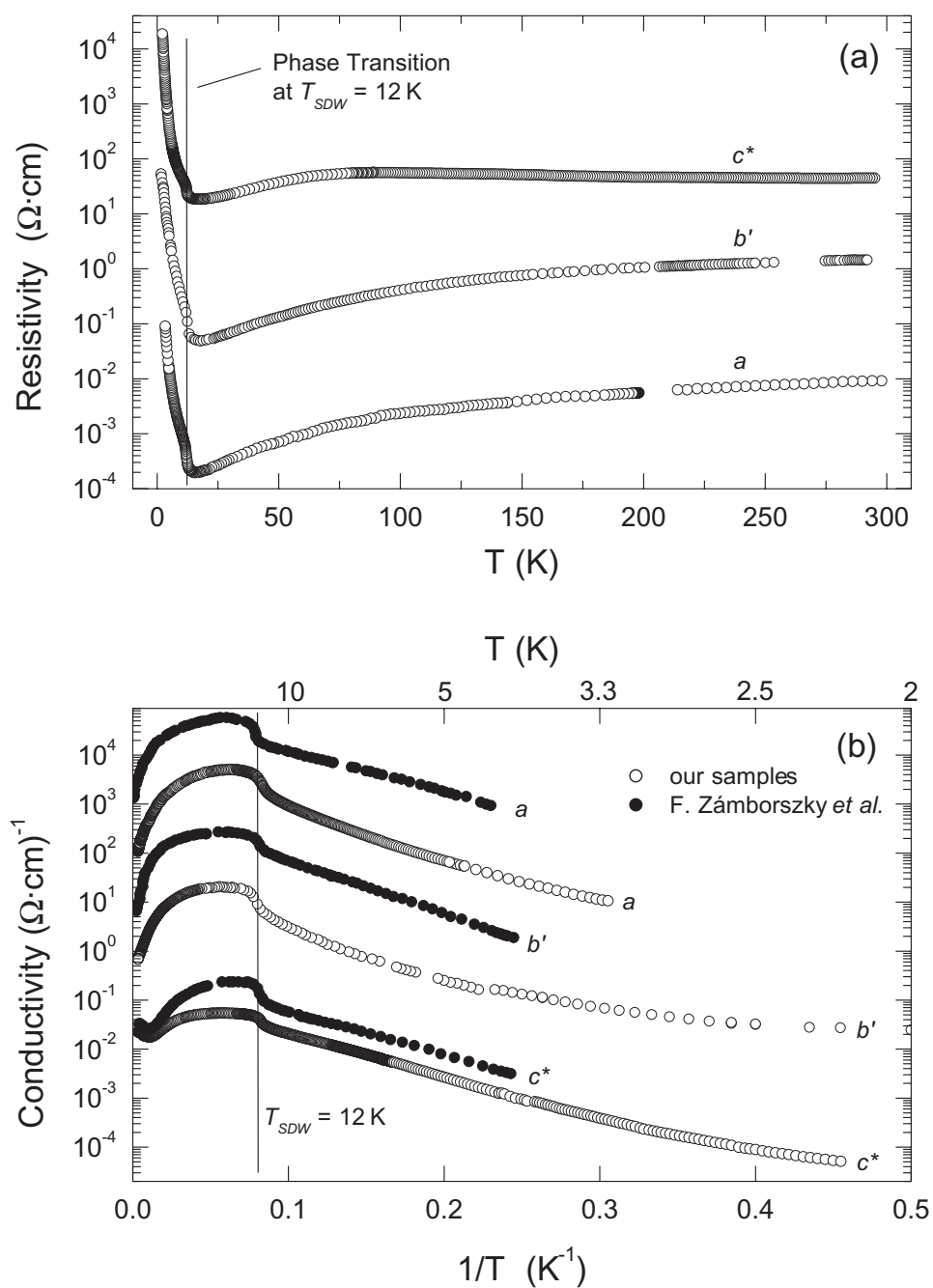
Figure 4.1: (a) Temperature dependence of the DC-resistivity of (TMTSF)$_2$PF$_6$ measured along the a, b', and c^* crystallographic directions. (b) DC-conductivity as a function of inverse temperature for all three directions (open circles) compared with the data from [113] (solid circles).

The a-axis resistivity obtained in our experiments agrees well with the previously published data [13, 111, 19, 112, 29, 113, 30]. In the normal state (i.e., above the metal-insulator transition at $T_{SDW} = 12$ K) it has a metal-like behavior, and the decrease of the resistivity between the room temperature and $T \approx 100$ K can be fitted to a $\rho_a(T) \sim T^{1.3}$ power law (Fig. 4.3). Below 70 K, the resistivity follows the law $\rho_0 + AT^2$, which is valid down to the metal-insulator (SDW) transition at 12 K (see inset in Fig. 4.3). For our samples, values of $\rho_0 = 1.1 \times 10^{-4}$ Ω·cm and $A = 0.2$ $\mu\Omega$·cm·K^{-2} are found; the low value of the residual resistivity ρ_0 together with a high resistivity ratio ρ_{300K}/ρ_{20K} are the indicatives of a very high crystal quality. The quadratic temperature dependence of the resistivity suggests that the inelastic electron scattering is dominant in the normal state at low temperatures [30].
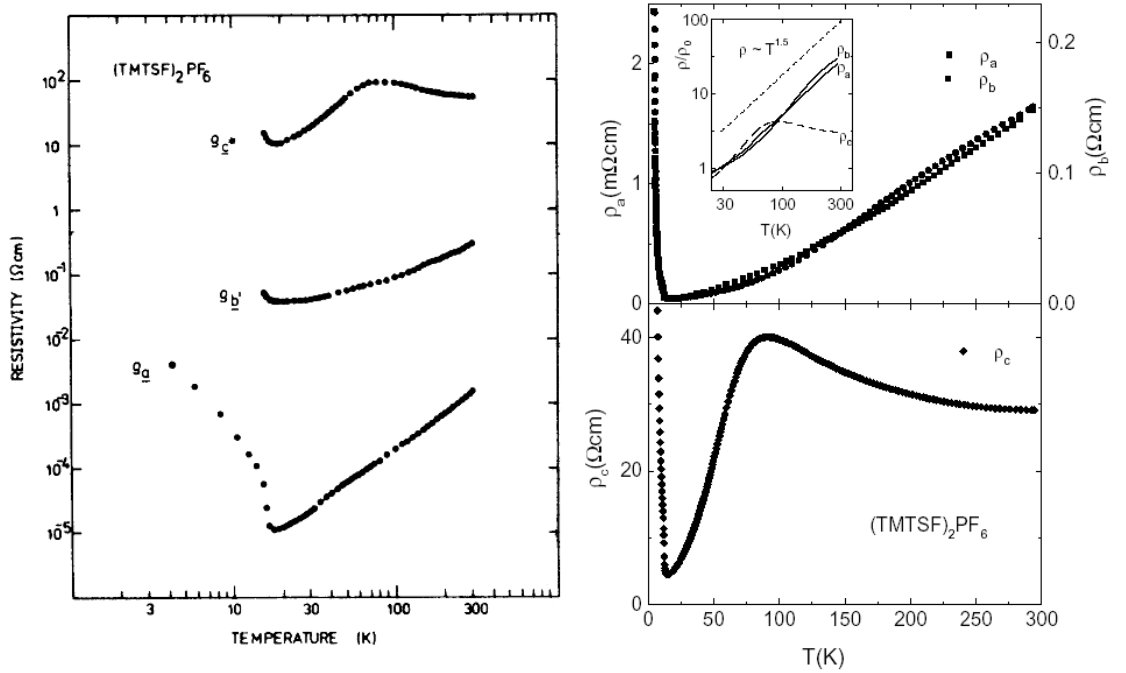
Figure 4.2: Temperature dependence of the a, b', and c^* resistivity of (TMTSF)$_2$PF$_6$, as taken from Ref. [111] (left graph); and of the a, b', and c^* resistivity of (TMTSF)$_2$PF$_6$, as taken from Ref. [114] (right graph).

To our knowledge, there are only two papers reporting on the DC measurements

of the b'-axis conductivity of (TMTSF)$_2$PF$_6$ crystals (Fig. 4.2). The former is the original paper of Jacobsen *et al.* [111], which was the only available result for almost 20 years. The latter is the recent publication of G. Mihály *et al.* [114], who obtained their data using the Montgomery method for a single crystal [115], as well as independent longitudinal four-probe measurements along the b' axis. These two results strongly contradict each other; and our findings are in a very good agreement with the report of G. Mihály *et al.* [114].

The intermediate conductivity direction also shows a metal-like behavior of $\rho(T)$; the resistivity along this direction decreases almost as steeply as $\rho_a(T)$. However, it follows the dependence $\rho_{b'}(T) \sim T^{0.84}$ between 300 and 200 K and changes to the $\rho_{b'} \sim T^{1.63}$ power law on further cooling down to 80 K (Fig. 4.3). Below 70 K, as that for $\rho_a(T)$, it can be perfectly described by a quadratic power law: $\rho_{b'}(T) \sim T^2$ (see inset in Fig. 4.3).

Finally, for the lowest conducting, c^* direction, our data are consistent with the previously published results [111, 29, 114]. ρ_{c*} increases by about a factor of 1.5 when going down to 90 K. Below 90 K $\rho_{c*}(T)$ falls rapidly before turning upwards again below 15 K. In the temperature range between 35 and 65 K it follows a metallic behavior with $\rho_{c*} \sim T$. The quadratic dependence of the resistivity below 65 K was not observed in this direction (see inset in Fig. 4.3).

4.3   Analysis and Discussion

4.3.1   Normal State

First of all, it should be noted that all our data are obtained at ambient pressure. As it is known for the Bechgaard salts (TM)$_2$X, much of the temperature dependence of their conductivity at high temperatures arises from the thermal expansion [30]. Consequently, the constant-pressure data usually show different temperature dependences than the constant-volume data. In order to be able to directly compare our
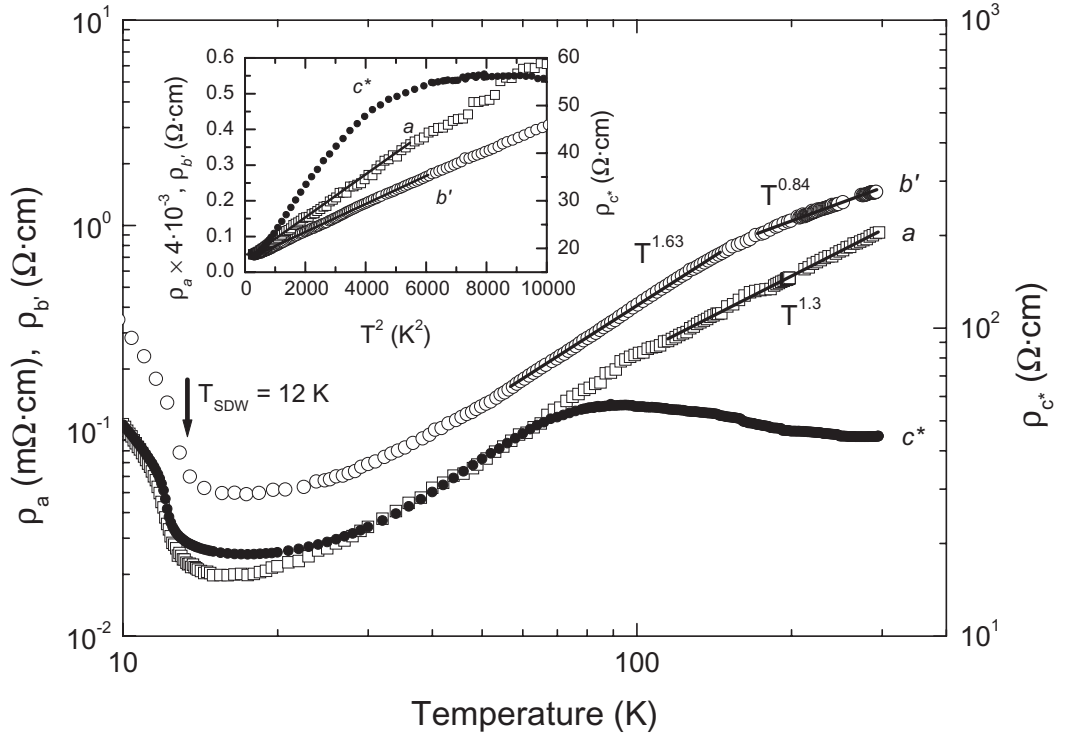
Figure 4.3: Temperature dependence of the DC resistivity of $(TMTSF)_2PF_6$ measured along the a (open squares), b' (open circles), and c^* (solid circles) crystallographic directions in log-log scale. The inset depicts the T^2 dependencies of the resistivities below 100 K. Note, that below 65 K $\rho_{c^*}(T)$ cannot be described by a quadratic dependence; instead it follows square root behavior of T^2, i.e., $\rho_{c^*}(T) \sim T$.

constant-pressure $\rho(T)$ experimental data with the theoretical models for constant-volume $\rho^{(V)}(T)$ dependences, a conversion has to be performed. We utilize for that a conversion procedure, as it was done before for $(TM)_2X$ salts [30, 88]. We take the unit cell at 16 K at ambient pressure as a reference unit cell – when the temperature T is increased, a pressure P must be applied (at a given T) in order to restore the reference volume. Taking into account, that in the metallic phase ρ_a varies by 10% per 1 kbar [29, 114] for all T values above 50 K; the measured resistivity ρ_a is then converted into a constant-volume value $\rho_a^{(V)}$ using the expression $\rho_a^{(V)} = \rho_a/(1 + 0.1P)$. Although the value of 25% is reported in Ref. [29], the data taken from this paper

and displayed in Fig. 4.4 (top panel) show this value to be around 10%, and we ascribe this fact to an unfortunate misprint of the authors. The analogous procedure is applied to get $\rho_{b'}^{(V)}$ and $\rho_{c*}^{(V)}$, taking into account that the variation of $\rho_{b'}$ and ρ_{c*} in the metallic phase for all T has the same value of 10% kbar^{-1} [29, 114] (Fig. 4.4).

At low temperature, $T < 50$ K, both the thermal expansion and the pressure coefficient are small [30, 116]. Therefore, the constant-volume temperature dependence of the resistivity does not derivate from the quadratic law observed under constant pressure.

The calculated values of the temperature dependencies of the constant-volume resistivity $\rho_a^{(V)}$, $\rho_{b'}^{(V)}$ and $\rho_{c*}^{(V)}$ between 100 K and the room temperature are shown in Fig. 4.5. As a consequence of constant-pressure to constant-volume corrections of our data described above, the temperature behavior of the DC resistivity along all three crystallographic axes of (TMTSF)$_2$PF$_6$ possesses the reduced power laws.

Along the linear chain axis, the constant-volume resistivity follows the power law $\rho_a^{(V)} \sim T^{0.56}$ temperature behavior. The temperature dependence of the transverse b'- axis constant-volume resistivity can be fitted by $\rho_{b'}^{(V)} \sim T^{0.24}$ and by $\rho_{b'}^{(V)} \sim T^{1.31}$ in the temperature ranges 200 K$< T <$300 K and 100 K$< T <$150 K, respectively (see Fig. 4.5). The constant-volume resistivity along the least conducting axis c^* experiences a semiconducting behavior from room temperature down to 93 K, somewhat stronger than that for a constant-pressure dependence; it follows $\rho_{c*}^{(V)} \sim T^{-0.95}$ temperature dependance in the temperature range 150 K$< T <$300 K.

In the rest of this Section we will consider a resistivity in the sense of a resistivity in conditions of unchanged unit cell volume, i.e., the constant-volume values, and we will omit the superscripts "(V)".

The in-plane conductivity ($\sigma_\parallel$) and inter-plane conductivity ($\sigma_\perp$) have been calculated for a system of weakly coupled Luttinger chains [87, 86]. It was found that the inter-chain hopping ($t_\perp$ is a perpendicular hopping integral) is responsible for the metallic character of the (TMTSF)$_2$X compounds, which otherwise would be Mott

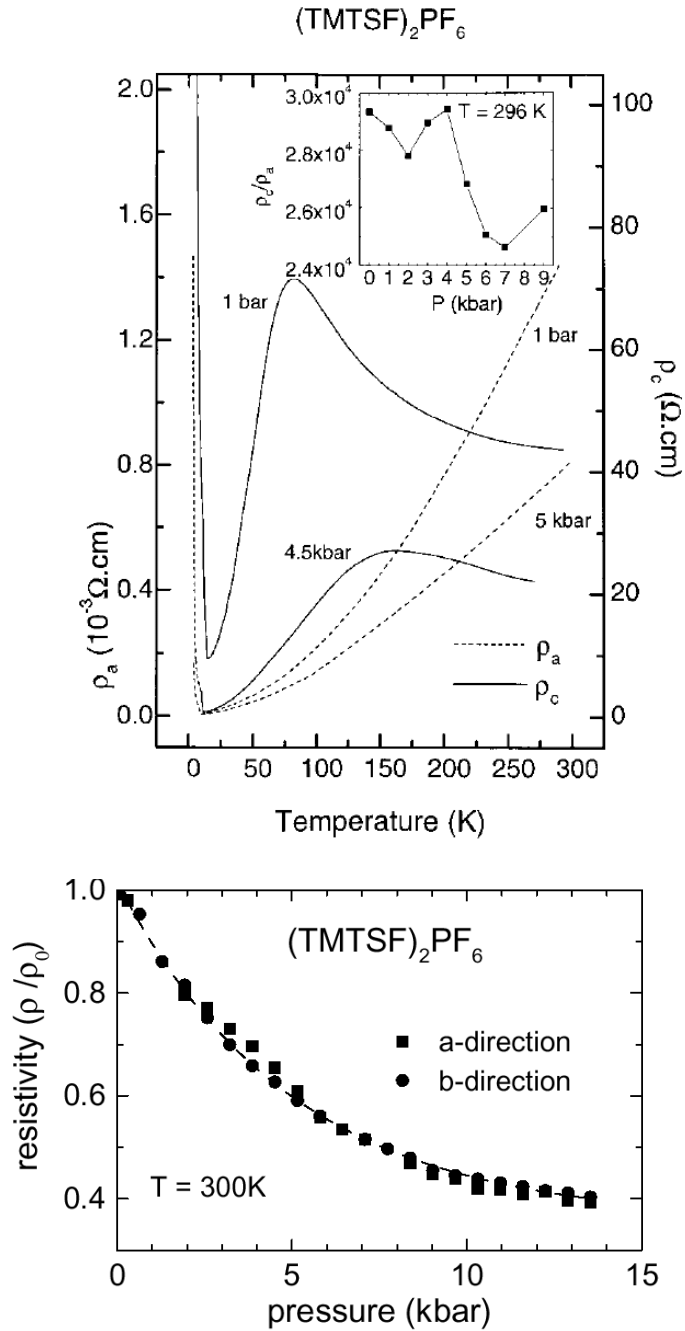Figure 4.4: (Top panel) Temperature dependence of the DC resistivity for $(TMTSF)_2PF_6$ along the chain axis a (dashed curve) and transverse axis c^* (solid curve), as taken from Ref. [29]. When changing the pressure from 1 bar to 5 kbar, the a-axis resistivity changes 50%, meaning that the pressure coefficient for the resistivity is 10% per kbar. The inset depicts the pressure dependence of the ratio ρ_a/ρ_{c^*},which is almost pressure independent (within 10%). (Bottom panel) Pressure dependence of the DC resistivity of $(TMTSF)_2PF_6$ along a and b' axes as taken from Ref. [113]; in the low pressure domain the pressure coefficient is 10%.
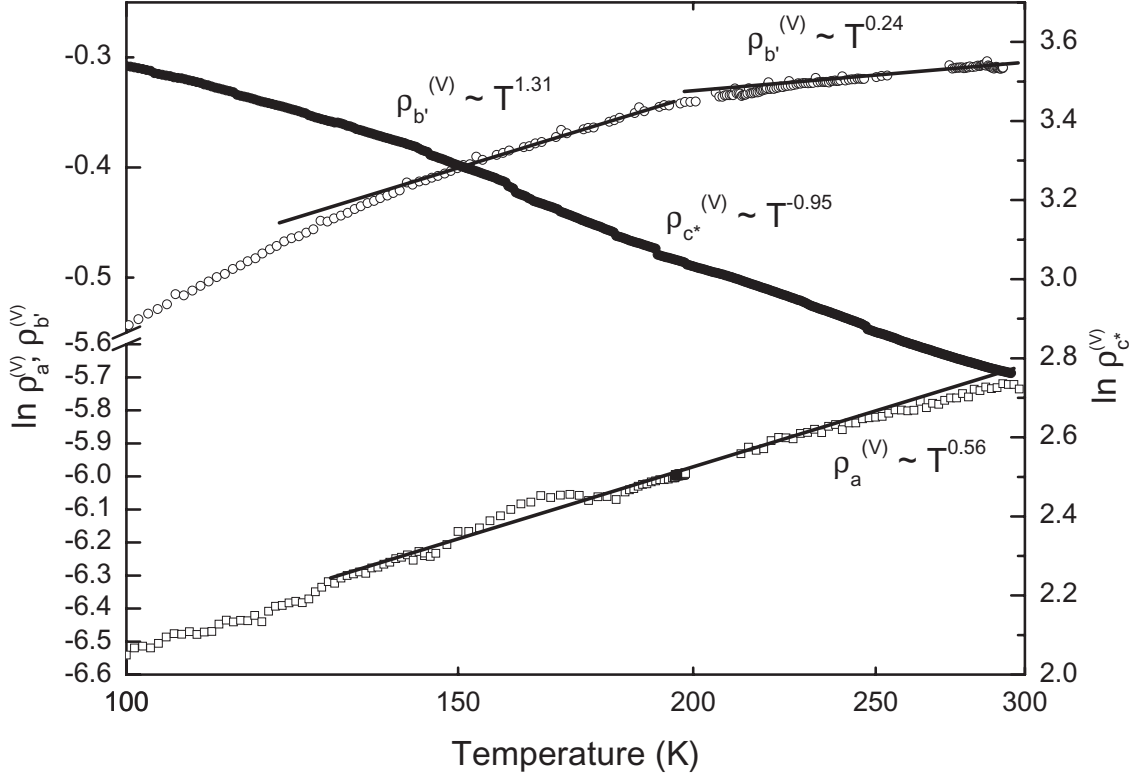
Figure 4.5: The log-log scaled temperature dependence of the constant-volume resistivity of $(TMTSF)_2PF_6$ along the a (open squares), b' (open circles), and c^* (open triangles) axes, as derived from our analysis.

insulators. The temperature (or the frequency ω) power-law was found, giving for the longitudinal and transverse resistivity respectively

$$\rho_{\parallel}(T) \sim (g_{1/4})^2 T^{16K_\rho - 3}, \tag{4.1}$$

$$\rho_{\perp}(T) \sim T^{1-2\alpha}, \tag{4.2}$$

where $g_{1/4}$ is the coupling constant for the umklapp process with $1/4$ filling, K_ρ is the LL exponent controlling the decay of all correlation functions ($K_\rho = 1$ corresponds to non-interacting electrons and $K_\rho < 0.25$ is the condition upon which the $1/4$ filled umklapp process becomes relevant) and $\alpha = 1/4(K_\rho + 1/K_\rho) - 1/2$ is the Fermi surface exponent (see Sec. 2.2.3).

The comparison of our experimental data, where $\rho_\parallel = \rho_a \sim T^{0.56}$, with the above LL theoretical model yields $K_\rho = 0.22$, the value that is in good agreement with the value $K_\rho = 0.23$ for $(TMTSF)_2PF_6$ obtained from the temperature dependence $\rho_a(T) \sim T^{0.5}$ in the 100 K$< T <$300 K range [109, 86]. For the frequency dependent conductivity parallel and perpendicular to the chains the behavior

$$\sigma_\parallel(\omega) \sim \omega^{16K_\rho - 5},\tag{4.3}$$

$$\sigma_\perp(\omega) \sim \omega^{2\alpha - 1}\tag{4.4}$$

is predicted [87]. Optical experiments on $(TMTSF)_2X$ (where X = PF_6, AsF_6, and ClO_4) along the chains [105, 58] yield $K_\rho = 0.23$.

If we use this value $K_\rho = 0.22$ obtained from the measurements parallel to the chains in order to describe the results we obtained from the measurements perpendicular to the chains, some inconsistency arises: with $K_\rho = 0.22$ we would expect for the transverse resistivity the power law $\rho_\perp \sim T^{-0.36}$, while our experimental result gives $\rho_{c^*} \sim T^{-0.95}$. However, the theoretical model was compared with the c^*-axis resistivity results [87, 29], which, in our opinion, is not the best choice: the comparison should be applied to t_b and $\rho_{b'}$ in the first place, rather than to t_c and ρ_{c^*}, because $t_b \gg t_c$. This means that if we assume the Luttinger chains along the a direction, we should consider the b direction as the direction, where the chains are weakly coupled above all. Nevertheless, a comparison of the calculated transverse resistivity $\rho_\perp \sim T^{-0.36}$ with the experimentally obtained $\rho_{b'} \sim T^{0.24}$ in the temperature range 200 K$< T <$300 K and $\rho_{b'} \sim T^{1.31}$ in the temperature range 150 K$< T <$200 K provides even stronger evidence against the LL picture. Hence we have to point out that for $(TMTSF)_2PF_6$ the DC transport along the transversal axes cannot be understood within the LL picture. Another possibility to interpret the DC transport properties of our object of investigations is to turn to the conventional Fermi-liquid theory.

The simplest model of the electronic transport in metals is the Drude model [49], where all relaxation processes are described by a single particle relaxation time τ:

$$\sigma_{DC} = \frac{Ne^2\tau}{m^*}, \qquad\qquad (4.5)$$

where N – a charge carrier concentration, e – an elementary charge, m^* – an effective mass of the charge carriers. The anisotropy of the resistivity $\rho_{DC} = 1/\sigma_{DC}$ values can be accounted for by an anisotropic band mass m^*. Going beyond the Drude model, the scattering rate $\Gamma = 1/\tau$ may be frequency dependent [49].

As plotted in Fig. 4.3, ρ_a and $\rho_{b'}$ have quite coinciding temperature profiles; the correspondent curves scale together. Consequently, the anisotropy $\rho_{b'}/\rho_a$ is almost temperature independent (within 20%) in the temperature range from room temperature down to 50 K, and goes from the value of 180 at $T = 50$ K to approximately 300 at 13 K, just above the metal-insulator transition (Fig. 4.6). This temperature behavior of the anisotropy is in good agreement with recent results [114], which we have already mentioned above.

The proportionality $\rho_a(T) \sim \rho_{b'}(T)$ suggests a simple anisotropic band structure with isotropic relaxation time $\tau(T)$. Thus the homogeneous relaxation rate, describing the similar T dependencies observed for a and b' directions, provides a strong evidence forward a conventional FL picture. At the same time, in (TMTSF)$_2$PF$_6$, the temperature dependences of ρ_a (Ref. [117]) and the Hall coefficient, between room temperature and the lowest temperatures, were quite satisfactorily compared with the FL theoretical model where the electron relaxation time varies over Fermi surface [118, 119]. According to this model, in the high temperature region (where $T > t_c \approx 10$ K and $T < t_b \approx 300$ K) the system is treated as a 2D FL. It is proposed that a quasi-1D conductor behaves like an insulator ($d\rho_a/dT < 0$), when its effective dimensionality equals one, and like a metal ($d\rho_a/dT > 0$), when its effective dimensionality is greater that one.

The small bandwidth also suggests that a tight binding approximation is appropriate. In the tight binding model (Sec. 1.2.3) a quarter-filled band has a conduction anisotropy of [27]:
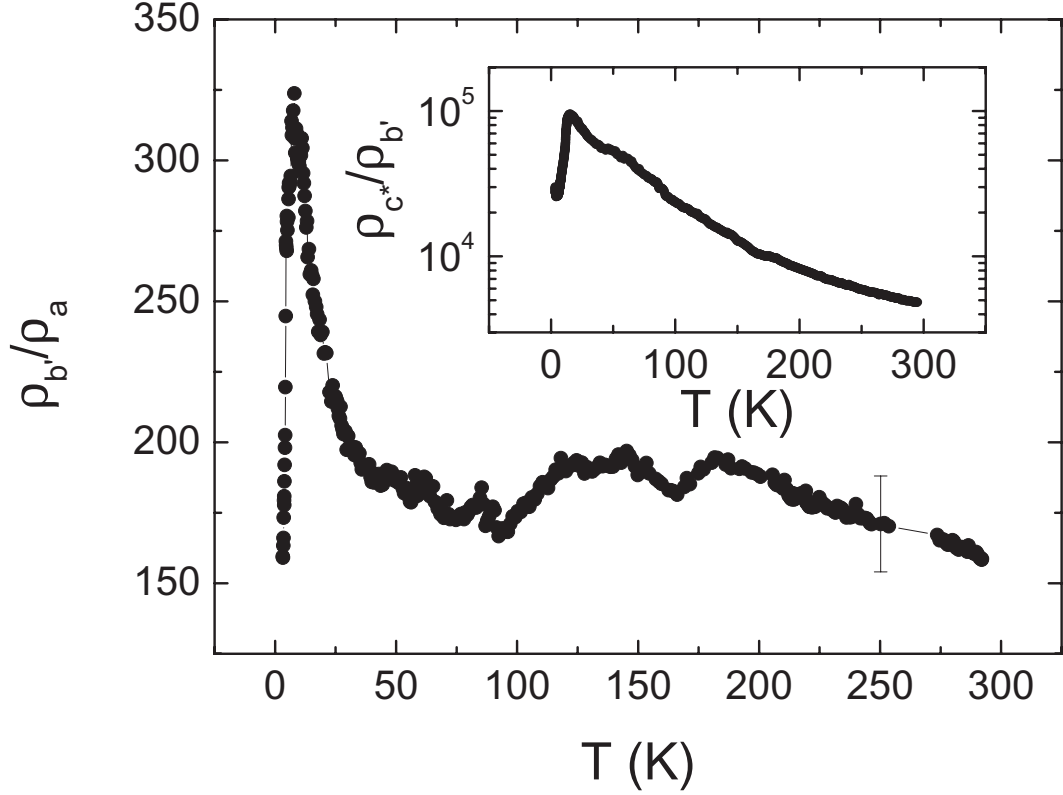
Figure 4.6: Temperature dependence of the anisotropy of the DC resistivity $\rho_{b'}/\rho_a$. Inset: temperature dependence of the anisotropy $\rho_{c^*}/\rho_{b'}$.

$$\frac{\rho_b}{\rho_a} = \frac{\sigma_a}{\sigma_b} = \left(\frac{a_s}{b}\right)^2 \cdot \left(\frac{t_a}{t_b}\right)^2, \tag{4.6}$$

where $\rho_a(\sigma_a)$ and $\rho_b(\sigma_b)$ are the resistivity(conductivity) in the a-axis direction and in the direction perpendicular to the a-axis, respectively. t_a, t_b are the transfer integrals along the a and b' directions; $a_s = a/2$ is the intermolecular distance along the a-axis, and b is the interchain distance to the neighboring stack (see Sec. 1.2.1).

Using $4t_a = 1.0$ eV (see Sec. 1.2.3) together with measured resistivities gives ($4t_a$: $4t_b$: $4t_c$) $\approx$ (1 : 4 $\times$ 10^{-2} : 4 $\times 10^{-3}$) eV = (11600 : 460 : 46) K, which is quite close to the anisotropy ($4t_a$: $4t_b$: $4t_c$) = (1 : 6.7 $\times$ 10^{-2} : 3 $\times$ 10^{-3}) eV as determined by P. M. Grant by band structure calculations [24]. Here we have to

admit that the $\rho_{c*}/\rho_{b'}$ anisotropy is not quite temperature independent, as seen from the inset of Fig. 4.6. Therefore we can speak only about an estimate of the transfer integral along the $c*$ direction in the order of magnitude.

Equation (4.6) establishes that whenever the collective modes do not contribute to σ_a, the conductivity anisotropy is approximately given by the square of the band structure anisotropy. It should thus not be strongly temperature dependent [27], as depicted in Fig. 4.6. This relation is certainly valid at low temperature, where the mean free path $\ell_{b'} \approx 20$ Å along the b' direction exceeds the lattice constant ($b = 7.7$ Å) [111, 114]. With increasing the temperature, $\ell_{b'}$ decreases below the distance between the chains b at $T_X \approx 50$ K [111, 114], and above this temperature the interchain propagation becomes diffusive. For such an incoherent motion the perpendicular hopping probability is given by $\tau_b^{-1} = \tau(t_b/\hbar)^2$ [120], i.e., it is determined by the lifetime along the chain direction. As a consequence, even a diffusive b'-direction transport follows the temperature dependence of the relaxation time τ, moreover, the magnitude of the anisotropy is the same as in the case of the coherent b'-direction transport (within a factor close to unity) [120].

A coherent-diffusive crossover has not been observed along the c^* direction either, where the mean free path is much smaller than the intermolecular distance [108]. The resistivity anomaly observed in $\rho_c(T)$ (Fig. 4.3) can easily be related to the fact that along the c^* direction the chains are separated by the PF$_6$ anions; thus the transport may rather be characteristic of a hopping process through the anions than of the nature of an ideal anisotropic electron system [108].

4.3.2 SDW State

Although in Chapter 2.1 we have considered the SDW and the CDW as a purely 1D phenomenon, one can easily imagine a 3D Fermi surface, which can satisfy the nesting conditions in all three principal directions, leading to the formation of a density wave ground state along each direction. The transport properties of the low-temperature SDW ground sate in (TMTSF)$_2$PF$_6$ is well studied along the a axis, but there is still

a lack of data in the transversal directions. We have found that at low temperature the spin density wave state develops below $T = 12$ K along the a, b', and c^* directions (Fig. 4.1). The activation behavior along all these directions is clearly seen, as shown in Fig. 4.7.

The corresponding values of a single particle energy gap Δ_0 opened along the a, b', and c^* directions are 27.1, 27.4 and 20.5 K, respectively (Fig. 4.7). On cooling down further, somewhat below 6 K, the activation behavior gives the value of the gap of 20.8 K, 21.3 K, and 18.4 K for a, b', and c^* direction, respectively (see Fig. 4.7). This slight change of an activation behavior may be due to the heating of our samples at very low temperatures, below 6 K.

The values of the single particle gap Δ_0 we found from our measurements are in good agreement with earlier findings from the DC measurements along the a axis with a value of Δ_0=21 K [113] and Hall coefficient measurements with two different configurations: when the current $J \parallel a$ and the magnetic field B was applied along c^* axis ($B \parallel c^*$, Δ_0=23 K) [114] and when the applied magnetic field was parallel to the b' axis ($B \parallel b'$, Δ_0=24 K) [121].

The values of the single particle gap (at zero frequency), which we found for the three crystallographic axes, can be perfectly described by a mean-field BCS theory (see Sec. 2.1.4), which gives

$$2\Delta_0(T = 0) = 3.528 k_B T_C, \tag{4.7}$$

where Δ_0 is the single particle gap at $T = 0$, k_B is the Boltzmann constant, and T_C is the transition temperature. For the transition temperature we have obtained from the derivative of our data T=12 K we get Δ_0=21 K, which coincides excellently with our results.
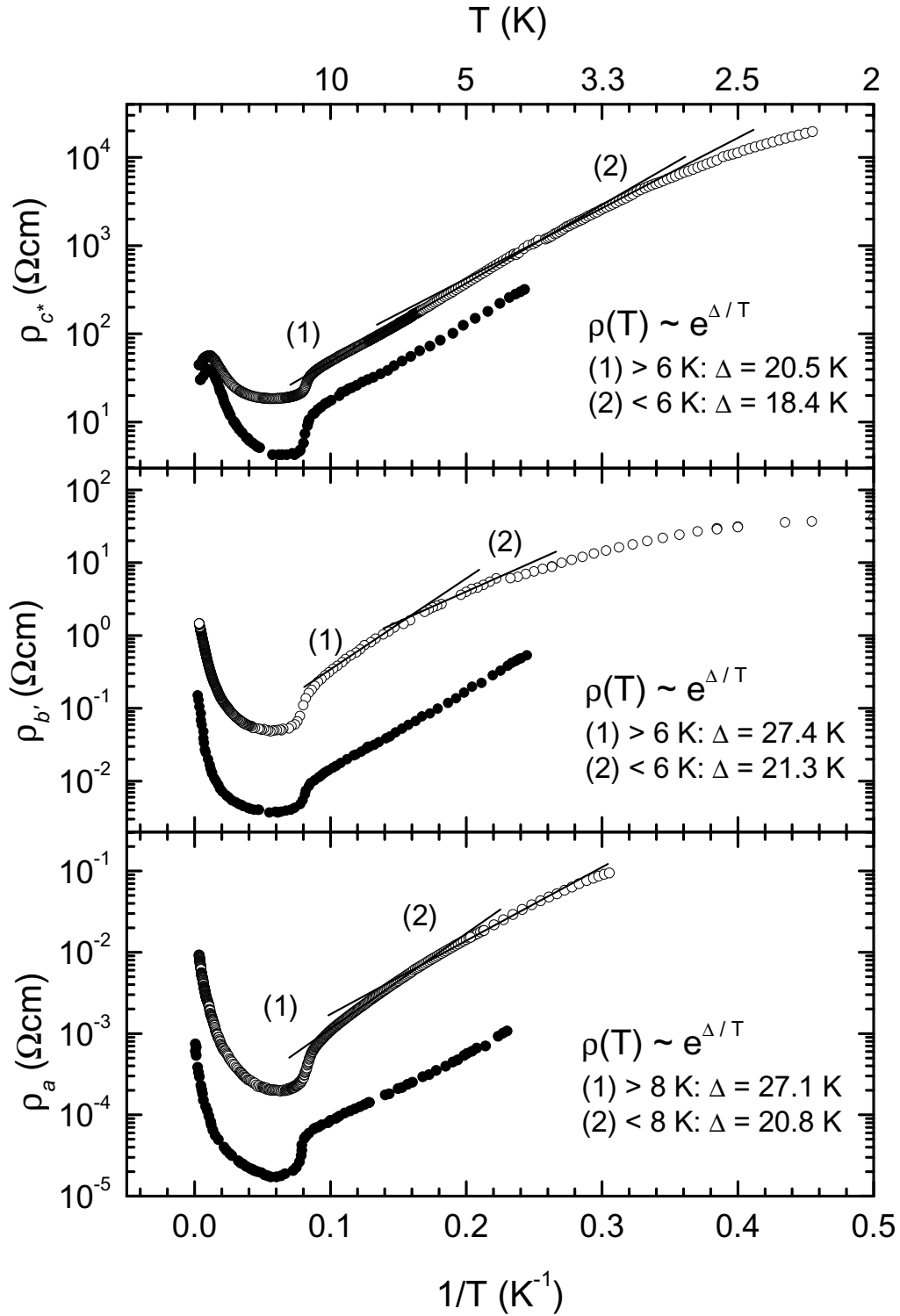
Figure 4.7: Arrhenius plot of the DC resistivity of (TMTSF)$_2$PF$_6$ along the c^*, b', and a directions (top, middle, and bottom panel, respectively.). Open circles depict our measurements, solid circles correspond to data, taken from Ref. [113]. The activation energy Δ is given for each direction.

Chapter 5

Microwave Investigations of (TMTSF)$_2$PF$_6$

Among all the experimental approaches used to study the dimensionality of the electron gas in Bechgaard salt, transverse transport measurements are particularly relevant to directly probe of interchain coupling. It was further realized that since the transverse transfer integrals are small, an electric field applied along the b' or c^* directions could also act as a probe of the physical properties in the plane perpendicular to that direction. Our DC measurements along the axis c^*, described in the previous Chapter, have shown a non-monotonic behavior of the temperature profile: a maximum of ρ_{c^*} was observed near 80 K. Earlier, a strong pressure dependence of this unusual feature was evidenced [29] and a typical 1D power law profile was found above the characteristic ρ_{c^*} maximum. This maximum was then ascribed to a broad crossover regime indicative of a deconfinement of the charge carriers from the chain axis; this results in a gradual onset of coherent transport along b' direction below 80 K, suggesting then a FL behavior in the $a - b'$ plane. However, from our DC measurements we did not observe the temperature independence of the anisotropy ratio ρ_{c^*}/ρ_a (see the inset in Fig. 4.6), as expected from FL arguments; it was also found to be temperature dependent in the only previous work [29]. These observations contrast with the work of Gor'kov *et al.* [122, 123, 124] who argued that the longitudinal

transport properties, below 60 K and down to the SDW transition temperature, can be well accounted for in terms of a weakly interacting Fermi liquid. However, such a quasi-particle like signature should also be detected in the b' transverse direction.

Reliable measurements of the transverse transport properties along b' direction are highly needed to clarify the present controversy. Unfortunately, since the Bechgaard salts have a pronounced needle shape whose axis is parallel to the chains, transverse transport along b' is particularly difficult to perform with usual DC methods. Owing to non-uniform current distributions between contacts, parasitic contributions from other directions can be introduced. These problems can be avoided by using a contactless microwave technique which allows a better control on the orientation of the current lines in these organic needles.

The low-temperature SDW ground state of (TMTSF)$_2$PF$_6$ is also of great interest to examine in the microwave frequency range. It was proposed that the modulation of the spin density is weakly incommensurate with the underlying lattice [125], and the collective mode can slide carrying current. But impurity pinning causes the collective mode to resonate at finite frequencies, the pinned mode resonance usually occurs in the millimeter wave spectral range in nominally pure specimens, as it was proposed for both the CDWs [126, 127, 128], and for the SDWs [61]. Upon application of an external electric field, the collective mode can be depinned and carry current [129, 112, 130]. The electrodynamics of the SDW state was well studied at several microwave frequencies (3–100 GHz) along the linear chain axis a [131, 132]. To our knowledge, the microwave transport properties of (TMTSF)$_2$PF$_6$ in the SDW state were never reported along the transverse directions (b' and c^*). And we have contributed to fill this lack of data by the investigations described in this Chapter.

In this Chapter we report microwave resistivity data obtained along both longitudinal and transverse directions of (TMTSF)$_2$PF$_6$ crystals. The different sample geometries we employed for our measurements at different polarizations are discussed in Sec. 5.1. We have used a conventional cavity perturbation technique, which is described in Sec. 3.2, at 33.5 and 24 GHz to obtain the electrical resistivity along

each crystal axes as a function of the temperature (2–300 K). We will report on our findings at 33.5 and 24 GHz in Secs. 5.2 and 5.3, respectively.

5.1 Sample Preparation

The single crystals of $(TMTSF)_2PF_6$ have been synthesized by the standard electrochemical method (Sec. 3.4) with typical needle-like shape along the a-direction. We have performed our microwave investigations along the a-directions employing for that naturally grown needles of typical dimensions of 1 mm $\times$ 0.2 mm $\times$ 0.2 mm. Unfortunately, such a needle geometry is not suitable for precise measurements of the transverse properties; this is particularly true for our microwave technique which yields very accurate data only when the electric field is oriented along the needle's axis. In order to perform the microwave measurements along the b'-direction, we have grown thick samples of the width of up to 1.8 mm in the transversal b'-direction. These thick needles were cut perpendicularly into pieces of a needle shape, where the b'-direction was the direction along the needle. Such single crystals of typical dimensions of 1.2 mm $\times$ 0.2 mm $\times$ 0.2 mm were used to perform measurements along the b' transverse direction, and a typical sample is shown in Fig. 5.1a. Unfortunately, it turns out that one cannot grow $(TMTSF)_2PF_6$ crystals thick enough to perform single crystal measurements along the c^*-axis, the maximal thickness along this transverse direction is about 0.2 mm. Each crystal was therefore cut into several pieces (Fig. 5.1b) so that it could be reconstructed with a shape of a needle having the crystal c^* direction as its longest axis (Fig. 5.1c), the typical dimensions of such mosaics samples were 0.8 mm $\times$ 0.2 mm $\times$ 0.2 mm. The small sample blocks were attached with vacuum grease "Apiezon N" to the quartz plate of dimensions slightly exceeding the dimensions of the sample and of the thickness of 0.07 mm. The commercially available vacuum grease "Apiezon N", which is known to be transparent in the microwave range, remains malleable down to the very low temperatures (down
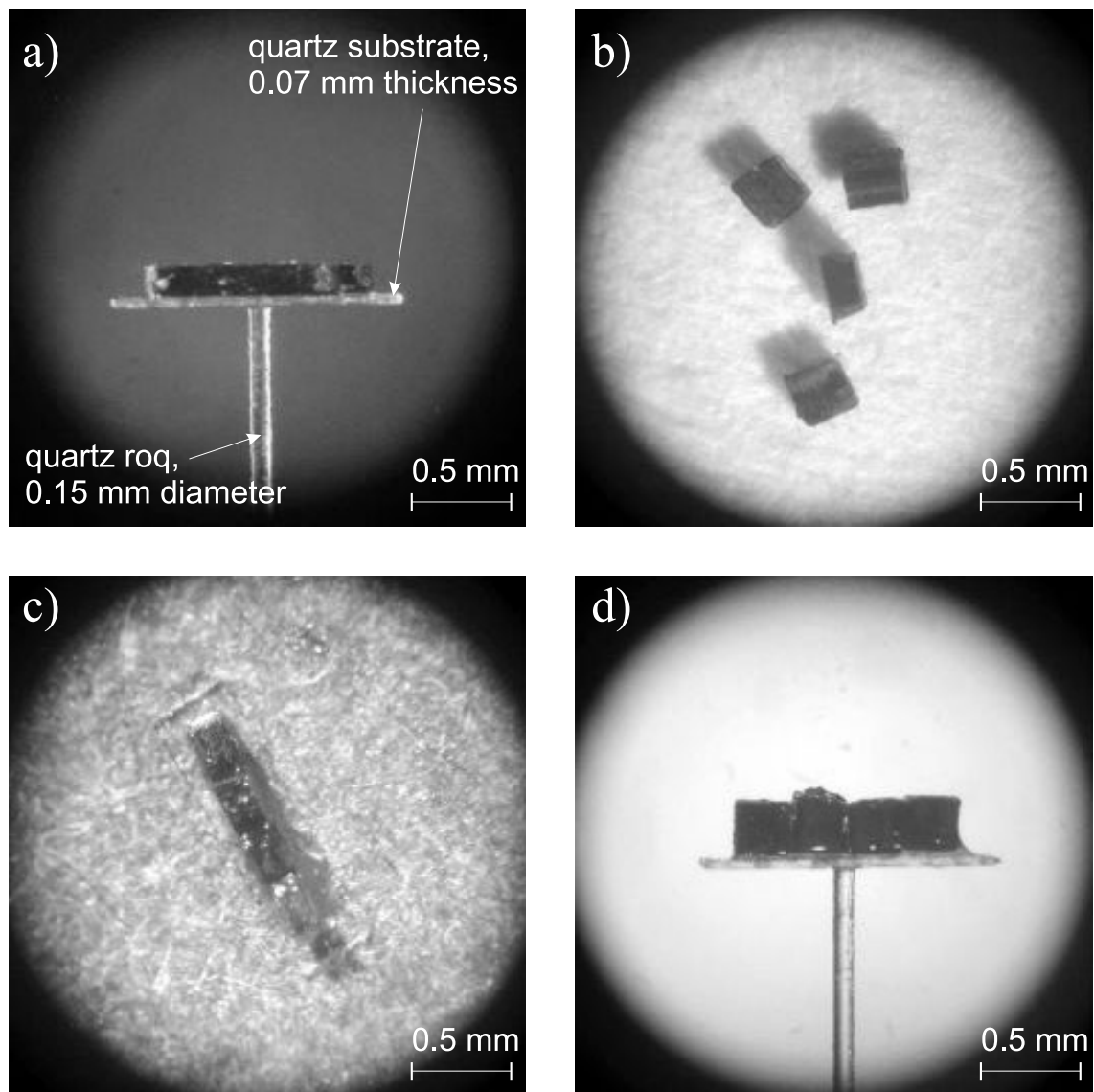
Figure 5.1: The sample arrangements in our experiments. (a) The typical sample arrangement we utilized for the measurements along the a or b' crystallographic axis is shown. (b) The blocks for reconstruction the c^*-needle are shown. (c) Mosaics sample (c^*-needle) built from the four blocks on the transparent substrate, top view. (d) Mosaics on the substrate forming the c^*-needle sample is attached to the quartz rod, side view.

to 4 K) and thus can not cause the damage of the samples due to the thermal contraction, which is typically valuable in the temperature range from room temperature down to 70 K. The quartz substrate also does not absorb the microwave radiation, it rather introduces a small frequency shift, which can be excluded by performing the reference (i.e., that of unloaded cavity) measurements with the same quartz plate. Finally, the quartz substrate with the sample atop of it is glued to the quartz rod of diameter of 0.15 mm (Fig. 5.1d) and placed at the position of the maximal electric field (see Sec. 3.2.4). As it was discussed above (Sec. 4.2), the transport properties of Bechgaard salts are very sensitive to the applied external pressure. In order to be sure that there was no mechanical stress due to the confinement to the substrate, we also employed the substrate configuration in the measurements performed on the single crystals along the a and the b' directions (see Fig. 5.1a). Having done our measurements both with and without the substrate, we can conclude that there is no influence of the substrate on the results of our investigations, and we will discuss it in the next Section in more details.

5.2 Microwave Investigations of (TMTSF)$_2$PF$_6$ at 33.5 GHz

At 33.5 GHz we have performed the measurements along all three crystallographic axes: a, b', and c^*. The samples were cooled slowly (at the typical cooling rate of 0.1–0.3 K per minute) to the lowest temperature of 2 K to prevent microcracking and outright breakage, which was evidenced by a sharp increase in the resonance frequency. In general, crystals of the same crystallization batch yielded similar properties; however, we did notice changes in the SDW response below 3.5 K (but not the normal state properties) after repeated cycling to room temperature, we will discuss these anomalies in Sec 5.4.3. Consequently, thermal cycling was avoided and measurements were generally taken on an origin sample, if possible.

Below we will report on our results separately for each direction.

5.2.1 Measurements along the a axis

Along the chain axis (a) the DC conductivity of $(TMTSF)_2PF_6$ is rather large ($\sim$ 10^3 $(\Omega\cdot cm)^{-1}$ at room temperature), as it was shown by DC measurements described in Chapter 4. For the microwave measurements along the a axis we have used needles of length of approximately 1 mm. Under this conditions, the skin depth exceeds the half of the sample's principal length along the a direction and the microwave radiation penetrates completely through the sample only if the conductivity has a value less then 0.3 $(\Omega\cdot cm)^{-1}$ at the frequency of 33.5 GHz. As it was shown by the earlier measurements, the microwave conductivity of $(TMTSF)_2PF_6$ along the chain axis is much larger than 0.3 $(\Omega\cdot cm)^{-1}$ and is comparable to the DC conductivity in the order of magnitude [131, 132]. Therefore in the microwave investigations along the a axis we have expected $(TMTSF)_2PF_6$ to be in the skin-depth regime (see Sec. 3.3.1), at least in the normal state. In the skin-depth regime, one performs the analysis in terms of surface resistance R_S and surface reactance X_S, which can be extracted from the change of center frequency and halfwidth, using Eqs. (3.16) and (3.17), respectively. The main problem here is to get rid of the unreproducible frequency shift which is introduced when the cavity is disassembled. It is possible to exclude this additive shift from the center frequency data, if the Hagen-Rubens limit can be applied for some parts of the experimental data (usually, to the temperature region of the higher conductivity). Then, in the range of the Hagen-Rubens limit applicability, the change in center frequency ($\Delta f/f_0$) and the change of the halfwidth ($\Delta\Gamma/2f_0$) can be equalized to each other through the equality of the absolute values of the surface reactance (X_S) and the surface resistance (R_S), respectively (see Eqs. (3.16), (3.17) and (3.26)).

Because we have performed our measurements at microwave frequencies, we expect the Hagen-Rubens limit ($\omega\tau \to 0$) to be appropriate for our analysis, this was also the case in earlier investigations [131, 132]. Indeed, the temperature dependencies of the relative change of the halfwidth $\Delta\Gamma/2f_0 = R_S$ and the center frequency $-\Delta f/f_0 = X_S+C$ have the same profile over the wide temperature range, as depicted in Fig. 5.2,

top panel. This is a strong proof that the (TMTSF)$_2$PF$_6$ system is in the Hagen-Rubens limit along the a-direction at the microwave frequencies, and the surface resistance $R_S = \Delta\Gamma/2f_0$ and the surface reactance $X_S = \Delta f/f_0$ have equal absolute values to within an additive constant C:

$$-R_S = X_S + C. \tag{5.1}$$

Thus the constant C containing in the center frequency data, which is due to the shift of the center frequency upon the disassembling of the cavity for the introducing the sample, can be determined from our analysis if we normalize the surface reactance $X_S = \Delta f/f_0 + C$ data to the surface resistance $R_S = \Delta\Gamma/2f_0$ data, as shown in Fig. 5.2, top panel.

After making this procedure, we have obtained the absolute values of both the change of the center frequency $\Delta f/f_0$ and the halfwidth $\Delta\Gamma/2f_0$ over the whole temperature range, as shown in Fig. 5.2 for two different samples at the top and the bottom panel, respectively, and therefore the self-consistent analysis has been performed in order to obtain the absolute values of the complex conductivity. The same scenario, i.e., the applicability of the Hagen-Rubens limit, was evidenced for all our samples. After excluding the frequency shift C from our data, we were able to perform a self-consistent analysis assuming the system to be either in the skin-depth regime or in the depolarization regime.

To make the analysis assuming the skin-depth regime, we took the absolute values of the surface resistance $R_S = \Delta\Gamma/2f_0$ and the surface reactance $X_S = \Delta f/f_0$ and calculate the conductivity, using the Eq. (3.24) for the general skin-depth regime and Eq. (3.28) for the (probable) Hagen-Rubens limit. The typical calculated values of the microwave conductivity of (TMTSF)$_2$PF$_6$ along the a axis under the assumptions of the skin-depth regime and the Hagen-Rubens limit of it are depicted in Fig. 5.3.

To perform the analysis in the framework of the depolarization regime, we have used Eq. (3.29) and from the known frequency shift $\Delta f/f_0$ and the halfwidth $\Delta\Gamma/2f_0$ we have calculated the conductivity, as shown in Fig. 5.3. As we see from Fig. 5.3, the
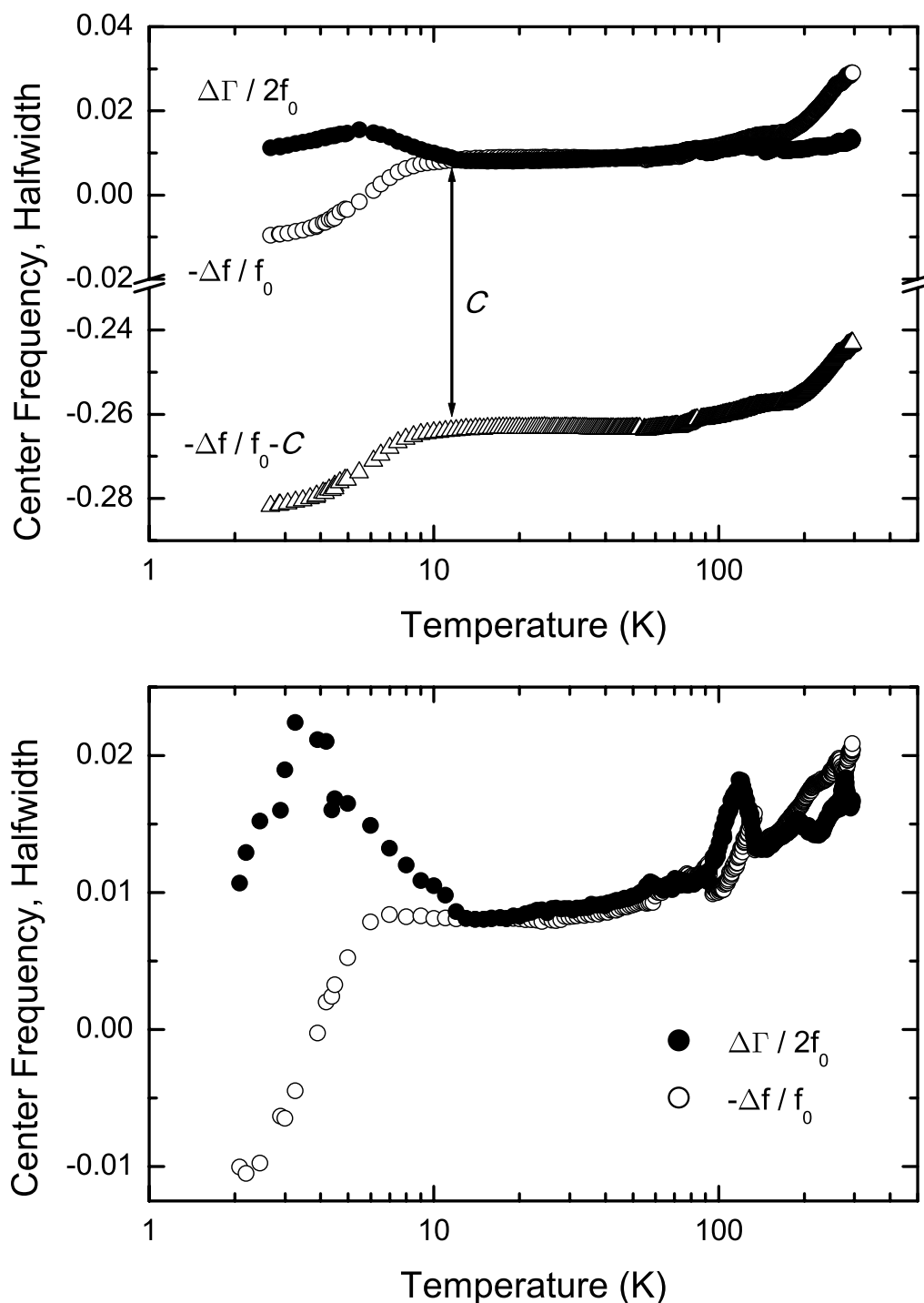
Figure 5.2: The center frequency $-\Delta f/f_0$ and the halfwidth $\Delta\Gamma/2f_0$ temperature profiles (top panel). The profiles scale each other in the broad temperature range 12 K< T <150 K, showing the Hagen-Rubens limit applicability at these temperatures: $R_S = \Delta\Gamma/2f_0 \simeq X_S = -\Delta f/f_0$. (Bottom panel) The Hagen-Rubens limit evidenced from the measurements on another sample.
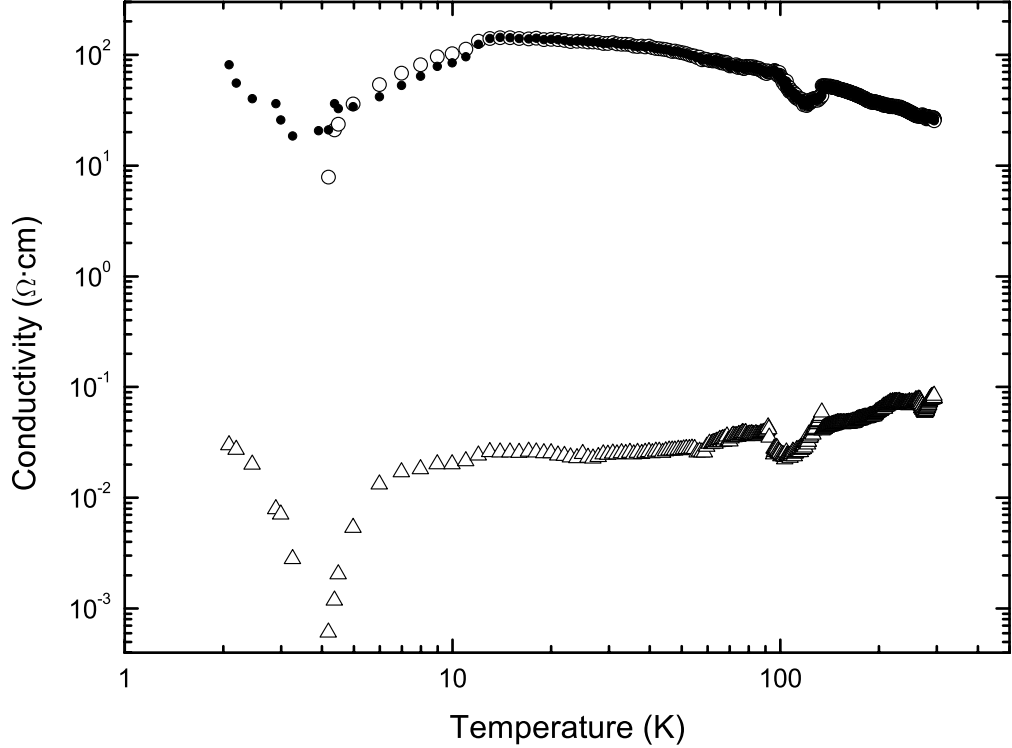
Figure 5.3: The 33.5 GHz conductivity of $(TMTSF)_2PF_6$ along the a axis, as calculated for different regimes: the skin-depth regime (solid circles), the Hagen-Rubens limit (open circles), and the depolarization regime (open triangles).

results obtained under the assumption of the depolarization regime are very conflicting with the DC results (Sec. 4.2) and previous microwave measurements [131, 132] both quantitatively (in the order of magnitude) and qualitatively (the semiconducting behavior in the normal state), and hence we can assume that along the chain axis a the system is in the skin-depth regime both in the normal state (above the temperature 12 K) and in the SDW state (below 12 K). One more argument supporting this assertion we will present below.

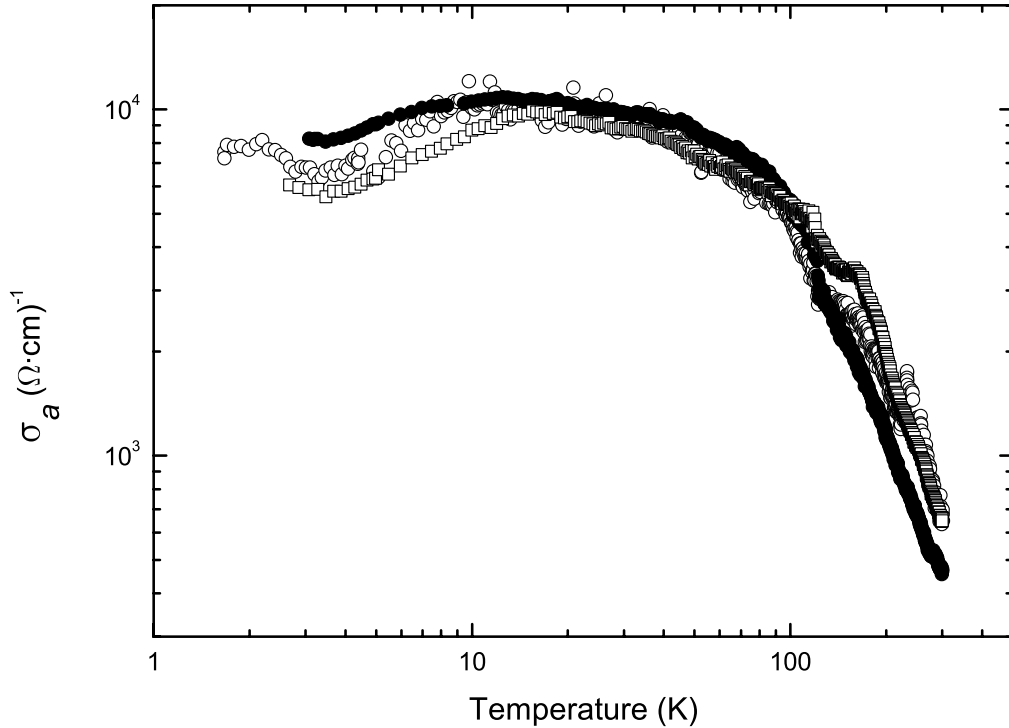The generic plot of the conductivity σ_a *versus* temperature T along the chain axis

Figure 5.4: The 33.5 GHz conductivity of (TMTSF)$_2$PF$_6$ along the chain axis a.

a for several samples of (TMTSF)$_2$PF$_6$ measured at the frequency 33.5 GHz is presented in Fig. 5.4. The values of the conductivity were calculated using the general skin-depth formalism, *not* the Hagen-Rubens limit. Although being not necessary, we have measured our samples with and without the substrate. And in both cases we have obtained the same temperature profiles of the conductivity. This means that the substrate did not affect the results of our measurements, and this finding is very important for our investigations along the c^*-direction, where we utilized mosaics samples attached to the substrate. We also have checked whether the weakly temperature-dependent behavior of the a-axis conductivity in the intermediate temperature range from 100 K down to the SDW transition temperature of 12 K is due

to the limit of the resolution of our experimental setup. In order to test this assumption we have used the samples of considerably different sizes; we have found that this behavior is typical for all our samples under investigation and therefore is an intrinsic property of the samples, rather then the limitation of the dynamic range or the resolution of our experimental setup. The orders of magnitude of the microwave conductivity are in good agreement with our DC results along the *a* crystallographic axis (see Sec. 4.2).

From Fig. 5.4 we see that the *a*-axis conductivity of (TMTSF)$_2$PF$_6$ at the frequency 33.5 GHz in the SDW state is higher than that in the normal state above 80 K, where the system is indeed in the skin-depth regime. Therefore, we were correctly applied the skin-depth analysis for our data below 12 K.

5.2.2   Measurements along the b' axis

For the analysis of our data measured along the b' transverse direction we have used the same arguments as for the *a*-direction. From the DC conductivity measurements we have found that the DC resistivity of (TMTSF)$_2$PF$_6$ along the b' axis is in the order of magnitude of 0.1–1 $\Omega{\cdot}$cm (see Sec. 4.2), which gives us a value of skin depth of 0.1–0.3 mm at 33.5 GHz. For the microwave measurements along the *b* direction we have utilized the needle shaped samples of the length of approximately 1–1.2 mm. This implies that if we would rely on this value of the transverse resistivity as a starting point for our investigations, we should expect the system to be in the skin-depth regime along the b' direction, at least in the normal state. To answer this question, we have performed the self-consistent analysis, in the manner described in the previous Section.

From the the temperature profiles of the center frequency and the halfwidth we found that the Hagen-Rubens limit ($|R_S| = |X_S|$) is valid for our data in a wide temperature range, as shown in Fig. 5.5 for several samples. Therefore, the constant frequency shift was excluded from our center frequency data, and we have performed our analysis both in the framework of the skin-depth regime and the depolarization
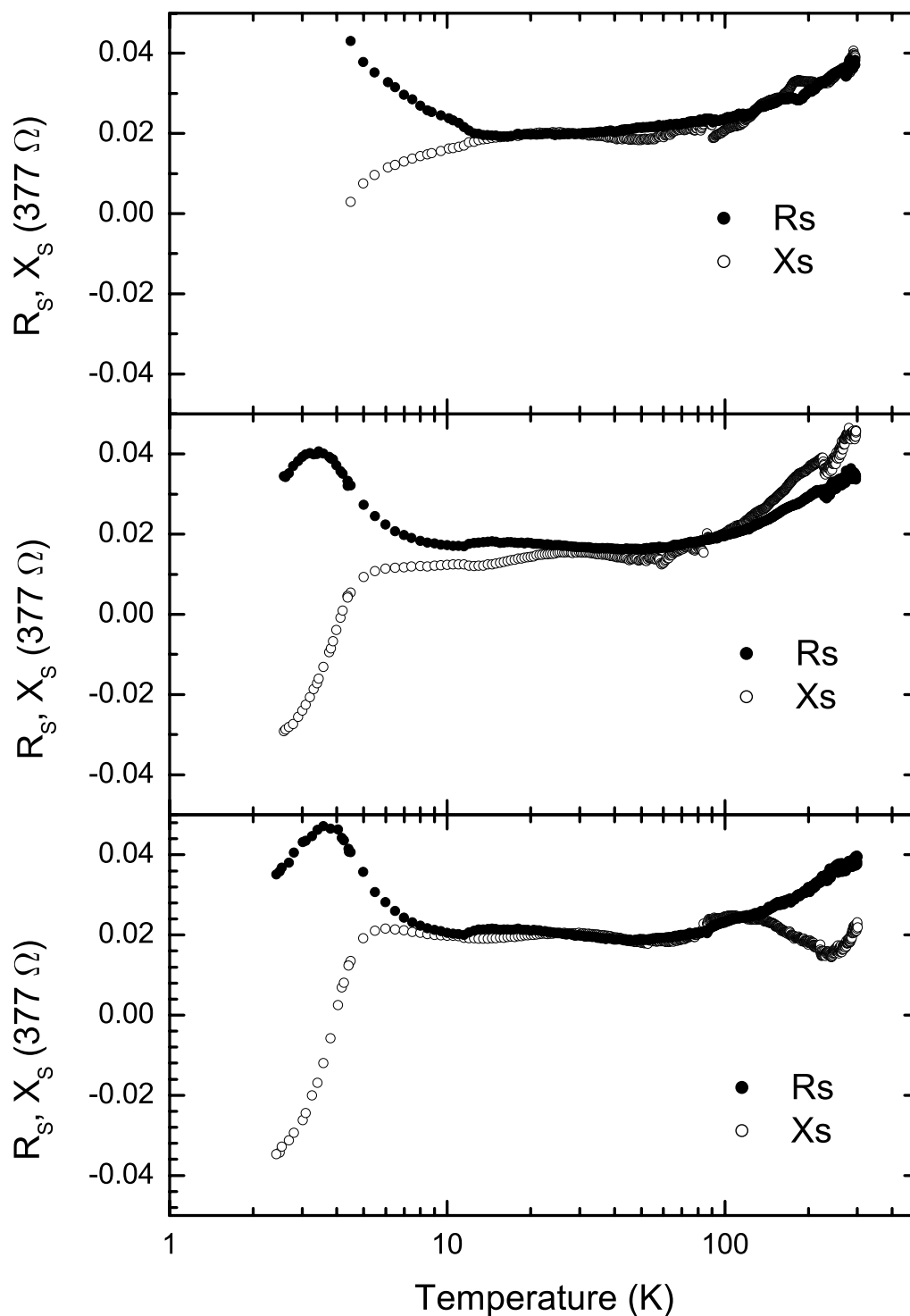
Figure 5.5: The temperature profiles of the surface resistance R_S and the surface reactance X_S measured for three different samples of (TMTSF)₂PF₆ at 33.5 GHz. The validity of the Hagen-Rubens limit ($|R_S| = |X_S|$) is clearly seen in a broad temperature range.

regime, the analysis using these two regimes is displayed in Fig. 5.6 for the same crystals as in Fig. 5.5. From the analysis depicted in Fig. 5.6 we can conclude, that our data can be analyzed using skin-depth formalism almost in the whole temperature range, except for below the temperature $T \simeq 4$ K. There, the conductivity calculated in the framework of the skin-depth regime has nonphysical negative values, at the same time the analysis performed in the framework of the depolarization regime becomes reasonable, since the corresponding curves touch the curves representing the skin-depth regime, making a smooth crossover from one regime to another. The Hagen-Rubens limit cannot be treated as a valid approximation for this low-temperature region, as it clearly seen from Fig. 5.5. Moreover, to present the final values of the b'-axis conductivity of (TMTSF)$_2$PF$_6$ even in the normal state, i.e. above 12 K, we used the general skin-depth formalism, rather then the Hagen-Rubens limit, which is the limiting case of the skin-depth regime. The generic plot of the so-calculated b-axis conductivity of (TMTSF)$_2$PF$_6$ at 33.5 GHz for several samples is presented in Fig. 5.7.

Here we show the results of our measurements on several samples from different crystallization batches. In order to be sure that the measurements along the b' axis were not polluted from the perpendicular direction of the sample due to the slight curvature of the electric field in the electric field antinode (see Fig. 3.1), we have performed our measurements in the configuration when either the a axis or the c^* axis of the sample were parallel to the resonator's axis Z (see the sketch in Fig. 5.7). We also have performed the measurements both with the substrate and without the substrate. All the results, depicted in Fig. 5.7 perfectly coincide with each other, meaning that the substrate does not affect our data, as well as the results of our measurements are independent from the orientation of the sample with respect to the resonator's axis Z.

The behavior of the b'-axis conductivity at 33.5 GHz of the (TMTSF)$_2$PF$_6$ compound we found in current investigations differs from the DC conductivity behavior along this axis. The microwave conductivity profile displays clearly, near 50 K, the
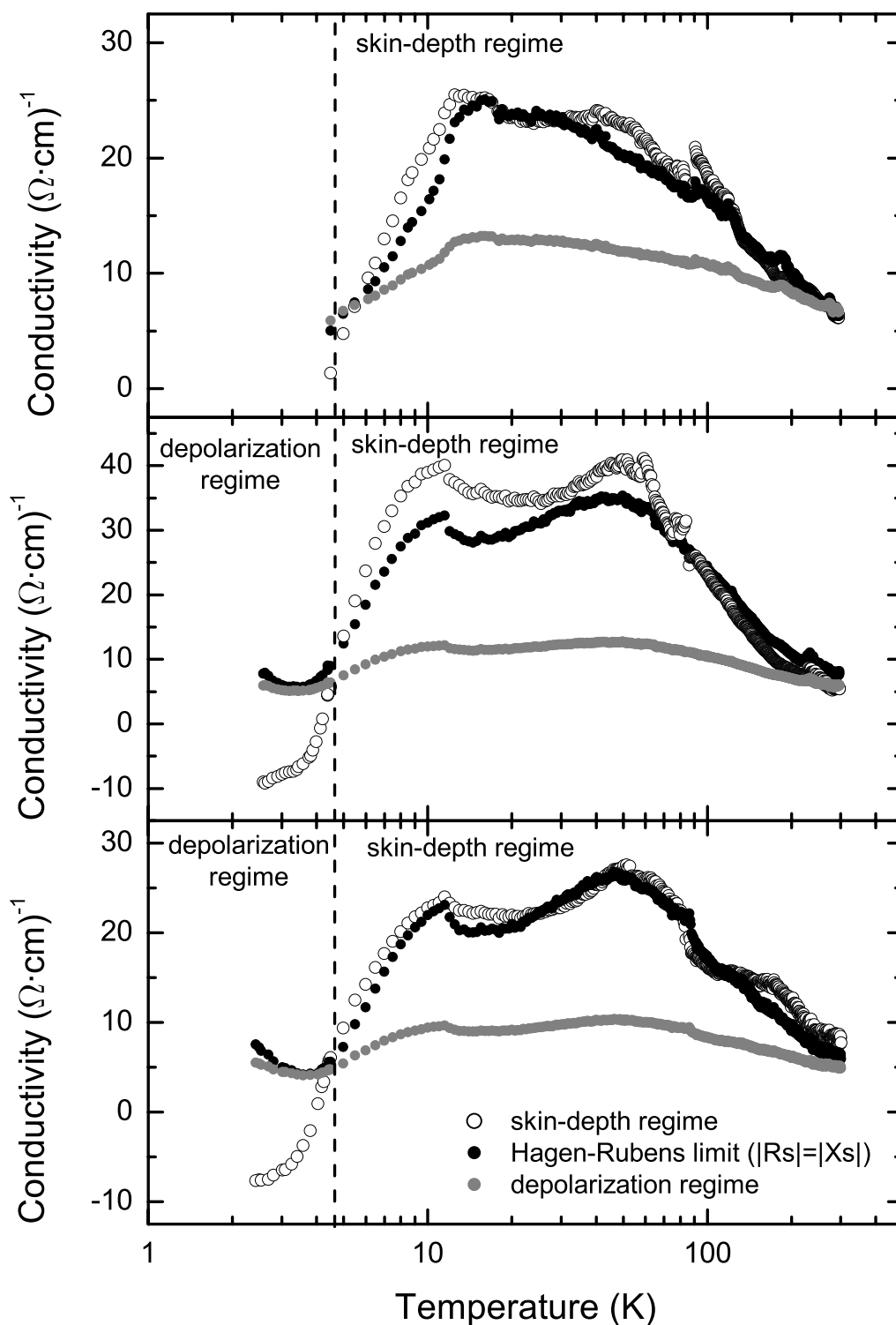
Figure 5.6: The 33.5 GHz conductivity of (TMTSF)$_2$PF$_6$ along the b' direction, as calculated in the skin-depth regime (open circles), the Hagen-Rubens limit (solid circles), and the depolarization regime (gray circles).
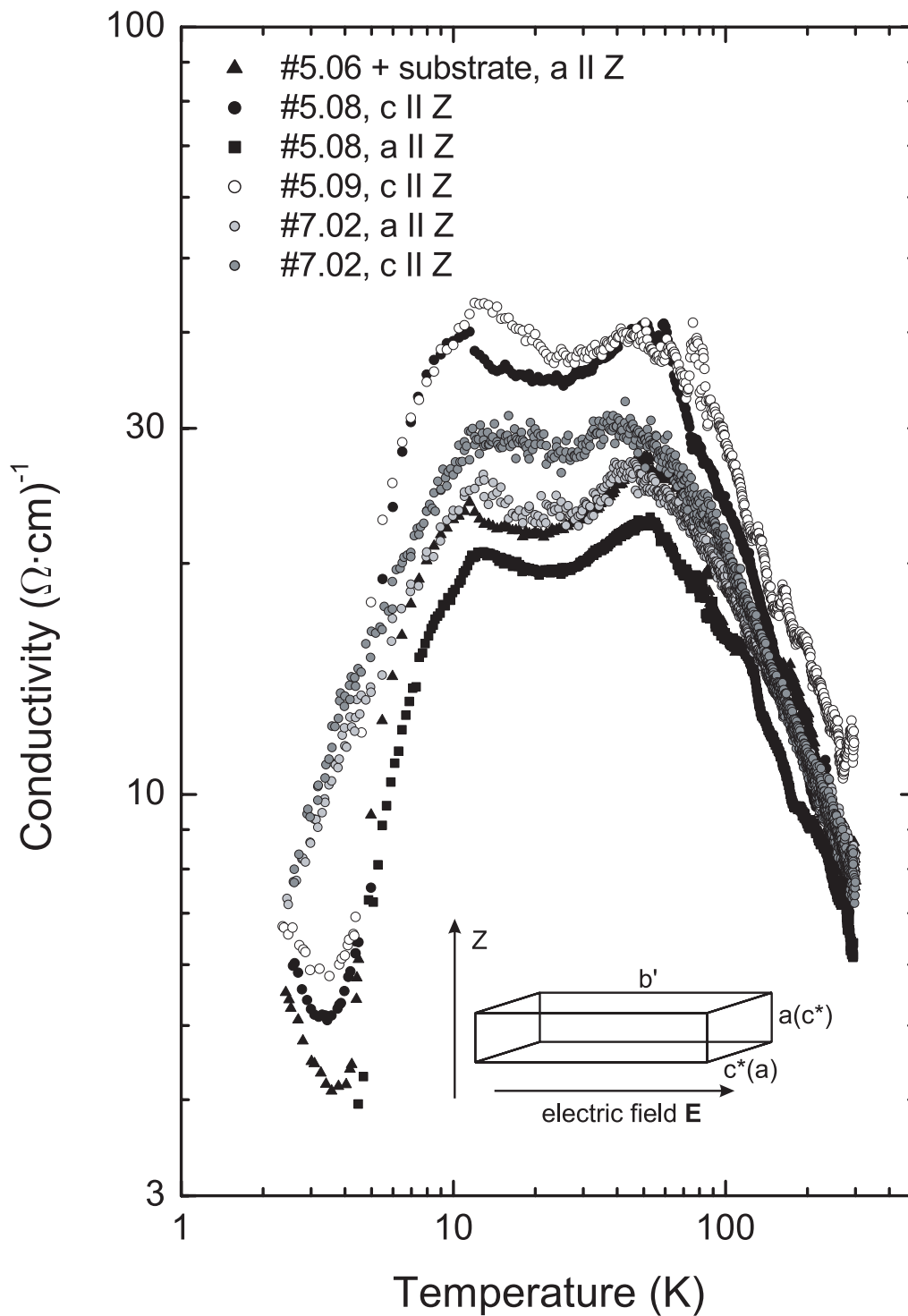
Figure 5.7: The 33.5 GHz conductivity of (TMTSF)$_2$PF$_6$ along the b' crystallographic axis, measured for several samples (labelled with "#" on the plot).

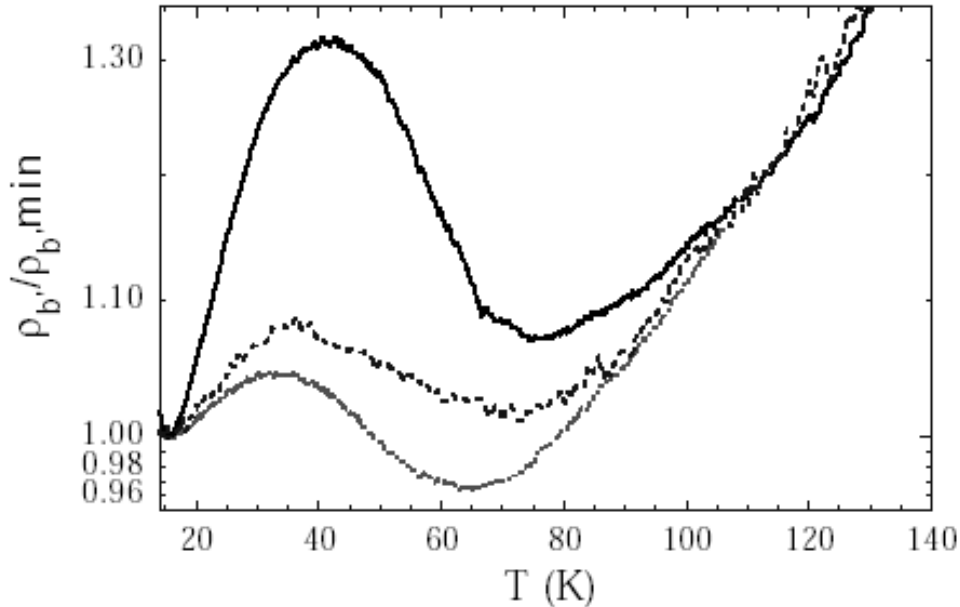Figure 5.8: b'-resistivity profiles relative to the value just above the SDW transition at intermediate temperatures for (TMTFSF)$_2$PF$_6$, as obtained in [133] at 16.5 GHz for three different samples.

change from the metallic behavior to the semiconductor-like behavior. It reaches minimum at around 25 K and becomes metal-like on further cooling down to 12 K, where the SDW transition is evidenced. This unusual behavior generally coincides with the only published results on the microwave conductivity measurements of (TMTSF)$_2$PF$_6$ along the b' direction [133], where the measurements were performed on mosaics in a rectangular copper cavity operated at 16.5 GHz in the TE$_{102}$ transmission mode. The results of [133] are displayed in Fig. 5.8. There was found that on lowering the temperature, the resistivity $\rho_{b'}$ first decreases monotonically down to a local minimum around 75 K, increases slightly to reach a local maximum near 40 K and decreases again down to 15 K before entering the SDW phase below 12 K. This peculiar profile observed between 12 and 80 K was also found to be sample dependent (Fig. 5.8), probably due to the slight misalignment relative to one another of the small crystals used in the needle's construction.

5.2.3   Measurements along the c^* axis

The measurements along the c^*-crystallographic axis were performed on mosaics constructed from the blocks cut out of the grown crystals so, that finally we have obtained a needle-like sample with c^* crystallographic direction as a longest axis of it, as described in Sec. 5.1. The DC value of the resistivity along the c^* axis in (TMTSF)$_2$PF$_6$ found in our experiments (see Sec. 4.2) is around 50 $\Omega\cdot$cm. This value of the conductivity gives us the value of skin depth of about 2 mm at zero frequency, which is larger than the size of the blocks we utilized to build the mosaic needle (with typical length of a block in the corresponding direction of 0.2-0.25 mm) for our investigations. In the microwave region, one even would expect the increase of resistivity, i.e., the decrease of conductivity with respect to the DC values, if one would assume the system to be a metal describing by Drude model [49]. Therefore, we have expected the depolarization regime to be appropriate for the analysis of our data measured along the c^* direction of (TMTSF)$_2$PF$_6$ at 33.5 GHz. Finally, we have found that this was really the case, and a very strong argument supporting this assumption will be presented below.

Unfortunately, applying the depolarization regime, we have the situation, when it is not possible to exclude the constant frequency shift due to the disassembling the cavity for the sample's insertion. Nevertheless, we have collected the statistics on the value of this frequency shift from the previous measurements along the a and the b' directions and we have taken the mean value of the frequency shift of 130 MHz to exclude it from the center frequency data it in the analysis we performed for our investigations along the c^*-axis. Trying to assemble the cavity each time with the same strength, we have achieved the random error only about 10% around this value, meaning that we can be sure within 20% in the magnitude of obtained conductivity values coming out from our analysis using the Eq. (3.29). After applying the depolarization regime, described in Sec. 3.3.2, we have obtained the 33.5 GHz conductivity of (TMTSF)$_2$PF$_6$ along the c^* axis.

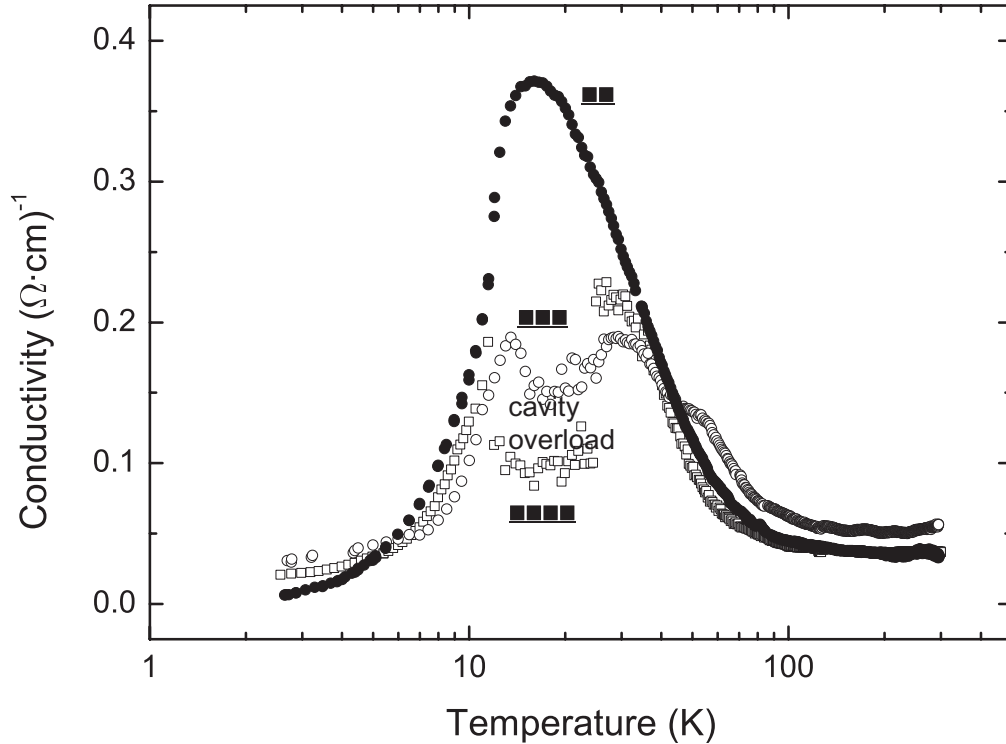The generic plot of the c^*-axis conductivities of (TMTSF)$_2$PF$_6$ measured at

Figure 5.9: The 33.5 GHz conductivity of (TMTSF)$_2$PF$_6$ along the c^* crystallographic axis measured for the four-block mosaics (open squares), for the tree-block mosaics (open circles), and for the two-block mosaics (solid circles).

33.5 GHz is displayed in Fig. 5.9. Here we present the results obtained on the investigations of three mosaic samples. First, we took the sample consisting of four crystal blocks, a needle of about 1 mm long, the corresponding data on the plot are labelled as "■■■■". We found that in the temperature region of 10 K< T <40 K the cavity was overloaded, namely the quality factor of the cavity was below 2000, which is the limit of resolution of our setup. This was also a good proof that the depolarization regime was appropriate in our analysis; because the quality factor of the cavity was decreasing with increasing the conductivity of the sample (because the radiation penetrates completely through the sample and the absorption increases

when the conductivity increases), while in the skin-depth regime the quality factor of the cavity increases with increasing the conductivity of the sample (because the radiation penetrates only within the skin depth, which decreases when the conductivity increases, resulting in lower absorption). The next step was to decrease the number of blocks forming the mosaics down to 3, this data are labelled as "■■■" in Fig. 5.9. We have obtained better results, but the cavity was still overloaded in more narrower temperature region 15 K< T <25 K. Finally, we utilized the mosaics consisting of only two blocks, labelled as "■■" in Fig. 5.9, and obtained the reliable results over the whole temperature range.

All three curves we have obtained from our measurements on three different samples are perfectly coincide with each other in the temperature range, where the cavity was not overloaded. In general, the temperature profile of the c^*-axis conductivity of (TMTSF)$_2$PF$_6$ at 33.5 GHz is in a good agreement with the DC-conductivity data along this direction, except for the the temperature region above 80 K, where the slightly semiconducting behavior was observed in the DC-conductivity results, while the 33.5 GHz conductivity is almost temperature independent in this temperature region.

5.3 Microwave Investigations of (TMTSF)$_2$PF$_6$ at 24 GHz

The microwave investigation of the conductivity of the Bechgaard salt (TMTSF)$_2$PF$_6$ at the frequency of 24 GHz was performed in order to confirm our results obtained at 33.5 GHz, since these two frequencies are not far away from each other, and we did not expect any valuable frequency-dependence of the conductivity results within such a limited frequency domain. The nearness of these two frequencies in terms of electrodynamical geometry for our samples, meaning that the characteristic length scales (skin depth, sample sizes) remain almost the same, also suggests that the analysis described in the previous Section can be applied without changes to the data

obtained at 24 GHz.

After applying the analysis exactly in a way described in the previous Section, we have obtained the 24 GHz conductivity of (TMTSF)$_2$PF$_6$ along three crystallographic axes. The generic plot of microwave conductivity of (TMTSF)$_2$PF$_6$ at the frequency of 24 GHz along the a, b', and c^* axes is presented in Fig. 5.10. The temperature profiles of the conductivity for each direction are perfectly coincide with the results obtained at 33.5 GHz.

5.4 Analysis and Discussion

Below we will discuss our findings separately for the normal state ($T > 12$ K) and the SDW state ($T < 12$ K). In this section we will speak about the results obtained in the measurements at 33.5 GHz and 24 GHz jointly. In Fig. 5.11 de have depicted the selected representative results of our microwave resistivity measurements together with DC values of resistivity of (TMTSF)$_2$PF$_6$, as obtained from our DC measurements (Chapter 4).

5.4.1 Normal State

Along the chain axis (a), the usual metallic behavior of the microwave resistivity is observed down to 14 K, where the microwave resistivity reaches a minimum (Fig. 5.11). Interestingly, the microwave resistivity profile displays clearly, near 70 K, a change of slope, when the DC one shows a single quadratic behavior below 70 K (see Sec. 4.2)

Along the least conducting direction (c^*), the microwave resistivity profile is consistent with the DC curve (Fig. 5.11): it is almost temperature independent when the temperature is decreased from 300 K to 90 K and recovers a metallic behavior on further cooling below 90 K.

The b'-axis microwave resistivity presents definitely a different profile, being almost flat (below 120 K) on the logarithmic scale compared to the other crystal directions. This profile is shown in more details in the inset of Fig. 5.11. On lowering the
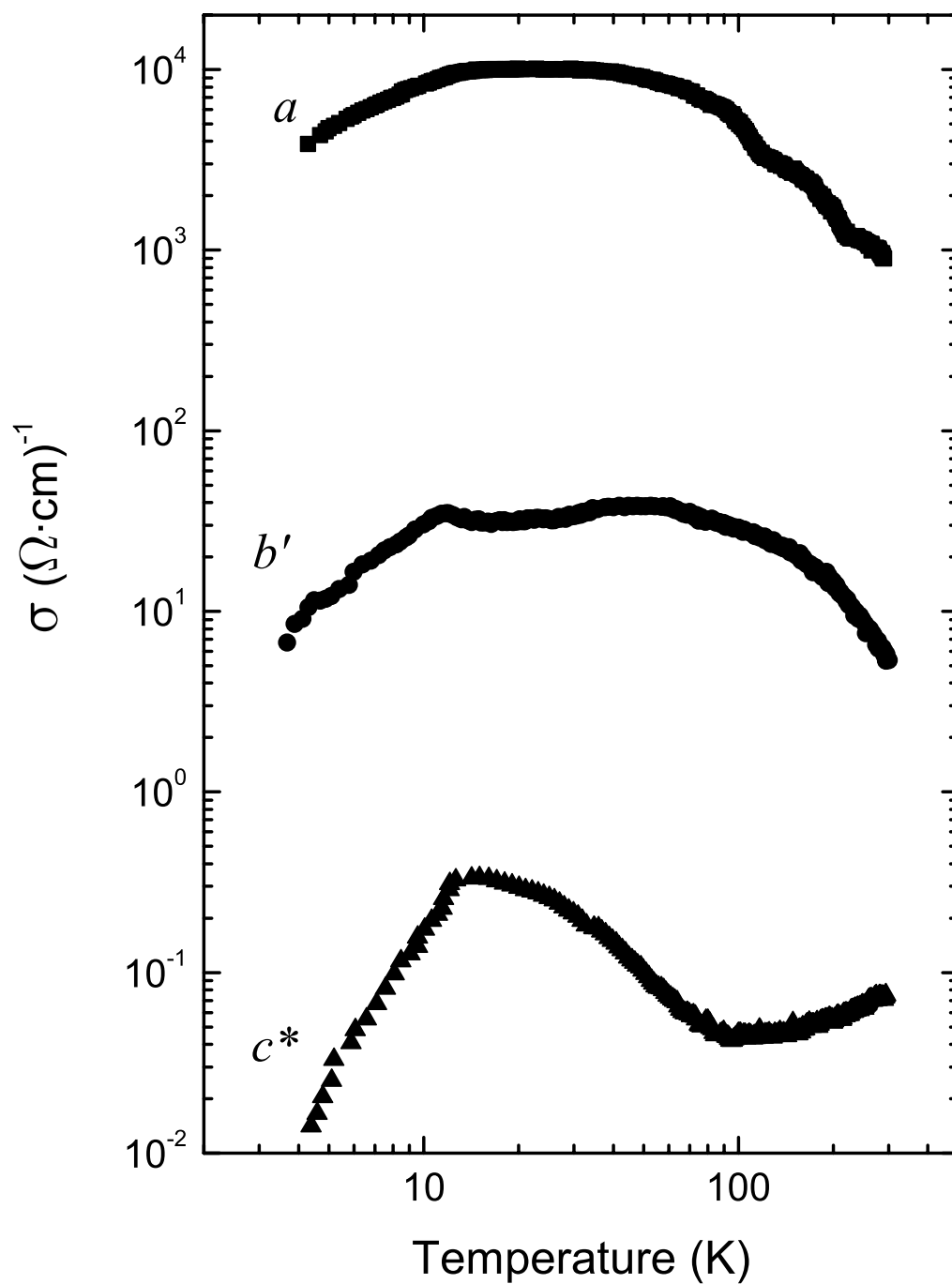
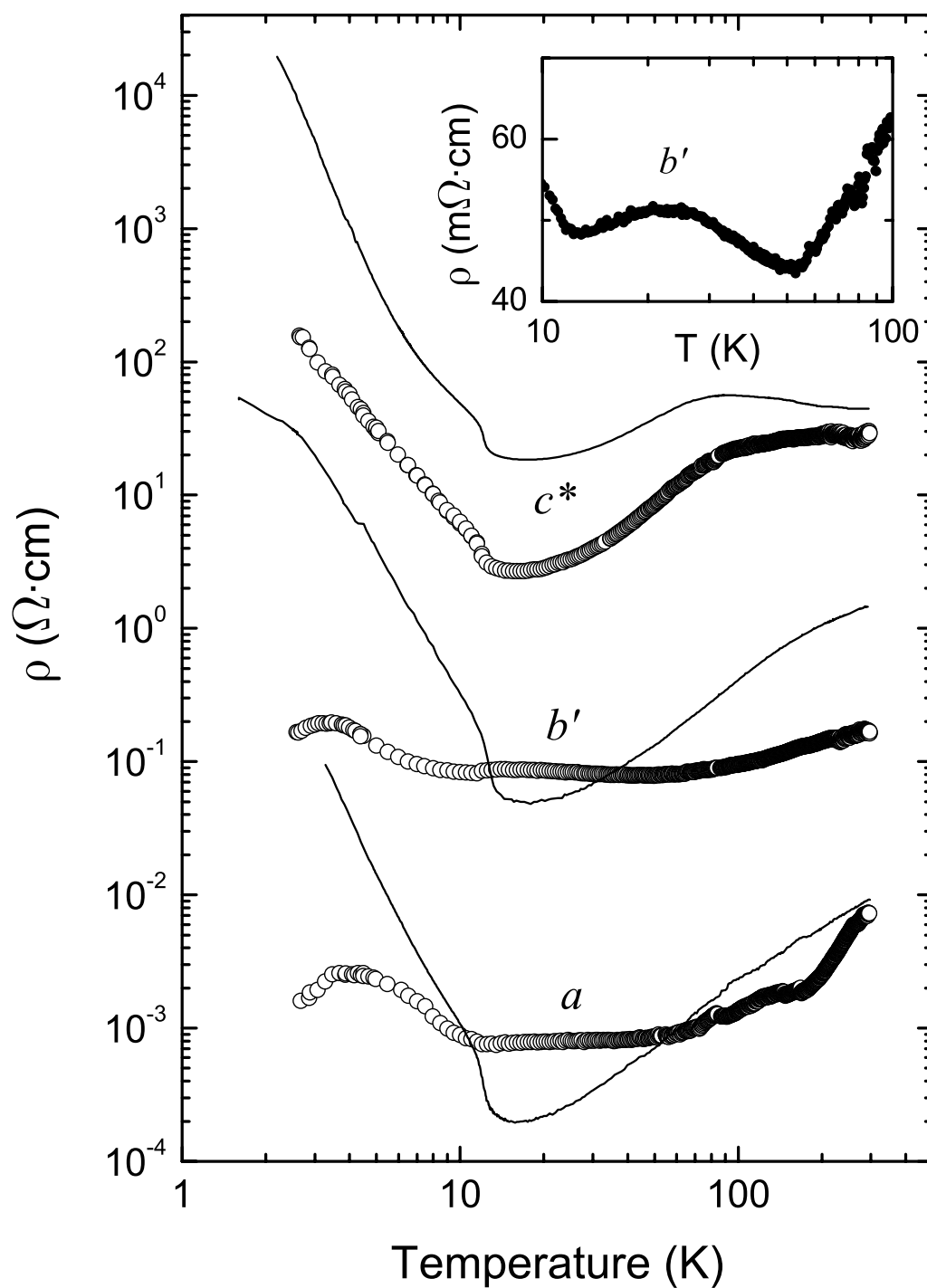Figure 5.10: The 24 GHz conductivity of $(TMTSF)_2PF_6$ along the a, b', and c^* crystallographic axis.

Figure 5.11: The microwave resistivity of (TMTSF)$_2$PF$_6$ along the a, b', and c^* crystallographic axis, measured at 24 and 33.5 GHz (symbols). The corresponding DC resistivity results along each axis displayed by curves. Inset: the b'-axis microwave resistivity shown in the temperature range 10 K$< T <$100 K.

temperature, the microwave resistivity $\rho_{b'}$ first decreases monotonically down to a local minimum around 55 K, increases slightly to reach a local maximum near 25 K and decreases again down to the SDW transition at 12 K.

The emergence of an insulating behavior below 55 K ($\mathrm{d}\rho_{b'}/\mathrm{d}T < 0$ in the inset of Fig. 5.11) refutes the possible existence of quasi-particle states down to 25 K. A Fermi liquid description of interacting electrons above 25 K would, indeed, have required a quadratic temperature profile of both the ρ_a and $\rho_{b'}$ components, as it was discussed in Sec. 4.2. Between 25 K and 55 K, $\rho_{b'}$ is might be better understood by assuming a Luttinger liquid behavior along the stacks: this yields a power-law increase $\rho_{b'}(T) \sim T^{1-2\alpha}$, where α is the exponent of the single-particle density of states of the LL (see Sec. 2.2.3)

In order to describe our microwave data within the framework of the Luttinger liquid theory, we have performed the conversion to the constant-volume quantities similar to that described in Sec. 4.3.1. However, due to the reduced temperature domain used to fit the power law of $\rho_{b'}$, the exponent might be only approximative. In Fig. 5.12 we report the results of this conversion and of finding the appropriate power law descriptions for selected data.

As it was discussed in Sec. 2.2.3, the Luttinger liquid theory gives the following power-law description for the longitudinal and transverse resistivity, respectively:

$$\rho_{\parallel}(T) \sim T^{16K_\rho - 3}, \tag{5.2}$$

$$\rho_{\perp}(T) \sim T^{1-2\alpha}, \tag{5.3}$$

where K_ρ is the exponent characterizing the charge degrees of freedom of a LL and $\alpha = 1/4(K_\rho + 1/K_\rho) - 1/2$ is the Fermi surface exponent.

The comparison of our experimental data depicted in Fig. 5.12, where $\rho_{\perp}(T) = \rho_{b'}(T) \sim T^{-0.4}$ in the temperature range 20 K$< T <$55 K, with the LL theoretical model yields $K_\rho = 0.22$, this value of K_ρ is in a good agreement with the value $K_\rho = 0.23$ for $(TMTSF)_2PF_6$ obtained from the DC transport [109, 86] and optical [105, 58] experiments on $(TMTSF)_2PF_6$ along the chains.
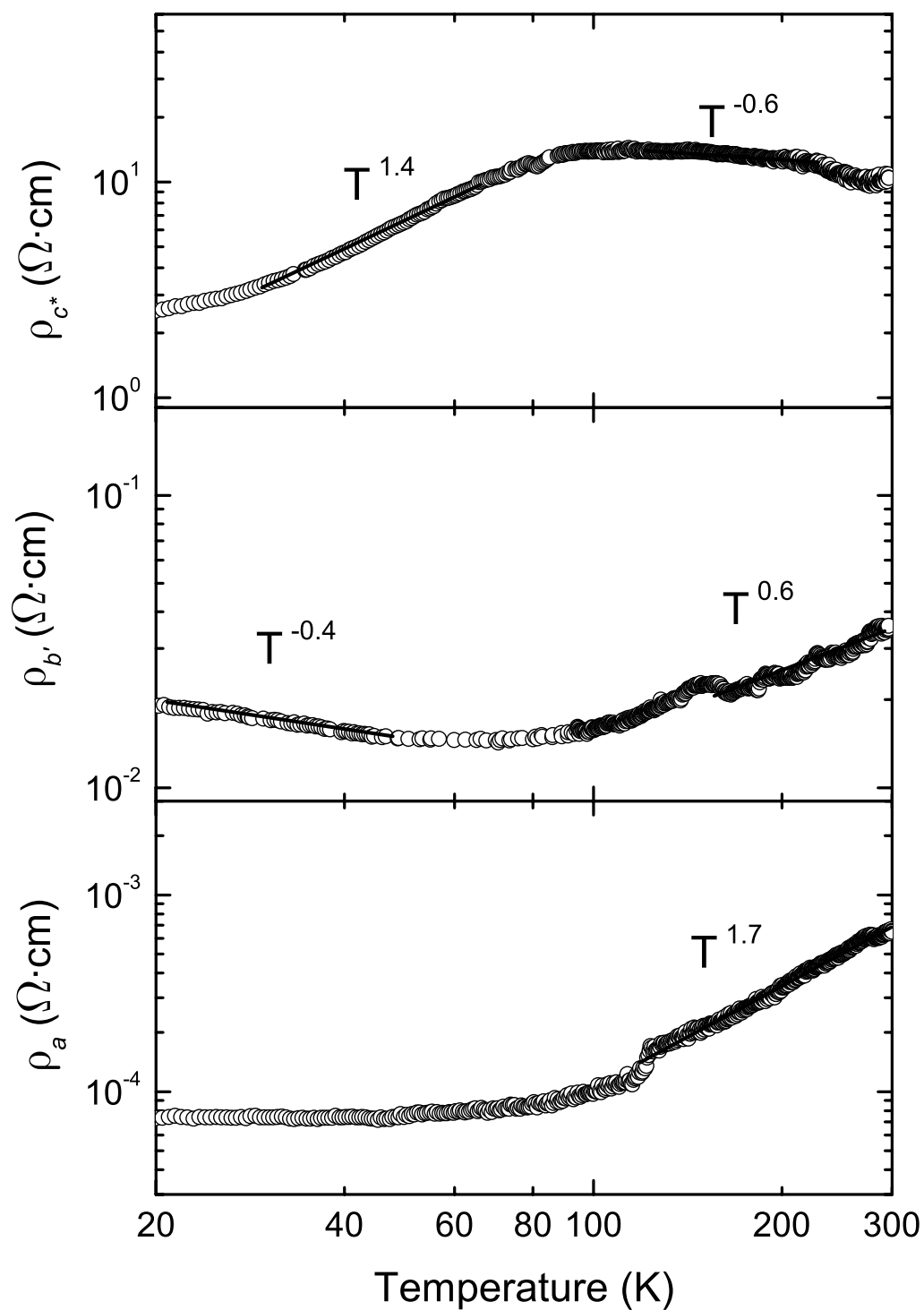
Figure 5.12: The Arrhenius plot of the constant-volume microwave resistivity of (TMTSF)$_2$PF$_6$ along the a (bottom panel), b' (middle panel), and c^* (top panel) crystallographic axis in the normal state.

However, if we use this value $K_\rho = 0.22$ in order to describe the own resistivity data collected along the chain axis a in the same temperature range 20 K$< T <$55 K, an inconsistency arises: with $K_\rho = 0.22$ we would expect for the longitudinal resistivity the power law $\rho_\parallel(T) = \rho_a(T) \sim T^{0.5}$, while our experimental result clearly shows the temperature independent a-axis resistivity in this temperature range (see Fig. 5.12).

Another possibility would be to check whether the high-temperature region 100 K$< T <$200 K could be described by the Luttinger Liquid theory, since the c^*-axis 24 GHz resistivity possess the semiconductor-like behavior $(\mathrm{d}\rho_{c^*}/\mathrm{d}T < 0)$ in this temperature range with the power law $\rho_\perp(T) = \rho_{c^*}(T) \sim T^{-0.6}$. From this power law we obtain $K_\rho = 0.20$, and therefore using this value of K_ρ to calculate the longitudinal resistivity we get $\rho_\parallel(T) = \rho_a(T) \sim T^{0.2}$. The latter power law contradicts our experimental result for the resistivity along the chains in this temperature range: $\rho_a(T) \sim T^{1.7}$. Therefore, we can conclude that for $(\mathrm{TMTSF})_2\mathrm{PF}_6$ our microwave data cannot be completely understood within the LL picture.

5.4.2 SDW State

The spin-density wave transition in $(\mathrm{TMTSF})_2\mathrm{PF}_6$ is evidenced at 12 K along all three directions at microwave frequencies, as seen from Fig. 5.11. It is also seen from Fig. 5.11 that the SDW transition behavior along the a and the b' crystallographic directions is much less activated when compared to the DC data. This reduction of the activation behavior at microwave frequencies was not observed along the c^* direction, where the resistivity profile below 12 K perfectly scales with the correspondent DC results (see Fig. 5.11).

We have performed the quantitative analysis of the microwave resistivity activation behavior in the same manner it was done for the DC results and reported in Sec. 4.3.2. We have compiled the Arrhenius plot of the resistivity ρ *versus* inverse temperature $1/T$ and defined the thermal activation energy values corresponding to the measurements along the different sample directions, as depicted for the selected samples in Fig. 5.13.
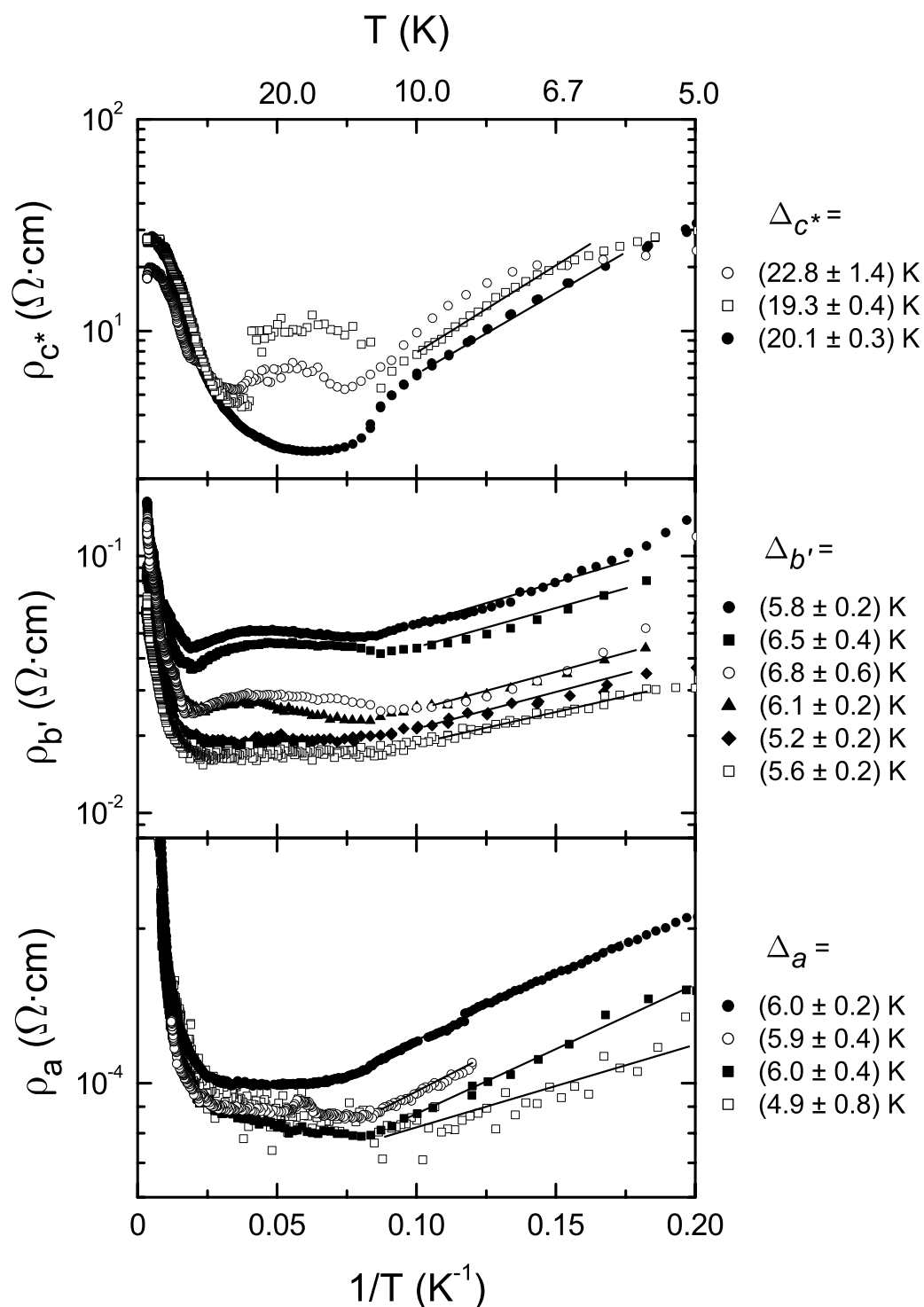
Figure 5.13: The Arrhenius plot of the microwave resistivity of (TMTSF)$_2$PF$_6$ *versus* reversed temperature along the c^* (top panel), the b' (middle panel), and the a (bottom panel) crystallographic axes for different samples. The correspondent thermal activation energy values are displayed at the left to the data plots for each direction.

We have found that along the c^*-axis, the activation behavior of the microwave resistivity within the SDW temperature region, i.e. below 12 K, has the mean value of the activation energy of $\Delta_{c^*} \simeq 20.7$ K. This value of the gap we found from our microwave measurements is in very good agreement with our DC results for the single-particle gap $\Delta_0 = 21$ K (see Sec. 4.3.2).

Along both the a and the b' directions, the reduced values of the activation energy were found: $\Delta_a \approx \Delta_{b'} \approx 6$ K. Such behavior indicates a strongly frequency-dependent response. This value is less than the one we found from the DC measurements and, apparently, the reduction of the gap value is associated with collective mode contribution to the transport properties.

It was proposed that in $(TMTSF)_2PF_6$ the SDW condensate is pinned to the impurities at finite frequencies [132, 49]. The pinned mode is in the microwave frequency range, and its precise position is sample dependent, because it is defined by the impurity content of the samples.

This situation is depicted in Fig. 5.14, which represents the proposed frequency dependence of the conductivity of $(TMTSF)_2PF_6$ in the SDW state. The single particle gap $2\Delta \approx 42$ K is indicated with a solid arrow at 30 cm^{-1}, as obtained from the DC measurements. The pinned mode is indicated in the microwave frequency range with a solid arrow. The dashed arrow depicts the frequency of our experimental technique (0.8 cm^{-1} for 24 GHz and 1 cm^{-1} for 33.5 GHz). It is evident, that our microwave investigations have been performed in the range, where the pinned collective mode is still very well pronounced, i.e., on the shoulder of the pinned mode resonance. The pinned mode is also grows with decreasing the temperature [132].

Therefore we can conclude that performing measurements at the frequencies of 24 and 33.5 GHz we have an appreciable contribution of the collective mode (the pinned SDW mode) to the transport properties of the system, leading to the reduced activation behavior of the resistivity in the SDW ground state. When at zero frequency in the SDW state, the transport is only of single particle nature.

Remarkably, the activation energy values reduce the same way for the a and b'
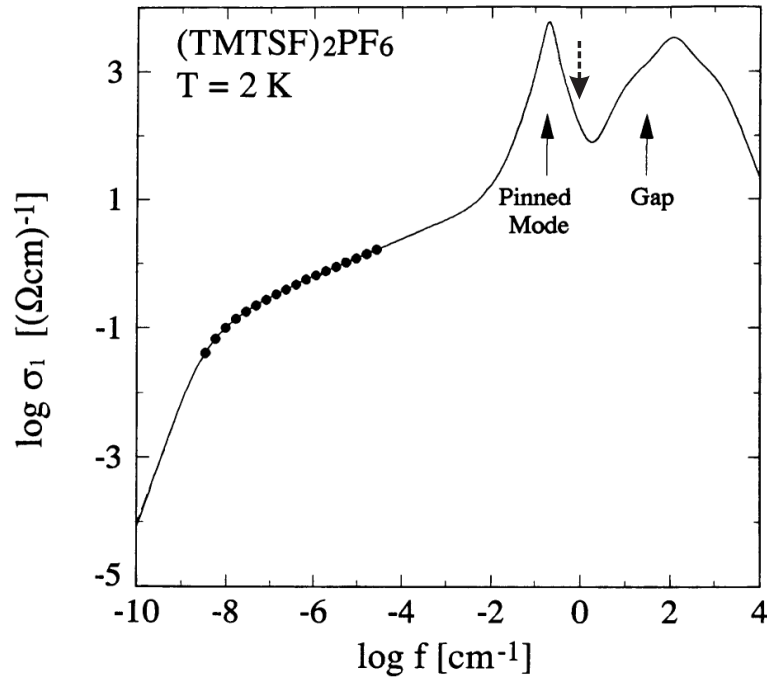
Figure 5.14: The frequency dependent SDW conductivity is displayed, as adopted from [132]. The measured conductivity is shown with symbols, the solid line represents the interpolation with the optical conductivity data and with the microwave conductivity data collected along the chain axis a . The solid arrows depict the position of single particle gap at 30 cm^{-1} and the SDW pinned mode in the microwave frequency range, labelled as "Gap" and "Pinned Mode", respectively. The dashed arrow depicts the frequency domain of the investigations presented in this work.

directions. This behavior was never observed before due to the lack of microwave investigations along the transverse axes of $(TMTSF)_2PF_6$, and the possible interpretation we will present below. As it was discussed in detail in Chapter 1, the Fermi surface of $(TMTSF)_2PF_6$ consists of two warped sheets (see Fig. 1.4, c), and thus the Fermi surface is opened along the k_c axis of the momentum space. We have clearly observed the development of the SDW ground state along the c^* axis in our DC and microwave investigations, meaning that the picture following from the tight-binding model and presented in Chapter 1 is rather simplified. The interchain single-particle

tunnelling along the b' direction is much large than that along the c^* direction, since $t_b \gg t_c$, and leads to a warping of the Fermi surface. At low temperatures, the wave vector $\mathbf{Q} = 2k_F \cdot \hat{a}$ no longer nests this warped Fermi surface, but the nesting is possible in the $a - b'$ plane with a tilted nesting vector $\mathbf{Q} = 2k_F \cdot \hat{a} + \frac{\pi}{b} \cdot \hat{b}$, and this situation is depicted in Fig. 5.15. The tilting of the nesting vector $\mathbf{Q}$ is responsible
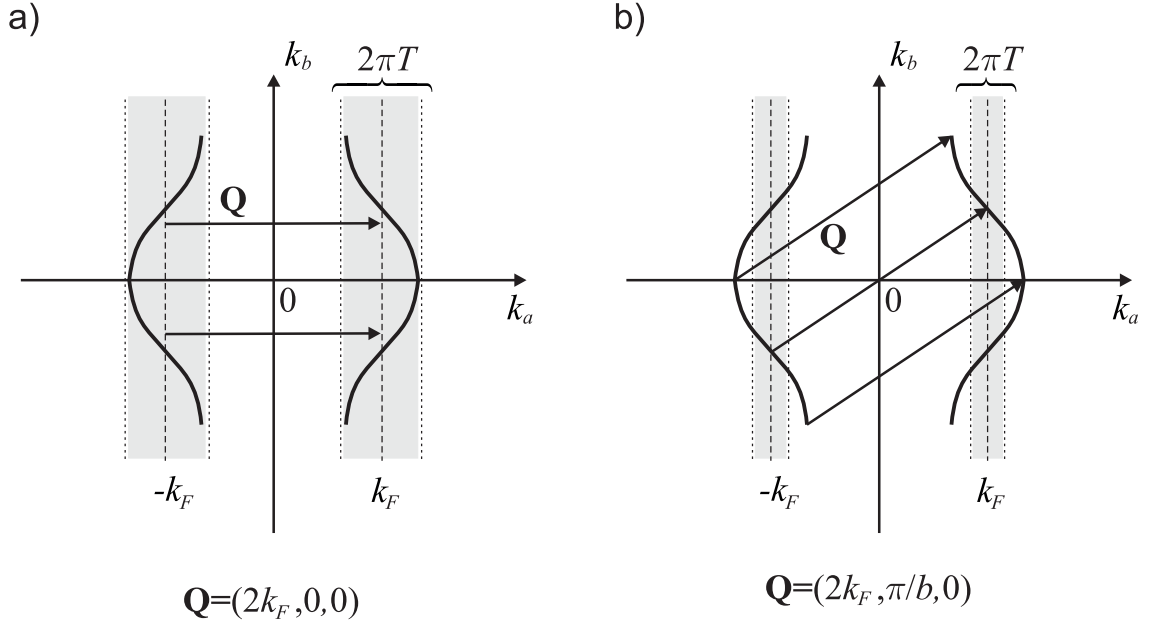

Figure 5.15: The schismatical representation (not to scale) of the nesting of the Fermi surface of $(TMTSF)_2PF_6$. At high temperature (a), the thermal fluctuations hide the warping of the Fermi surface and the conductor has a one-dimensional nesting vector $\mathbf{Q} = 2k_F \cdot \hat{a}$. At low temperature (b), the warping is felt and the nesting vector becomes two-dimensional: $\mathbf{Q} = 2k_F \cdot \hat{a} + \frac{\pi}{b} \cdot \hat{b}$.

for the fact that the SDW formation also takes place along the b' crystallographic axis, as it was evidenced from the microwave experiments. The quantitative similarity in the suppression of the activation behavior along the a and b' axes can also be explained within this picture. The tilting of the nesting vector means that the collective mode transport occurs not only along the a direction, but along the mixed direction in the $a - b'$ plane, having its projection both along a and b'. Therefore, response of the collective mode along these two axes should be qualitatively similar: when the SDW slides, there is an equivalent contribution both in the a and b'-axis

transport. Hence the collective mode contribution to the transport properties of the system below 12 K at the microwave frequencies is equal for the two directions a and b', leading to the equal reduction of the activation behavior for these two direction. To come to these conclusions is only possible by the probe of the transverse properties of the $(TMTSF)_2PF_6$ system at the microwave frequencies, where both the single-particle transport and the collective mode contribution coexist, and this was done in the presented work.

From Fig. 5.13 we see that even for a single sample the found values of the thermal activation energies are rather uncertain, sometimes within 10% error. The possible explanation for this uncertainty is that the precise position of the SDW pinned mode on the frequency scale, and therefore the corresponding value of the thermal activation energy, is define by the impurity content of the samples. Hence, it may be sample-dependent or, at least, it may differ for the samples from different crystallization batches.

The difficulty in more precisely defining the thermal activation energies in the SDW state is also associated with the low-temperature anomalies below 3.5 K. This anomalies is clearly seen in the microwave resistivity data collected at 33.5 GHz along the a and the b' (see, for example, Figs. 5.4 and 5.7) axis and is a subject of discussion, given in the next Section.

5.4.3   Below 3.5 K

Below the temperature of 3.5 K, i.e., deeply in the SDW ground state, the strong deviations from the activated semiconductor-like behavior were observed in the data obtained at 33.5 GHz along the a and the b' crystallographic axes of $(TMTSF)_2PF_6$ (Figs. 5.4, 5.7). These deviations, however, were not observed by DC resistivity measurements (see Sec. 4.3.2) on fresh samples and 24 GHz measurements on annealed samples (Fig. 5.10); we have used the samples at 24 GHz after making the investigations at 33.5 GHz on them. Qualitatively similar anomalies at very low temperatures

from 3 K up to 6 K were evidenced in the previous microwave investigations at different frequencies, and one typical example is depicted in Fig. 5.16. At the same time,
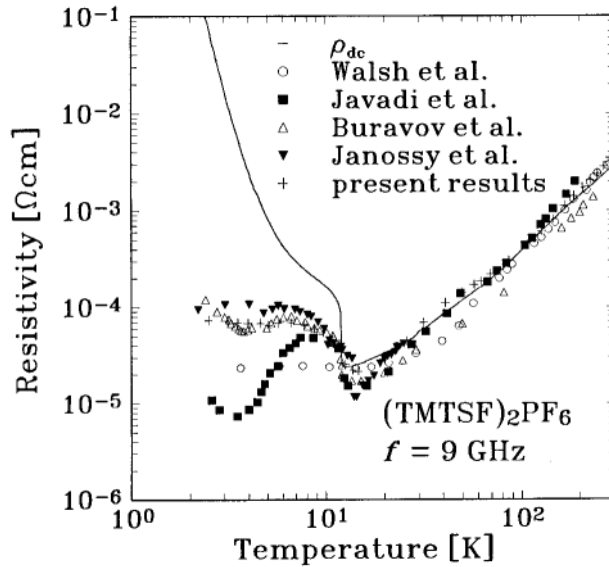

Figure 5.16: The 9 GHz microwave resistivity of $(TMTSF)_2PF_6$ as measured by several groups. The earlier results from Walsh *et al.* [134], Jànossy *et al.* [135], Buravov *et al.* [136], and Javadi *et al.* [137] are compared with the results of [132], labelled as "present results". From Ref. [132].

the earlier DC transport measurements did not show this discrepancies in the SDW ground state [113]. Here we will present a possible explanation of these, still never discussed, anomalies.

In contrast to contact-employed measurements (DC and RF), where the voltage applied to the sample is always strictly determined, the strength of the electric field inside the cavity is hard to control. We have estimated the electric field intensity at the position of the sample (the electric field antinode) inside the cavities in our experimental setups and came to the value of around 1 mV/cm. A more precise determination of the electric field value is difficult to perform due to the large uncertainties in the attenuation of the EM waves in bent waveguides. This value of the electric field is still smaller than the static threshold field value $E_T \simeq 3.5$ mV/cm

for (TMTSF)$_2$PF$_6$ [48] and therefore should not result in sliding of the SDW pinned mode.

Nevertheless it was shown recently that the AC threshold electric field is smaller than the static threshold field and is temperature dependent for the (TMTSF)$_2$PF$_6$ system [138], as presented in Fig. 5.17. It was found, that below 5 K the AC signal amplitude needed to drive the SDW far away from its equilibrium state, i.e., to depin it, strongly decreases (Fig. 5.17). Although these measurements were performed at lower frequencies (up to 1 MHz) compared to our investigations, a simple extrapolation of this findings to the microwave frequency range (see Fig. 5.17, top panel) would result in lower values of the microwave threshold field with respect to the static threshold field values.

These results are quite reasonable from the point of view of wash-board potential model, described in Sec. 2.1.2, because even applying the AC electric field smaller that the wash-board barrier (equal to the static threshold field), a sort of resonance can occur leading the SDW condensate to overcome the barrier height.

We have performed our measurements with the electric field of approximately 1 mV/cm, which is quite close from below to the static threshold field value. Being based on the argument given above, we believe that at low temperatures, below 3.5 K, this value of electric field exceeds the critical dynamic electric field value, leading to the depinning of the SDW mode, at least partially. This is the reason for the suppression of the semiconductor-like activating behavior.

This conclusion is also supported by sample-dependent results below 3.5 K. At 33.5 GHz, these anomalies have slightly different temperature profiles for different samples. The deviations from the semiconductor-like behavior were not observed at all for the samples from another crystallization batch (see Fig. 5.7), and this can be explained by the fact that the pinning strength strongly depends on the impurity content in the samples and therefore can differ for the samples from different crystallization batches. The annealed samples we used for the investigations at 24 GHz have
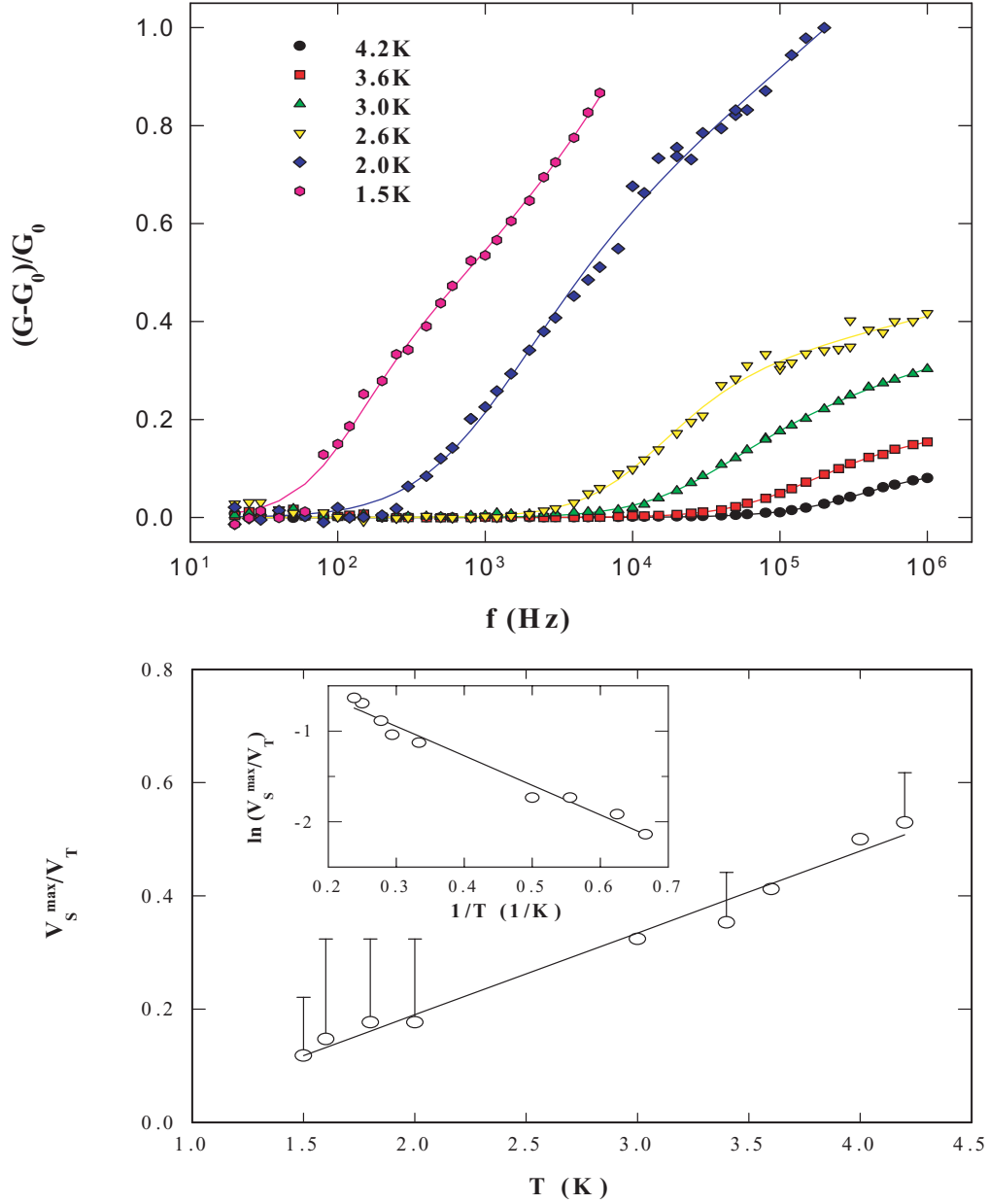
Figure 5.17: (Top panel) Real part of the conductivity in the low AC field regime normalized to the DC value ($(G - G_0)/G_0$) *versus* frequency for several selected temperatures. (Bottom panel) Maximum AC signal amplitude in the low AC filed regime normalized to DC threshold (V^{max}/V_T) *versus* temperature. For $V_S > V_S^{max}$ the sample response starts to deviate from the behavior shown in the top panel. Full line indicates the fit to the power law behavior. The inset shows the fit to Arrhenius form. From Ref. [138].

lost this anomalous behavior below 3.5 K after making cooling cycles during the measurements at 33.5 GHz on them (see Fig. 5.10). Here, on performing a cooling cycle, we inevitably introduce some microckracs to the sample, which also could cause the SDW collective mode to pin more strongly to these imperfections, making the value of threshold field considerably higher.

Chapter 6

Conclusions

6.1 Results

There is a long standing controversy whether the transport properties of the Bechgaard salts can be understood in terms of the usual Fermi-liquid (FL) theory, or the Luttinger liquid (LL) theory. The nature of the metallic phase of an interacting electron system depends strongly on the dimensionality. It is theoretically well established that the conventional FL theory of 3D metals cannot be applied to the interacting electrons whose motion is confined to one dimension, thus leading to a formation of the LL state.

Among all the experimental approaches used to study the dimensionality of the electron gas in Bechgaard salt, transverse transport measurements are particularly relevant to directly probe of interchain coupling. Therefore, the reliable measurements of the transverse transport properties along b' and c^* directions are highly needed, and this was the motivation of the current work.

To explore the low-temperature spin-density (SDW) ground state of $(TMTSF)_2PF_6$ in the microwave range is also of great interest. It was proposed that the modulation of the spin density is slightly incommensurate with the underlying lattice, and the collective mode can slide carrying current. But impurity pinning causes the collective mode to resonate at finite frequencies, the pinned mode resonance

usually occurs in the millimeter wave spectral range in nominally pure specimens, as it was proposed for the SDWs [61]. Upon application of an external electric field, the collective mode can be depinned and carry current. The electrodynamics of the SDW state was well studied at several microwave frequencies (3–100 GHz) along the linear chain axis a [131, 132]. To our knowledge, the microwave transport properties of $(TMTSF)_2PF_6$ in the SDW state were never reported along the transverse directions (b' and c^*).

High quality single crystals of $(TMTSF)_2PF_6$ have been synthesized by the standard electrochemical growth method. The samples have a needle-shaped form with typical dimensions 2 mm $\times$ 0.5 mm $\times$ 0.1 mm along a, b' and c^*- axis, respectively. The results on the b' axis conductivity were obtained on a narrow slice cut from a thick crystal perpendicular to the chain axis (the needle's longest dimension); and the typical dimensions of so-made samples were $a \times b' \times c^* = 0.2 \times 1.3 \times 0.3$ mm^3. The microwave measurements along the c^* axis have been performed on the mosaics.

We present measurements of electrodynamical response of $(TMTSF)_2PF_6$, a representative member of the organic quasi-one dimensional Bechgaard salts, in both the normal ($T > 12$ K) and spin density wave state ($T < 12$ K). We report on the investigations performed along the chain axis a, and transverse crystallographic axes b' and c^*. These measurements have been made at 24 and 33.5 GHz frequency and were anticipated by the direct-current (DC) measurements.

The DC resistivity measurements were performed using a conventional four-probe technique to eliminate influence of the contact resistances. The samples were slowly cooled down to avoid cracks and ensure a good thermal equilibrium with temperature sensors, and the resistivity data were taken in the wide temperature range from 300 K down to 2 K.

The low value of the residual DC resistivity ρ_a together with a high resistivity ratio $\rho_a(300$ K$)/\rho_a(20$ K$)$ indicated a very high crystal quality. Below the $T < 70$ K, we have found, that the resistivity along the a and b' directions follow the quadratic power law: $\rho_a(T), \rho_{b'}(T) \sim T^2$, this behavior is a strong indication of the

inelastic electron-electron scattering and is typical for the Fermi-liquid systems. The quadratic power law in this temperature range 12 K$< T <$70 K was not observed along the c^* direction, but rather $\rho_{c^*}(T) \sim T$. The proportionality $\rho_a(T) \sim \rho_{b'}(T)$ suggests a simple anisotropic band structure with isotropic relaxation time $\tau(T)$; thus the anisotropy $\rho_{b'}/\rho_a \simeq 180$ is temperature independent. The temperature-independent anisotropy together with the small bandwidth also suggests that a tight binding approximation is appropriate. Thus we have found the simple anisotropic band structure: $(4t_a : 4t_b : 4t_c) \approx (1 : 4 \times 10^{-2} : 4 \times 10^{-3})$ eV $=$ (11600 : 460 : 46) K, which is quite close to the anisotropy as determined by band structure calculations [24].

The DC transport properties of (TMTSF)$_2$PF$_6$ in the normal state above $T = 100$ K, where the system is expected to be more one-dimensional, were analyzed in the framework of Luttinger liquid, which gives the following power-law description for the longitudinal ($\rho_\parallel$) and transverse ($\rho_\perp$) resistivity, respectively:

$$\rho_\parallel(T) \sim T^{16K_\rho - 3},$$

$$\rho_\perp(T) \sim T^{1-2\alpha},$$

where K_ρ is the exponent characterizing the charge degrees of freedom of a LL and $\alpha = 1/4(K_\rho + 1/K_\rho) - 1/2$ is the Fermi surface exponent.

As it is known for the Bechgaard salts (TM)$_2$X, much of the temperature dependence of their conductivity at high temperatures arises from the thermal expansion. To analyze the DC conductivity data of (TMTSF)$_2$PF$_6$ within the LL formalism, which was developed for the constant-volume quantities of a strictly 1D system, we have performed the conversion of constant-pressure to constant-volume conductivity data.The pressure coefficients for the conductivity of (TMTSF)$_2$PF$_6$ are known from the literature [30, 88].

From the temperature profiles of the high-temperature DC resistivity in the temperature range 100 K$< T <$300 K, we have found that the comparison of our experimental data, where $\rho_\parallel = \rho_a \sim T^{0.56}$, with the above LL theoretical model yields

$K_\rho = 0.22$, optical experiments on $(TMTSF)_2X$ along the chains [105, 58] yield $K_\rho = 0.23$. However, if we use this value $K_\rho = 0.22$ in order to describe the resistivity data collected along the transverse axes b' or c^* in the same temperature range, an inconsistency arises: with $K_\rho = 0.22$ we would expect for the transverse resistivity the power law $\rho_\perp(T) \sim T^{-0.36}$, while our experimental result clearly shows the $\rho_{b'} \sim T^{0.24}$ and $\rho_{c^*} \sim T^{-0.95}$ temperature dependence. Hence, the strong discrepancy forward the description within the Luttinger liquid picture was evidenced.

At low temperature we have found that the SDW state develops below $T = 12$ K along the a, b', and c^* directions, and the activation behavior was clearly evidenced from the $\log \rho(1/T)$ plot. The value of the thermal activation energy is found to be around $\Delta \simeq 21$ K along all three directions. This value can be perfectly described by a mean-field BCS theory, which gives $\Delta = 1.764 k_B T_C = 21$ K for the transition temperature we observed $T_C = 12$ K.

Unfortunately, since the Bechgaard salts have a pronounced needle shape whose axis is parallel to the chains, transverse transport along b' is particularly difficult to perform with usual DC methods. Owing to non-uniform current distributions between contacts, parasitic contributions from other directions can be introduced. These problems can be avoided by using a contactless microwave technique which allows a better control on the orientation of the current lines in these organic needles.

Measurements of the microwave conductivity were performed by means of the contactless cavity perturbation technique, employing the cylindrical copper cavity operated in the TE_{011} transmission mode at a resonance frequency of 24 and 33.5 GHz. The sample was fixed to a quartz rod positioned in the electric field maximum. We have utilized the needle-shaped samples for the measurements along the a and b' directions and mosaics for the investigations along the c^* crystallographic direction. During a measurement the sample can be rotated inside the cavity, allowing to measure its anisotropy *insitu*. In the experiment we determine the change of the resonance frequency $\left(\frac{\Delta\omega}{\omega_0}\right)$ and the quality factor $\left(\Delta\frac{1}{2Q}\right)$ of the cavity upon insertion of the sample. A complete temperature sweep from 2 K to 300 K is possible with varying cooling

rates and at each desired temperature both the center frequency $f_0 = \frac{\omega_0}{2\pi}$ of the cavity resonance and the halfwidth $\Gamma = \frac{f_0}{Q}$ were measured. Using our apparatus, changes of the frequency and halfwidth can be determined with a sensitivity better then 5×10^{-7} at room temperature, with a further factor of 2 improvement at low temperatures; about 10 mK precision was achieved in temperature control.

The complex conductivity σ the sample is related to the change in the cavity parameters, $\Delta\Gamma$ and Δf_0, and the results were analyzed either within the framework of the quasistatic approximation or surface impedance formalism. The former is applicable when the skin depth exceeds the samples dimensions and microwave radiation penetrates the sample entirely (depolarization regime); the latter corresponds to the opposite case (skin depth regime).

From the self-consistent analysis we were able to find the absolute values of the microwave resistivity along all three directions. We have found that the temperature dependence of the microwave resistivity ρ_a, $\rho_{b'}$, and ρ_{c*} is similar at both microwave frequencies of 24 and 33.5 GHz, but differs from the DC results. Namely, while the microwave resistivity of $(TMTSF)_2PF_6$ along the c^* axis scales with the corresponding DC data, the microwave resistivity ρ_a and $\rho_{b'}$ shows less pronounced temperature dependence both in the normal state and in the SDW state. It was also found that the microwave resistivity $\rho_{b'}$ is not metal-like in the temperature range 25 K$< T <$55 K in the normal state: on lowering the temperature, it first decreases monotonically down to a local minimum around 55 K, increases slightly to reach a local maximum near 25 K and decreases again down to the SDW transition at 12 K. The negative derivative $d\rho_{b'}/dT < 0$ in the temperature range 25 K$< T <$55 K refutes the possible existence of quasi-particle states corresponding to the Fermi-liquid description. In order to describe our microwave data within the framework of the Luttinger liquid theory, we have performed the conversion to the constant-volume resistivity values similar to that described above.

The analysis of our experimental data gives $\rho_\perp(T) = \rho_{b'}(T) \sim T^{-0.4}$ in the temperature range 20 K$< T <$45 K, and within the LL theoretical model yields $K_\rho = 0.22$.

However, if we use this value $K_\rho = 0.22$ in order to describe the own resistivity data collected along the chain axis a in the same temperature range 20 K$< T <$55 K, an inconsistency arises: with $K_\rho = 0.22$ we would expect for the longitudinal resistivity the power law $\rho_\parallel(T) = \rho_a(T) \sim T^{0.5}$, while our experimental result clearly shows the temperature independent a-axis resistivity in this temperature range. Therefore, we can conclude that for $(TMTSF)_2PF_6$ our microwave data cannot be completely understood within the LL picture.

The spin-density wave transition in $(TMTSF)_2PF_6$ is evidenced at 12 K along all three directions. From the Arrhenius plot $\log \rho(1/T)$ we have found that along the c^*-axis, the activation behavior of the microwave resistivity within the SDW temperature region has the mean value of the activation energy of $\Delta_{c^*} \simeq 20.7$ K. This value of the gap we found from our microwave measurements is in very good agreement with our DC results for the single-particle gap $\Delta_0 = 21$ K. Along both the a and the b' directions, the reduced values of the activation energy were found: $\Delta_a \approx \Delta_{b'} \approx 6$ K. Such behavior is indicative of a strongly frequency-dependent response and was attributed to the vicinity of the SDW pinned mode in the microwave frequency range. It was proposed that in $(TMTSF)_2PF_6$ the SDW condensate is pinned to the impurities in the microwave frequency range. We have concluded that our microwave investigations have been performed in the range, where the pinned collective mode is still very well pronounced, i.e., on the shoulder of the pinned mode resonance. Therefore we can conclude that performing measurements at the frequencies of 24 and 33.5 GHz we have a valuable contribution of the collective mode (the pinned SDW mode) to the transport properties of the system, leading to the reduced activation behavior of the resistivity in the SDW ground state. We have considered the two-dimensional nesting vector in $a - b'$ plane, which leads to the similar response of the SDW along a and b' axis, and therefore the activation behavior reduces the same way for these directions. When at zero frequency in the SDW state, the transport is only of single particle nature.

The low-temperature anomalies, below $T < 3.5$ K, were evidenced deeply in the

SDW state at 33.5 GHz, and we believe that these anomalies are due to the exceeding of the threshold electric field when performing the microwave measurements.

6.2 Future Work

While our results strongly point forward the conventional FL theory to be applicable in the normal state of the $(TMTSF)_2PF_6$ system, there are several open questions which remain. There are still several representatives of the Bechgaard salts, which have more pronounced one-dimensionality, e.g. $(TMTSF)_2ClO_4$ or $(TMSTF)_2ReO_4$. They may be a good subject of contactless microwave investigations to successfully apply the LL theory.

In addition, extending the technique described in this thesis to other microwave frequencies to study these representatives of the Bechgaard salts, one can supplement phase diagram and the frequency-dependent picture proposed for $(TM)_2X$ salts in the normal and SDW states.

Finally, the dynamical properties of the SDW mode in $(TMTSF)_2PF_6$ are of interest and could be scrutinized with respect to the applied electric field below 4 K.

Bibliography

[1] P. Ball, *"Designing the Molecular World: Chemistry at the Frontier"*, Princeton University Press, Princeton (1994)

[2] R. E. Peierls, *Quantum Theory of Solids*, Oxford University Press, London (1955)

[3] C. K. Chiang, C. R. Fincher, Jr., Y. W. Park, A. J. Heeger, H. Shirakawa, E. J. Louis, S. C. Gau, and A. G. MacDiarmid, *Phys. Rev. Lett.* **39**, 1098 (1977)

[4] S. A. Brazovski, N. N. Kirova, *"Electron selflocalization and periodic superstructure in quasi one-dimensional dielectrics"* in *Sov. Scient. Reviews, Sec. A. Physical Review* **5**, p.100, ed. by I. M. Khalatnikov (1984)

[5] W. A. Little, *Phys. Rev.* A**134**, 1416 (1964)

[6] D. S. Acker, R. J. Harder, W. R. Hertler, W. Mabiler, L. R. Melby, R. E. Benson and W. E. Mochel, *J. Am. Chem. Soc.* **82**, 6408 (1960)

[7] F. Wudl, G. M. Smith and E. J. Hufnagel, *Chem. Commun.* **13**, 1453 (1970)

[8] J. Ferraris, D. O. Cowan, V. J. Walatka and J. H. Perlstein, *J. Am. Chem. Soc.* **95**, 948 (1973)

[9] J. P. Pouget, S. K. Khanna, F. Denoyer, R. Comés, A. F. Garito and A. J. Heeger, *Phys. Rev. Lett.* **37**, 437 (1976)

[10] S. Kogoshima, T. Ishiguro and H. Anzai, *J. Phys. Soc. Japan* **41**, 2061 (1976)

[11] R. L. Greene and G. B. Street, *Phys. Rev. Lett.* **34**, 577 (1975)

[12] D. Jérome, A. Mazaud, M. Ribault, and K. Bechgaard, *J. Physique Lett.* A**41**, L95 (1980)

[13] K. Bechgaard, C. S. Jacobsen, K. Mortensen, H. J. Pedersen, and N. Thorup, *Solid State Commun.* **33**, 1119-1125 (1980)

[14] N. Thorup, G. Rindorf, H. Soling and K. Bechgaard, *Acta Cryst.* **B 37**, 1236 (1981)

[15] F. Wudl, *J. Am. Chem. Soc.* **103**, 7064 (1981)

[16] K. Bechgaard, *Mol. Cryst. Liq. Cryst.* **79**, 1 (1982)

[17] N. Thorup, G. Rindorf, H. Soling, I. Johannsen, K. Mortensen, and K. Bechgaard, *J. Phys. (Paris) Colloq.* **C3**, 1017 (1983)

[18] B. Gallois, J. Gaultier, C. Hauw, D. Chasseau, A. Meresse, A. Filhol, and K. Bechgaard, *Mol. Cryst. Liq. Cryst.* **119**, 225 (1985)

[19] D. Jérome, and H. J. Schulz, *Adv. Phys.* **31**, 299-400 (1982)

[20] R. Moret, J. P. Pouget, R. Comes, and K. Bechgaard, *Phys. Rev. Lett.* **49**, 1008 (1982)

[21] P. C. W. Leung, A. J. Schultz, H. H. Wang, T. J. Emge, G. A. Ball, D. D. Cox, and J. M. Williams, *Phys. Rev.* B **30**, 1615 (1984)

[22] J. S. Scott, E. M. Engler, W. G. Clark, C. Murayama, K. Bechgaard, and H. J. Pedersen, *Mol. Cryst. Liq. Cryst.* **79**, 417 (1982)

[23] P. M. Grant, *Phys. Rev.* B **26**, 6888 (1982)

[24] P. M. Grant, *J. Phys. (Paris) Colloq.* **C3**, 847 (1983)

[25] D. Jérome, *Strongly Interacting Fermions and High T_C Superconductivity*, B. Doucot and J. Zinn-Justin, Les Houches (1991)

[26] G. Grüner, *Density Waves in Solids*, Addison-Wesley Publishing Company, New York (1994)

[27] G. Soda, D. Jérome, M. Weger, J. Alizon, J. Gallice, H. Robert, J. M. Fabre, and L. Giral, *J. Phys. (Paris)* **38**, 931 (1977)

[28] A. Heeger, in *Highly Conducting One Dimensional Solids*, edited by I. Devreese, p.79, Plenum, New York and London (1979)

[29] J. Moser, M. Gabay, P. Auban-Senzier, D. Jérome, K. Bechgaard, and J. M. Fabre, *Eur. Phys. J.* B **1**, 39 (1998)

[30] D. Jérome, in *Organic Conductors*, ed. by J. P. Farges, Marcel Dekker, New York (1994), p. 405

[31] T. Ishiguro, K. Yamaji, and G. Saito, *Organic Superconductors*, Second Edition, Springer-Verlag, Berlin (1998)

[32] J. P. Pouget and S. Ravy, *J. Phys. I (France)* **6**, 1501 (1996)

[33] J. P. Pouget, in *Low-Dimensional Conductors and Superconductors*, ed. by D. Jérome and L. G. Caron, *NATO ASI Ser. B, Physics* **155**, Plenum Press, New York (1987), p. 17

[34] L. Balicas, K. Behnia, W. Kang, E. Canadell, P. Auban-Senzer, D. Jérome, M. Ribault, and J. M. Fabre *J. Phys. I (France)* **4**, 1539 (1994)

[35] W. Kang, S. T. Hannahs, and P. M. Chaikin *Phys. Rev. Lett.* **70**, 3091 (1993)

[36] R. E. Peierls, *Ann. Phys. Leipzig* **4**, 121 (1930)

[37] H. Fröhlich, *Proc. Royal Soc.* A **223**, 296 (1954)

[38] R. M. Fleming and C. G. Grimes, *Phys. Rev. Lett.* **42**, 1423 (1979)

[39] G. Grüner, A. Zawadowski, and P. M. Chaikin, *Phys. Rev. Lett.* **46**, 511 (1981)

[40] H. Fukuyama and P. A. Lee, *Phys. Rev.* B **17**, 535 (1978)

[41] P. A. Lee and T. M. Rice, *Phys. Rev.* B **19**, 3970 (1979)

[42] E. Sweetland, C-Y. Tsai, B. A. Wintner, J. D. Brock, and R. E. Thorne, *Phys. Rev. Lett.* **65**, 3165 (1990)

[43] S. M. DeLand, G. Mozurkevich, and L. D. Chapman, *Phys. Rev. Lett.* **66**, 2026 (1991)

[44] J. McCarten, M. Maher, T. L. Adelman, and R. E. Thorne, *Phys. Rev. Lett.* **63**, 2841 (1989)

[45] G. Mihály and P. Canfield, *Phys. Rev. Lett.* **64**, 459 (1990)

[46] A. W. Overhauser, *Phys. Rev. Lett.* **4**, 462 (1960)

[47] A. W. Overhauser, *Phys. Rev.* **128**, 1437 (1962)

[48] M. E. Hanson, *PhD Thesis*, University of California, Los Angeles (1994)

[49] M. Dressel and G. Grüner, *Electrodynamics of Solids*, Cambridge University Press, Cambridge (2002)

[50] J. Bardeen, L. N. Cooper, and J. R. Schriffer, *Phys. Rev.* **106**, 162, (1957)

[51] J. Bardeen, L. N. Cooper, and J. R. Schriffer, *Phys. Rev.* **108**, 1175, (1957)

[52] H. Frohlich, *Phys. Rev.* **79**, 845 (1950)

[53] C. A. Reynolds, B. Serin, W. H. Wright, and L. B. Nesbitt, *Phys. Rev.* **78**, 487 (1950)

[54] P. Segovia, D. Purdie, M. Hengsberger, and Y. Baer, *Nature* **402**, 504 (1999)

[55] M. Dressel, P. Hesse, S. Kirchner, G. Untereiner, M. Dumm, J. Hemberger, A. Loidl, and L. Montgomery, *Synth. Met.* **120**, 719 (2001)

[56] T. Lorentz, M. Hofmann, M. Grüninger, A. Freimuth, G. S. Uhrig, M. Dumm, and M. Dressel, *Nature* **418**, 614 (2002)

[57] T. Giamarchi, Phys. Rev B 44, 2905 (1991)

[58] A. Schwartz, M. Dressel, G. Grüner, V. Vescoli, L. Degiorgi, and T. Giamarchi, *Phys. Rev.* B **58**, 1261 (1998)

[59] V. J. Emery, in *Low-Dimensional Conductors and Superconductors*, edited by D. Jérome and L. Caron, Plenum, New-York, p. 143 (1987)

[60] R. L. Greene and E. M. Engler, *Phys. Rev. Lett.* **45**, 1587 (1980)

[61] G. Grüner, *Rev. Mod. Phys.* **66**, 1 (1994)

[62] J. P. Pouget, R. Moret, R. Comes, and K. Bechgaard, *J. Phys. (Paris) Lett.* **42**, L543 (1981)

[63] J. P. Pouget, R. Moret, R. Comes, K. Bechgaard, J. M. Fabre, and L. Giral, *Mol. Cryst. Liq. Cryst.* **79**, 129 (1982)

[64] C. Coulon, in *Organic and Inorganic Low-Dimensional Crystalline Materials*, edited by P. Delhaes and M. Drillon, Plenum, New York, p. 201 (1987)

[65] L. D. Landau, *Sov. Phys. JETP* **3**, 920 (1956)

[66] F. D. M. Haldane, *J. Phys.* C **14**, 2585 (1981)

[67] H. J. Schulz, *Int. J. Mod. Phys.* **5**, 57 (1991)

[68] J. Voit, *Rep. Prog. Phys.* **58**, 977 (1995)

[69] P. W. Anderson, *Phys. Rev. Lett.* **65**, 2306 (1990)

[70] P. W. Anderson, *Phys. Rev. Lett.* **64**, 1839 (1990)

[71] H. Basista, D. A. Bonn, T. Timusk, J. Voit, D. Jérome and K. Bechgaard, *Phys. Rev.* B **42**, 4088 (1990)

[72] C. G. Olson, R. Liu, D. W. Lynch, R. S. List, A. J. Arko, B. W. Veal, Y. C. Chang, P. Z. Jiang and A. P. Paulikas, *Phys. Rev.* B **42**, 381 (1990)

[73] D. Coffey and K. S. Bedell, *Phys. Rev. Lett.* **71**, 1043 (1993)

[74] J. R. Engelbrecht and M. Randeira *Phys. Rev. Lett.* **65**, 1032 (1990)

[75] C. M. Varma, P. B. Littlewood, S. Schmitt-Rink, E. Abrahams and A. E. Ruckenstein, *Phys. Rev. Lett.* **63**, 1996 (1989)

[76] N. Mitani, and S. Kurihara *Physica* C **192**, 230 (1992)

[77] A. Wirosztek, B. Dóra and K. Maki, *Europhys. Lett.* **47**, 358 (1999)

[78] C. Bourbonnais, F. Creuzet, D. Jérome, K. Bechgaard and A. Moradpour, *J. Rev. Lett. (Paris)* **45**, L755 (1984)

[79] P. Wzietek, F. Creuzet, C. Boubonnais, D. Jérome, K. Bechgaard and P. Batail, *J. Phys.* I **3**, 171 (1993)

[80] B. Dardel, D. Malterre, M. Grioni, P. Weibel, Y. Bear, J. Voit and D. Jérome, *Europhys. Lett.* **24**, 687 (1993)

[81] F. Zwick, S. Brown, G. Margaritodo, C. Merlic, M. Onellion, J. Voit and M. Grioni, *Phys. Rev. Lett.* **79**, 3982 (1997)

[82] J. Voit, *Eur. Phys. J.* B **5**, 505 (1998)

[83] J. Voit, *Phys. Rev.* B **47**, 6740 (1993)

[84] V. Meden and K. Schönhammer, *Phys. Rev.* **46**, 15752 (1992)

[85] D. Jérome in Les Houches 1991, *Strongly Interacting Fermions and High T_C Superconductivity* ed. by B. Douçot and J. Zinn-Justin, Elsevier, Amsterdam (1995)

[86] A. Lopatin, A. Georges, and T. Giamarchi, *Phys. Rev.* B **63**, 075109 (2001)

[87] A. Georges, T. Giamarchi, and N. Sandler, *Phys. Rev.* B **61**, 16393 (2000)

[88] B. Korin-Hamzič, E. Tafra, M. Basletič, A. Hamzič, G. Untereiner, and M. Dressel, *Phys. Rev.* B **67**, 014513 (2003)

[89] J. Solyom, *Adv. Phys.* **28**, 209 (1979)

[90] T. Giamarchi, *Phys. Rev.* B **46**, 342 (1992)

[91] J. Voit, *J. Phys.* C **21**, L1141 (1996)

[92] J. Slater, *Rev. Mod. Phys.* **18**, 441 (1946)

[93] L. D. Landau and E. M. Lifshitz, *Electrodynamics of Continuous Media*, Pergamon, Oxford (1984)

[94] C. G. Montgomery, *MIT Radiation Laboratory Series*, Vol. 11, *Technique of microwave measurements*, 1947, pp. 298–300

[95] C. P. Poole, *Electron spin resonance. A Comprehensive Treatise on Experimental Techniques*, Wiley Interscience, New York, 1967, p. 137

[96] C. H. Townes, A. L. Schawlow, *Microwave Spectroscopy*, McGraw-Hill, New York, 1955, p. 380

[97] H. A. Bethe, *Phys. Rev.* **66**, 163 (1944)

[98] S. Hill, P. S. Sandhu, C. Buhler, S. Uji, J. S. Brooks, L. Seger, M. Boonman, A. Wittlin, J. A. A. J. Perenboom, P. Goy, R. Kato, H. Sawa, and S. Aonuma, in *Millimeter and Submillimeter Waves III*, ed. by M. N. Afsar, *Proc. SPIE* **2842**, pp. 296–306 (1996)

[99] O. Klein, S. Donovan, M. Dressel, and G. Grüner, *Int. J. Of Infrared and Millimeter Waves*, **14**, 2423 (1993)

[100] S. Donovan, O. Klein, M. Dressel, K. Holczer, and G. Grüner, *Int. J. Of Infrared and Millimeter Waves*, **14**, 2459 (1993)

[101] M. Dressel, O. Klein, S. Donovan, and G. Grüner, *Int. J. Of Infrared and Millimeter Waves*, **14**, 2489 (1993)

[102] G. Grüner, *Millimeter and Submillimeter Wave Spectroscopy of Solids*, Springer-Verlag, Berlin (1998)

[103] MAFIA version 3.22, 1999, "Solution of <u>MA</u>xwell's equations by <u>F</u>inite <u>I</u>ntegration <u>A</u>lgorithms", a commercial, interactive program package for the computation of electromagnetic fields which uses the finite integration technique

[104] S. Biermann, A. Georges, A. Lichtenstein, and T. Giamarchi, *Rev. Rev. Lett.)* **87**, 276405 (2001)

[105] M. Dressel, A. Schwartz, G. Grüner, and L. Degiorgi, *Phys. Rev. Lett.* **77**, 398 (1996)

[106] M. Dumm, M. Dressel, A. Loidl, B. W. Fravel, K. P. Starkey, and M. Montgomery, *Phys. Rev.* B **61**, 511 (2000)

[107] M. Miljak, J. R. Cooper, and K. Bechgaard, *Phys. Rev.* B **37**, 4970 (1988)

[108] J. R. Cooper, L. Forró, B. Korin-Hamzić, K. Bechgaard, and A. Moradpour, *Phys. Rev.* B **33**, 6810 (1986)

[109] J. Moser, J. R. Copper, D. Jérome, B. Alavi, S. E. Brown, and K. Bechgaard, *Phys. Rev. Lett.* **84**, 2674 (2000)

[110] S. Kirchner, *Diploma Thesis*, Universität Stuttgart, Stuttgart (1999)

[111] C. S. Jacobsen, K. Mortensen, M. Weger, K. Bechgaard, *Solid State Commun.* **38**, 423 (1981)

[112] S. Tomić, J. R. Cooper, W. Kang, D. Jérome, and K. Maki, *J. Phys. (Paris)* I **1**, 1603 (1991)

[113] F. Zámborszky, G. Szeghy, G. Abdussalam, L. Forró, G. Mihály, Phys. Rev. B **60**, 4414 (1999)

[114] G. Mihály, I. Kézsmárki, F. Zámborszky, and L. Forró, *Phys. Rev. Lett.* **84**, 2670 (2000)

[115] H. C. Montgomery, *J. Appl. Phys.* **42**, 2971 (1971)

[116] B. Gallois, J. Gaultier, T. Lamcharfi, F. Bechtel, and A. Filhol, *Synth. Met.* **19**, 321 (1987)

[117] V. M. Yakovenko, and A. T. Zheleznyak, *Sinth. Met.* **120**, 1083 (2001)

[118] V. M. Yakovenko, and A. T. Zheleznyak, *Sinth. Met.* **103**, 2202 (1999)

[119] A. T. Zheleznyak, and V. M. Yakovenko, *Europhys. J.* B **11**, 385 (1999)

[120] M. Weger, *J. Phys. (Paris)* **38**, 1097 (1977)

[121] P. M. Chaikin, P. Haen, E. M. Engler, and R. L. Greene, *Phys. Rev.* B **24**, 7155 (1981)

[122] L. P. Gor'kov, *Europhys. Lett.* **31**, 49 (1995)

[123] L. P. Gor'kov, *J. Phys. (Paris)* I **6**, 1697 (1996)

[124] L. P. Gor'kov, and M. Mochena, *Phys. Rev.* B **57**, 6204 (1998)

[125] J. M. Delrieu, M. Roger, Z. Toffano, A. Moradpour, and K. Bechgaard *J. Phys.* **47**, 839 (1986)

[126] G. Grüner, *Rev. Mod. Phys.* **60**, 1129 (1988)

[127] L. Degiorgi, B. Alavi, G. Mihály, and G. Grüner, *Phys. Rev.* B **44**, 7808 (1991)

[128] L. Degiorgi, and G. Grüner, *Phys. Rev.* B **44**, 7820 (1991)

[129] P. A. Lee, T. M. Rice, and P. W. Anderson *Solid State Commun.* **14**, 703 (1974)

[130] G. Kriza, G. Quirion, O. Traetteberg, and D. Jérome, *Europhys. Lett.* **16**, 585 (1991)

[131] S. Donovan, L. Degiorgi, and G. Grüner, *Europhys. Lett.* **19**, 433 (1992)

[132] S. Donovan, M. Dressel, Y. Kim, L. Degiorgi, G. Grüner, and W. Wonneberger, *Phys. Rev.* B **49**, 3363 (1994)

[133] P. Fertey, M. Poirier, and P. Batail, *Eur. Phys. J.* B **10**, 305 (1999)

[134] W. M. Walsh Jr., F. Wudl, G. A. Thomas, D. Nalewajek, J. J. Hauser, P. A. Lee, and T. Poehler, *Phys. Rev. Lett.* **45**, 829 (1980)

[135] A. Jànossy, M. Hardiman, and G. Grüner, *Solid State Commun.* **46**, 21 (1983)

[136] L. I. Buravov, V. N. Laukhin, and A. G. Khomenko, *Sov. Phys. JETP* **61**, 1292 (1985)

[137] H. H. S. Javadi, S. Sridhar, G. Grüner, L. Chiang, and F. Wudl, *Phys. Rev. Lett.* **55**, 1216 (1985)

[138] N. Biškup, *PhD Thesis*, University of Zagreb, Zagreb (1996)

Curriculum vitae

August 1, 1975	Born in Kriwoj Rog, Ukraine, former USSR.
April 7, 2000	Marriage with Helene Petukhov (Uschakow).
November 6, 2001	Daughter Lisa Petukhov born.
1982 – 1992	High School No. 16, Stary Oskol, Russia, graduated with honors.
1992 – 1998	Moscow Institute of Physics and Technology (State University), Dolgoprudny, Russia.
Sept. 1997 – Oct. 1998	Diploma (M.S.) thesis, General Physics Institute, Russian Academy of Sciences, Moscow, Russia. Title: "Transport Characteristics of FeSi". Supervisor: Prof. Demishev, Dr. Glushkov.
Nov. 1998 – Mar. 2003	PhD student, 1. Physikalisches Institut, Universität Stuttgart, Stuttgart, Germany. Title: "Microwave Investigations of Low-Dimensional Organic Conductors". Supervisor: Prof. Dr. Martin Dressel

List of Publications

1. N. Sluchanko, V. Glushkov, S. Demishev, M. Kondrin, K. Petukhov, A. Pronin, N. Samarin, Y. Bruynseraede, V. Moshchalkov, and A. Menovsky,

   "Low-temperatures anomalies of the Hall coefficient in FeSi",

   JETP Lett. **68**, 817 (1998)

2. V. Glushkov, N. Sluchanko, S. Demishev, M. Kondrin, A. Pronin, K. Petukhov, N. Samarin, Y. Bruynseraede, V. Moshchalkov, and A. Menovsky,

   "Low temperature transport anomalies in FeSi",

   Physica B **284**, 1179 (2000)

3. N. Sluchanko, V. Glushkov, S. Demishev, M. Kondrin, K. Petukhov, N. Samarin, V. Moshchalkov, and A. Menovsky,

   "Thermopower in the regime of strong Hubbard correlations in FeSi",

   Europhys. Lett., **51**, 557 (2000)

4. N. Sluchanko, V. Glushkov, S. Demishev, M. Kondrin, V. Ivanov, K. Petukhov, N. Samarin, A. Menovsky, and V. Moshchalkov,

   "Ground State Formation in a Strong Hubbard Correlation Regime in Iron Monosilicide",

   JETP **92**, 312 (2001)

5. M. Dressel, N. V. Kasper, K. Pethukov, B. Gorshunov, G. Gruner, P. Huth and H. Adrian,

   "The Nature of Heavy Quasiparticles in Magnetically Ordered Heavy Fermions UPd_2Al_3 and UPt_3",

   Phys. Rev. Lett. **88**, 186404 (2002)

6. M. Dressel, N. V. Kasper, K. Pethukov, D. N. Peligrad, B. Gorshunov, M. Jourdan, P. Huth, and H. Adrian,

   "Correlation gap in the heavy-fermion antiferromagnet UPd_2Al_3",

   Phys. Rev. B **66**, 035110 (2002)

Acknowledgements

First of all, I would like to thank my advisor, Prof. Dr. Martin Dressel, for his generous support and continual encouragement throughout my time in Stuttgart, and for the opportunities to explore the world, scientifically and otherwise. His clear understanding of physics and sharp insight through verity of encountered problems were very helpful and the major source of propulsion in this project.

I am very grateful to Prof. Dr. Michael Mehring for his participation on my oral committees and for his bright lectures on the course of Condensed Matter Physics.

I also want to thank Martina Wentzel, our secretary, for the great job she did in organizing travels and getting useful information for foreigners in Germany.

Working in Prof. Dressel's group has given me the opportunity to work (and play) with a number of people. In particular, I would like to thank Tobby Brandt, Michael Dumm, Bruno Gompf, Phillip Haas, Kurt Lassmann, Stephan Mair, Adriana Matei, Belal Salameh, Marc Scheffler, Jürgen Thoms, Amy Vongtragool, and Peter Weber, all of whom had a hand in this work in one way or another.

The single crystals used in this work have been grown by Gabriele Untereiner, to whom I am very much obligated. Her contribution to this thesis, as well as to the existence of the institute, is hard to overestimate.

The expertise of the technical support stuff in the Physics Department here at the University of Stuttgart is also appreciated. I would like to thank all the technicians in both the departmental machine shop and in the electronics shop.

I cannot express enough thanks to Boris Gorshunov, for his friendship and assistance over the past couple of years, without which I am sure I would never be at this

point now.

Finally, special thanks go to to my wife, Elena, and my parents and parents-in-law, whose love and endurance make me possible to complete the long journey of times for doctorate works.